Superconducting Proximity Effect in Quantum Anomalous Hall Insulators

INAUGURAL-DISSERTATION

to obtaining the degree of doctor
from the Faculty of Mathematics and Natural Sciences
of the University of Cologne

by
Anjana Uday
from Thrissur, India

Cologne, 2024

Superconducting Proximity Effect in Quantum Anomalous Hall Insulators

Anjana Uday

First examiner: Prof. Dr. Yoichi Ando

Second examiner: Prof. Dr. Annika Kurzmann

Chairperson: Prof. Dr. Achim Rosch

Date of the examination: 18 February 2025

Abstract

When a thin film of a topological insulator (TI) is doped with magnetic impurities, it can exhibit the quantum anomalous Hall effect (QAHE). This phenomenon emerges from the breaking of time-reversal symmetry (TRS) in a system with strong spin-orbit coupling, resulting in a vanishing longitudinal resistance and a quantized Hall resistance of h/e^2 (where h is the Planck constant and e is the charge of an electron), even in the absence of an external magnetic field. Such a magnetic topological insulator is called a quantum anomalous Hall insulator (QAHI), where electrical current is carried by one-dimensional (1D) chiral edge states that propagate along the sample boundaries, while the two-dimensional (2D) bulk remains insulating. When superconducting pairing correlations are induced in such a material via the proximity to an s-wave superconductor, the resulting topological superconductivity is predicted to host chiral Majorana edge modes. In a Hall-bar device configuration, where a superconducting strip lies across the full width of a QAHI thin film, a quantized two-terminal conductance of $\frac{1}{2}(e^2/h)$ was proposed as the smoking-gun evidence of the topological superconducting phase associated with a single chiral Majorana mode. This reduction in two-terminal conductance by a factor of two, compared to e^2/h observed in a bare QAHI without the superconducting strip, has been experimentally reported. However, the origin of this $\frac{1}{2}(e^2/h)$ conductance feature remains a topic of active debate, as alternative trivial mechanisms have also been proposed. This emphasizes the need for more robust experimental evidence to confirm the superconducting proximity effect in QAHIs.

In this thesis, narrow superconducting electrodes of Nb on top of a QAHI thin film are investigated with widths ranging from 160 to 520 nm. By measuring the nonlocal 'downstream' resistance with respect to the grounded superconducting electrode, a negative resistance contribution of $-400\ \Omega$ is observed for the narrowest superconducting electrode. This contribution decreases exponentially as the width of the SC increases. This negative nonlocal resistance is attributed to crossed Andreev reflection (CAR) taking place across the superconducting electrode. In the CAR process, an electron in the chiral edge state, arriving at the superconducting electrode with an energy eV smaller than the SC gap Δ, is converted into a hole in the chiral edge state leaving from the SC, carrying a potential of $-V$. Simultaneously, a Cooper pair is formed in the superconductor. The observation of a negative edge potential, measurable as a negative 'downstream' resistance with respect to the grounded SC in our experiment, is a compelling signature of induced superconducting pair correlation in the chiral edge state of the QAHI. Moreover, the characteristic length over which the CAR process is suppressed with increasing the width of the SC is found to be significantly longer than the superconducting coherence length of Nb. This implies that the CAR process is mediated by the superconductivity induced in the QAHI film underneath the Nb electrode, rather than by the Nb superconductor itself. These findings are supported by a detailed Landauer-Büttiker analysis of the experimental set-up, accounting for all possible processes at the SC-QAHI interface, and by KWANT simulations that incorporate charge disorder in the QAHI film, as well as the metallization effects by the superconducting electrode.

Having established a reliable method to proximitize a QAHI thin film using a superconducting Nb, the second part of this thesis re-evaluates the $\frac{1}{2}(e^2/h)$ feature in two-terminal conductance measurements. Rather than only characterizing the device's two-terminal conductance, the potentials of all chiral edge states arriving at and leaving from the superconducting Nb electrode are determined in this thesis, providing a comprehensive understanding of the transport through the proximitized QAHI thin film. Two Hall-bar devices were fabricated for this purpose. In the first device, a Nb superconducting electrode spans the full width of the Hall-bar, forming a proximitized QAHI region beneath the SC. The second device serves as a control experiment, where the QAHI film is interrupted underneath the superconducting electrode, creating two separate QAHI Hall-bars connected in series through the Nb electrode. For both devices, a quantized resistance of h/e^2 is measured across the Nb electrode in a four-terminal configuration when the current flows through the QAHI film. This quantized resistance of h/e^2 in the four-terminal set-up employed in this thesis corresponds to a two-terminal conductance of $\frac{1}{2}(e^2/h)$ for the device. No difference is observed between the devices with and without a continuous QAHI under the superconducting electrode. This indicates that the $\frac{1}{2}(e^2/h)$ conductance feature is unrelated to chiral Majorana edge mode transport, as the interrupted QAHI in the control device prevents Majorana transmission underneath the superconducting electrode. In addition, the potentials of all chiral edge states arriving at and leaving from the superconducting electrode remain unchanged when the external magnetic field exceeds the upper critical field of Nb, which points to a trivial effect unrelated to (induced) superconductivity. By using the Landauer-Büttiker formalism, the experimental data are shown to be consistent with a model in which the superconductor equilibrates all the chiral edge states arriving at and leaving from the superconducting electrode. Lastly, no negative nonlocal edge potentials are observed in Hall-bar devices with a Nb strip, in contrast to the narrow Nb electrodes studied in the first part of this thesis. This suggests that signatures of the superconducting proximity effect in QAHI thin films are only observable within a length scale comparable to the superconducting coherence length.

The findings in this thesis provide critical insights into the chiral edge transport at superconducting electrodes interfaced with QAHIs and prove the existence of the SC proximity effect in QAHIs, offering a foundation for future studies of topological superconductivity, Majorana physics, and the search for non-Abelian zero modes.

Contents

List of Figures

List of Abbreviations

TI Topological insulator. i, v, 2, 3, 5, 13, 16, 29, 30

TRS Time-reversal symmetry. i, 2–4, 11, 17

TSC Topological superconductor. 9–13, 16, 30, 69–71

Chapter 1

Introduction

A highly promising strategy for constructing a fault-tolerant quantum computer is based on the existence of topological states of matter [1]. The quantum Hall effect, discovered by Klaus von Klitzing in 1980 [2], is the first example of a topological state observed in condensed matter. When a two-dimensional electron gas (2DEG) is subjected to a strong magnetic field, it leads to the formation of Landau levels and a state defined by quantized Hall conductance and zero longitudinal resistance. Later, it was theoretically predicted [3–5] that magnetic insulating materials with strong spin-orbit coupling can exhibit a quantized Hall conductance as well, along with a vanishing longitudinal resistance without an applied magnetic field. This phenomenon is known as the quantum anomalous Hall effect (QAHE). This prediction was followed by the experimental realization of the QAHE in magnetically doped topological insulators, in particular Cr- or V-doped $(Bi_xSb_{1\text{-}x})_2Te_3$ thin films [6–11]. In both the quantum anomalous Hall insulator (QAHI) and quantum Hall insulator (QHI), the current is carried by the dissipationless one-dimensional (1D) chiral edge state(s). Theoretically, two distinct types of chiral topological superconductivity are realized by coupling a QAHI and QHI with an s-wave superconductor. In the former system, 2D topological superconductivity is realized with 1D propagating chiral Majorana edge modes (CMEMs) if the 2D topological surface states of a QAHI is proximitized [12–14]. This chiral motion along the boundary of the topological superconductor can be exploited to exchange a pair of non-abelian anyons in real space by creating a π-phase domain wall in the CMEMs [15–18]. In the latter system, the two counter-propagating 1D chiral edge states are coupled through crossed Andreev reflection, creating a 1D topological superconductor with zero-dimensional Majorana bound states that exhibit non-abelian braiding statistics [19, 20]. However, if a quasi-1D QAHI is realized, by either etching a trench in the QAHI film or etching the QAHI into a nanowire, then it is also possible to proximitize the two counter-propagating edge states of the QAHI directly through the s-wave superconductor, creating a pair of non-abelian Majorana zero modes (MZMs) at the ends of the quasi-1D structure [14, 21]. Hence, the QAHI and QHI are both promising platforms for the realization of a topological quantum computer [22].

The main objective of this thesis is to confirm the presence of superconducting proximity effect in a quantum anomalous Hall insulator (QAHI) contacted by an s-wave superconductor (SC) and to investigate the chiral edge transport in such heterostructures. The content of this thesis is structured in five chapters. In the first chapter, a brief introduction to magnetic topological insulators (MTIs) and the QAHE will be given, followed by a discussion of the current state-of-the-art SC-QAH heterostructures. Lastly, a literature overview is given of the SC-QH hybrid systems, which as the QH research field is more matured served as a valuable reference when designing the experiments presented in this thesis. In chapter 2, the nonlocal resistance measured with respect to a grounded narrow superconducting electrode on top of a QAHI thin film is shown to be negative under certain conditions. This is the most important result of this thesis, as it is interpreted as the first real proof for induced superconducting correlations in chiral edge states of a QAHI. In chapter 3, multi-terminal Hall-bar devices are investigated with μm-size SC strips lying across their full width. This experiment addresses the current debate on whether or not half-integer quantized conductances are trustworthy signatures for the presence of chiral Majorana edge states [13, 23–29]. In chapter 4, a conclusion is given for these two experiments, followed by an outlook for the field in chapter 5.

1.1 Introduction to the QAHE

A topological insulator (TI) has an insulating bulk with a metallic boundary as a consequence of its nontrivial topology. When a TI comes in contact to a trivial insulator (for instance the vacuum), the bulk-boundary correspondence forces the band gap to close and a gapless interface state emerges. Three-dimensional (3D) TIs are accompanied by two-dimensional (2D) gapless surface states and two-dimensional 2D TIs are associated with gapless 1D edge states at the boundary, as shown in Figs. 1.1a-b and 1.1c-d respectively. These surface/edge states are protected by time-reversal symmetry (TRS) and have a helical spin polarization as its spin is locked to its momentum [30]. The first experimental realization of a 2D TI, also known as a quantum spin Hall insulator, was in HgTe quantum wells [31], following the theoretical prediction by Bernevig *et al.* [32]. When an unstrained HgTe quantum well exceeds the critical thickness ($t_c \approx 6.3$ nm), a set of two spin-polarized, counterpropagating edge states are formed at the edge of the sample, giving rise to a quantized longitudinal conductance. The spin polarization of the edge states in a quantum spin Hall insulator prohibits elastic back-scattering from nonmagnetic impurities, leading to dissipationless edge transport.[1] Although all the experiments on the HgTe quantum wells only observed the quantized conductance for channel lengths up to about 200 μm, as a consequence of the inelastic scattering when the edge states encounter charge puddles [31, 33–35].

In recent years, many 3D TIs were proposed and experimentally realized, amongst which the chalcogenide TI materials like Bi_2Se_3, Bi_2Te_3, Sb_2Te_3 and their alloys [30, 36–40]. In Bi_2Te_3, the Dirac point is buried in the bulk valence band and the Fermi level (E_F) lies in the bulk conduction band due to the electron-type bulk carriers induced by Te vacancies making it an n-type TI. On the other hand, the Dirac point lies within the 2D bulk gap in Sb_2Te_3, but E_F lies in the bulk valence band due to the hole-type bulk carriers from the Sb-Te antisite defects making it a p-type TI. Hence, by fine tuning the x-composition in the ternary compound $(Bi_xSb_{1-x})_2Te_3$, E_F and the Dirac point can

[1] Note that each metal contact along the edge will equilibrate the two counter-propagating edge states, giving rise to a quantized voltage drop. Hence, the four-terminal longitudinal resistance will be quantized to a multiple of $h/(2e^2)$ depending on the number of metal contacts [31].

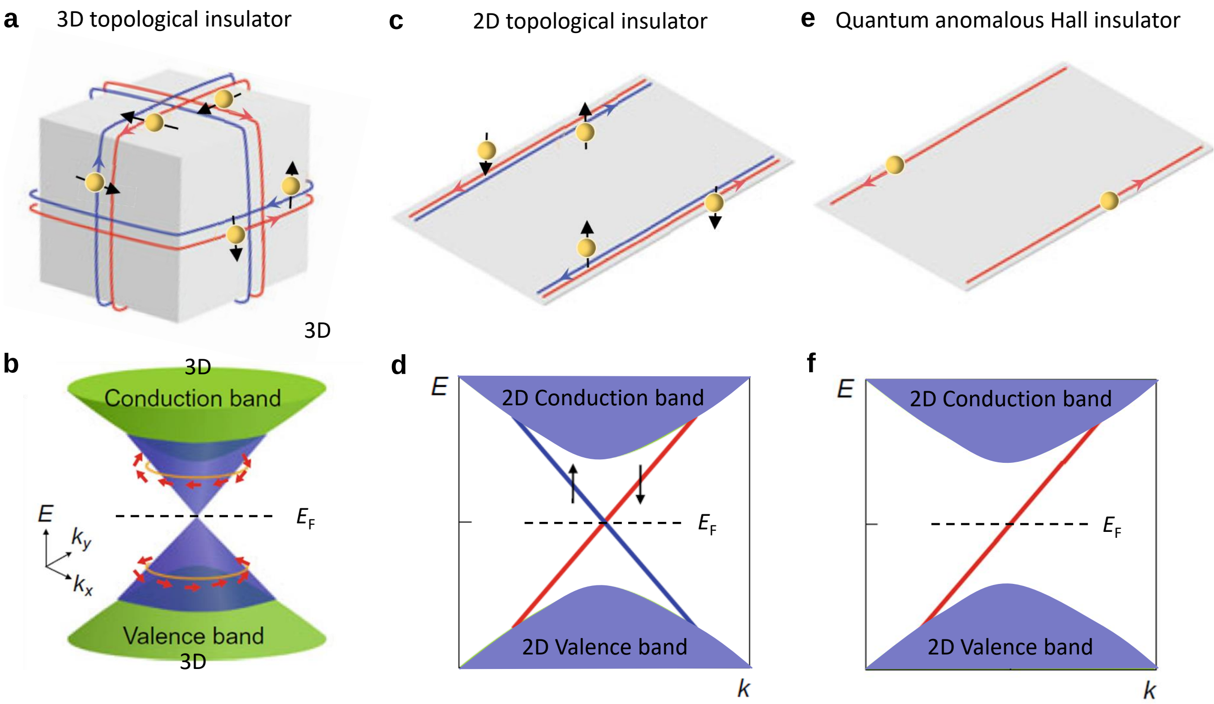

Fig. 1.1 | The surface and edge states of TIs with Dirac dispersion. **a**, Real-space illustration of a 3D TI with the 2D helical surface states. The electrons with opposite spins move in opposite directions due to the spin-momentum locking. **b**, The massless Dirac-like dispersion of the helical surface state that connects the bulk valence and conduction bands, forming a 2D Dirac cone **c**, Real-space illustration of a 2D TI with 1D helical states. **d**, The energy dispersion of the 1D helical states in a 2D bulk band gap. **e**, Real-space illustration of a QAHI with a single chiral 1D edge state. Note that the 1D edge channel in a QAHI is not fully spin polarized (see Eq. 1.8). **f**, The energy dispersion of a QAHI. The 2D helical surface states at the Dirac point are gapped due to the broken TRS, but this gap is closed at the edge of the sample by the chiral 1D edge state. When the Fermi level E_{F} lies inside the 2D bulk band gap, the current is only carried by the dissipationless edge state.

be moved into the 2D bulk gap via charge compensation [38, 40]. Moreover, when the thickness of such a 3D TI film is reduced, the top and bottom surface states hybridize, opening up a gap at the Dirac point. This crossover from 3D TI to 2D TI is oscillatory as it alternates between trivial insulator and quantum spin Hall insulator phases [41]. In Ref. [42], the change in the longitudinal resistance between diverging and finite ($\sim h/(2e^2)$) values for varying thicknesses of exfoliated flakes of $\mathrm{Bi_{0.7}Sb_{1.3}Te_{1.05}Se_{1.95}}$ were interpreted as signatures of these phase transitions between trivial and 2D TI states. However, the presence of long-range Coulomb disorder due to the charged impurities, can bring the system in a metallic state of percolated charge puddles, masking the signatures of the quantum spin Hall phase. This disorder-driven insulator-to-metal transition can only be avoided with a large enough hybridization gap and low impurity concentration [43, 44]. This indicates that the experimental realization of the quantum spin Hall insulator phase by thinning down a 3D TI is extremely challenging, as one needs to precisely control the thickness and disorder.

The two primary limitations of a quantum spin Hall insulator, i.e. the restricted channel length for conductance quantization and the stringent control required over material thickness, necessitate the development of a platform that enables extended quasi-ballistic transport with reduced sensitivity to sample variations such as thickness. In 2010, Yu *et al.* proposed an alternative material framework that also gives rise to dissipationless 1D edge transport, but breaks TRS, i.e. the realization of a quantum anomalous Hall insulator (QAHI), see Fig. 1.1e-f. The current is carried by the 1D chiral edge state when E_{F} lies in the 2D bulk band gap induced by the out-of-plane magnetization. The two essential ingredients are a ferromagnetic 2D insulator and a band inversion with strong spin-orbit coupling [5]. A straightforward candidate is breaking the TRS in a quantum spin Hall insulator. However, experimentally it was shown that Mn-doped HgTe quantum wells lead to paramagnetic or antiferromagnetic, not ferromagnetic ordering [45, 46].[2]

The first experimental realization of the QAHE was achieved in Cr-doped $(\mathrm{Bi_xSb_{1\text{-}x}})_2\mathrm{Te_3}$ thin films with a thickness of 5 quintuple layers grown on $\mathrm{SrTiO_3}$ substrates by molecular beam epitaxy (MBE). The expected quantized Hall resistance of h/e^2 along with a significant drop in the longitudinal resistance was achieved by gate-tuning the E_{F} into the magnetically induced energy gap in the 2D density of states at zero applied magnetic field [7]. Subsequently, the QAHE was realized in V-doped $(\mathrm{Bi_xSb_{1\text{-}x}})_2\mathrm{Te_3}$ with a larger coercive field ($H_{\mathrm{c,FM}}$) and a relatively higher Curie temperature ($T_{\mathrm{c,FM}}$) than the Cr-doped $(\mathrm{Bi_xSb_{1\text{-}x}})_2\mathrm{Te_3}$ [8]. Additionally, in recent years, the quantized Hall resistance of the QAHE was also observed in twisted bilayer graphene [48], $\mathrm{MnBi_2Te_4}$ [49], $\mathrm{MnBi_2Te_4/Bi_2Te_3}$ superlattices [50] and moiré heterostructures of $\mathrm{MoTe_2/WSe_2}$ [51]. Until now, a vanishing longitudinal resistance was only observed in uniform or modulation Cr- or V-doped $(\mathrm{Bi_xSb_{1\text{-}x}})_2\mathrm{Te_3}$ [8, 9, 52–55].

In 2022, our lab successfully reported the observation of quantized Hall resistance ($R_{\mathrm{yx}} = h/e^2$) and a vanishing longitudinal resistance (R_{xx}) in the MBE grown thin films of V-doped $(\mathrm{Bi_xSb_{1\text{-}x}})_2\mathrm{Te_3}$ on InP (111)A [53].[3] The temperature dependence for the Hall (ρ_{yx}) and longitudinal (ρ_{xx}) resistivity is shown in Fig. 1.2a. The ρ_{yx} stays zero until the Curie temperature $T_{\mathrm{c,FM}} = 18$ K, and increases to h/e^2 due to the formation of the 1D chiral edge channel upon spontaneous magnetization. Similarly, the insulating 2D (and 3D) bulk contribution dominates in ρ_{xx} until $T_{\mathrm{c,FM}}$, below which the current is carried by the dissipationless 1D chiral edge state. The magnetic field dependence of ρ_{yx} and ρ_{xx} is presented in Fig. 1.2b, measured at 40 mK. As the magnetization changes at the coercive field (around 1 T), ρ_{yx} is quantized either at $+h/e^2$ or $-h/e^2$, arising from the integer topological invariant i.e. Chern number $\mathcal{C} = \pm 1$ of the system (detailed discussion in the section below). Simultaneously, ρ_{xx} vanishes except for a peak at the coercive field, where the QAHE is lost upon magnetization reversal. One important detail of this work is that the QAHE is achieved without applying any gate voltage [53], i.e. the chemical potential is tuned into the magnetic exchange gap during the MBE growth of the thin film by fine tuning the Bi and Sb concentration. Moreover, this work investigated the loss of dissipationless edge transport with increasing current, referred to as the breakdown of the QAHE [52, 56]. The longitudinal voltage (V_{x}) remains zero until the breakdown current ($I_{\mathrm{BD}} \approx 160$ nA), above which a gradual upturn is observed signalling the onset

[2] Recently, first principle calculations suggest that V- or Cr-doped CdTe and HgTe may lead to ferromagnetic ordering which may pave way for new platforms for the QAHE [47].

[3] In this publication [53], G. L., A. B., and I are co-first authors.

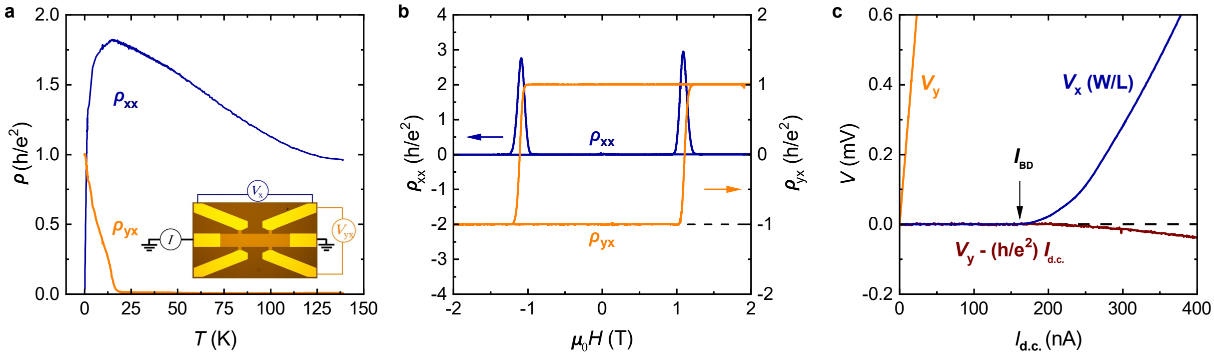

Fig. 1.2 | The quantum anomalous Hall effect. **a**, Temperature dependence of the transverse (ρ_{yx}) and longitudinal (ρ_{xx}) resistivity, measured using a Hall-bar configuration with $I_{\mathrm{d.c.}} = 50$ nA. A hall-bar device with the measurement scheme for Hall and longitudinal voltage, V_{yx} and V_{x}, respectively. **b**, Magnetic-field dependence of ρ_{yx} and ρ_{xx}, measured at 40 mK with $I_{\mathrm{d.c.}} = 30$ nA. **c**, The I-V characteristics for the transverse (V_{y}) and longitudinal voltage (V_{y}) measured at 10 mK in 0 T after training the sample at +2 T to align all the magnetic domains. Note that V_{x} was normalized by the voltage-contact separation (L) and the width (W) of the Hall-bar. Both the voltages, V_{x} and V_{y} shows deviation from the ideal QAHE above ∼160 nA. This onset of dissipation with increasing current is referred to as the current-induced breakdown of the QAHE.

of dissipation. The hall voltage shows a linear response and deviates less strongly from h/e^2 at high currents. The breakdown is attributed to the electric-field driven percolation of 2D charge puddles across the width of the sample [53]. Recently, Röper *et al.* studied the characteristics of edge plasmon in a QAHI using broadband microwave transport, identifying two different dissipation mechanisms for the chiral edge states [57]. In the low-voltage, low-temperature regime, a frequency-dependent dissipation was observed, attributed to charge puddles and modeled as an RC series circuit. In contrast, the dissipation was frequency-independent at elevated temperatures and for higher voltage regimes associated with 2D diffusive transport due to thermal excitation and percolation of 2D charge puddles well above breakdown [53, 57], respectively.

1.2 Low-energy Effective Hamiltonian of QAHI

In this section the 2D low-energy effective Hamiltonian for a magnetically doped TI is discussed in order to understand the realization of the QAHE and in the next section, the superconducting proximity effect in such a system. The effective Hamiltonian [5, 13] is given by,

$$\mathcal{H}_0 = \sum_k \psi_k^\dagger H_0(k) \psi_k, \tag{1.1}$$

with $\psi_k = (c^t_{k\uparrow}, c^t_{k\downarrow}, c^b_{k\uparrow}, c^b_{k\downarrow})^T$, where the superscripts t and b correspond to the top and bottom surface state with up (↑) or down (↓) spin, and

$$H_0(k) = \hbar v_{\mathrm{D}}(k_y\sigma_x - k_x\sigma_y)\rho_z + m(k)\rho_x + \lambda\sigma_z, \tag{1.2}$$

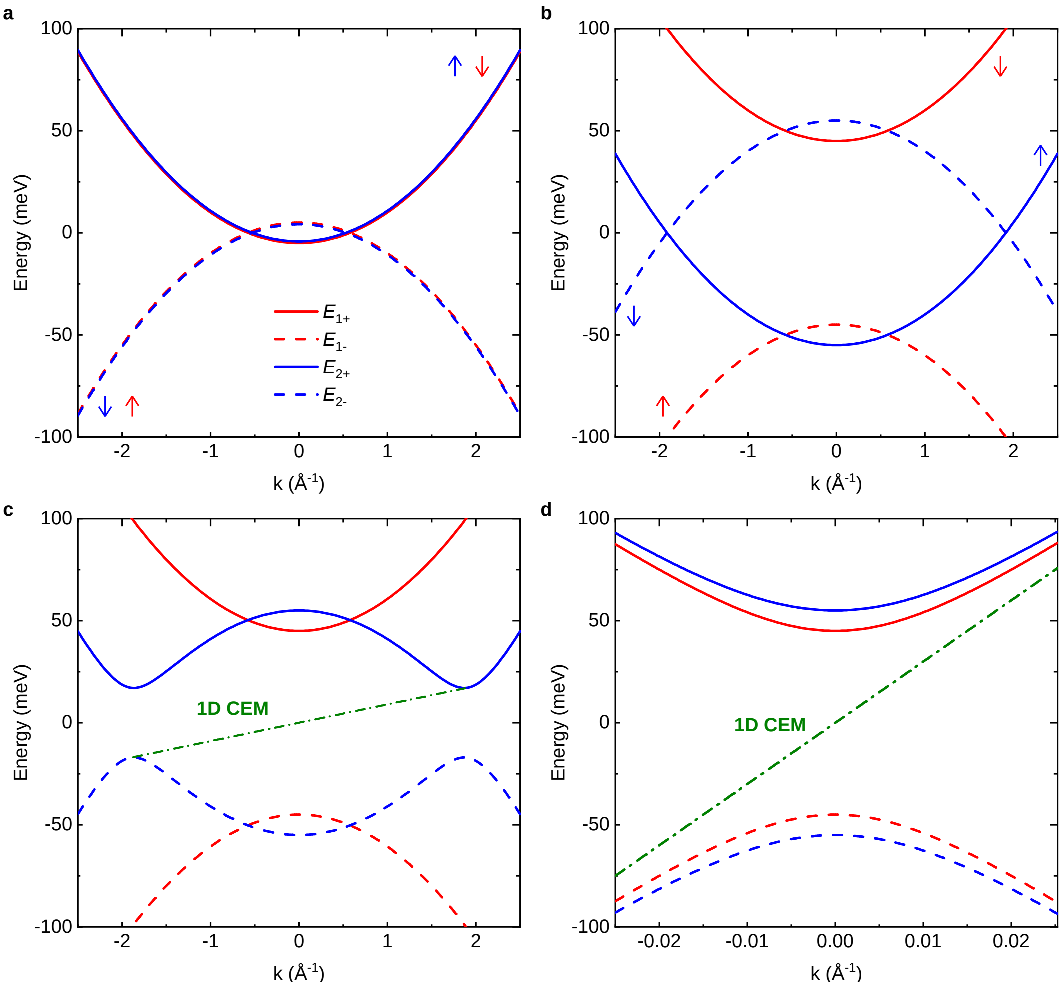

Fig. 1.3 | Evolution of the energy spectrum upon including magnetization and spin-orbit coupling. The red (blue) color shows the eigenvalues $E_{1,\pm}$ ($E_{2,\pm}$) and the arrows represent their spin. The green dash-dot line corresponds to the 1D chiral edge state with $E_{\mathrm{Edge}} = \hbar v_{\mathrm{D}} k$. **a**, In the absence magnetization and spin-orbit coupling, the eigenvalues are parabolas with a band inversion since $m_0 m_1 < 0$. **b**, The band inversion for $E_{1,+}$ and $E_{1,-}$ is lost for large enough magnetization strength. **c**, A gap is opened up at the unprotected crossings between $E_{2,+}$ and $E_{2,-}$, giving rise to a 1D chiral edge mode when both the magnetization and the spin-orbit coupling are included. Here, the spin-orbit coupling is only at 0.3% of its full strength, to demonstrate the gap opening. **d**, Band structure with the magnetization and the full spin-orbit coupling strength, showing a direct band gap. Note that the x-axis range has changed by two orders of magnitude. This figure was inspired by Ref. [5]. The material parameters used for generating this figure are $m_0 = -5$ meV, $m_1 = 15$ meVÅ^2, $\lambda = 50$ meV, and $\hbar v_{\mathrm{D}} = 3$ eVÅ (as in Chapter 2).

where v_{D} is the Dirac velocity, σ_i and ρ_i $(i = x, y, z)$ are the Pauli matrices for the spin and top-bottom surface degrees of freedom, respectively. As the top and bottom surface states are close to each other, their wavefunctions overlap and hybridize which leads to the opening of a mass gap. This is taken into account by the mass term: $m(k) = m_0 + m_1(k_x^2 + k_y^2)$. In addition, λ is the magnetization strength along the z-axis induced by the ferromagnetic ordering, whose amplitude and sign change during the magnetization reversal of the MTI. The 4×4 Hamiltonian $H_0(k)$ in Eq. 1.2 can be block-diagonalized to

$$\tilde{H}_0(k) = \begin{bmatrix} h(k) + \lambda\sigma_z & 0 \\ 0 & h^*(k) - \lambda\sigma_z \end{bmatrix} = \begin{bmatrix} H_1(k) & 0 \\ 0 & H_2(k) \end{bmatrix}, \tag{1.3}$$

with

$$h(k) = \hbar v_{\mathrm{D}}(k_y\sigma_x - k_x\sigma_y) + m(k)\sigma_z, \tag{1.4}$$

by changing the basis to $((c^t_{k\uparrow}+c^b_{k\uparrow}), (c^t_{k\downarrow}-c^b_{k\downarrow}), (c^t_{k\downarrow}+c^b_{k\downarrow}), (c^t_{k\uparrow}-c^b_{k\uparrow}))^T/\sqrt{2}$ [5]. Subsequently, the four energy eigenvalues (bands) can then be determined:

$$E_{1,\pm} = \pm\sqrt{\hbar^2 v_{\mathrm{D}}^2(k_x^2 + k_y^2) + [(m_0 + \lambda) + m_1((k_x^2 + k_y^2)]^2} \quad \text{for} \quad H_1(k), \tag{1.5}$$

$$E_{2,\pm} = \pm\sqrt{\hbar^2 v_{\mathrm{D}}^2(k_x^2 + k_y^2) + [(m_0 - \lambda) + m_1((k_x^2 + k_y^2)]^2} \quad \text{for} \quad H_2(k), \tag{1.6}$$

Note that the only difference between the equations for $E_{1,\pm}$ and $E_{2,\pm}$ is the sign in front of λ, whose own sign depends on the out-of-plane magnetization direction (up or down). The energy spectra are shown for four different scenarios in Fig. 1.3. In panel a, the eigenvalues are plotted in the absence of magnetization ($\lambda = 0$) and spin-orbit coupling ($v_{\mathrm{D}} = 0$). Hence, only $m(k) = m_0 + m_1(k_x^2 + k_y^2)$ remains with $m_0 = -5$ meV and $m_1 = 15$ meVÅ^2 for $(\mathrm{Bi_xSb_{1\text{-}x}})_2\mathrm{Te_3}$.[4] Since $m_0 m_1 < 0$, the system possesses an inverted band structure with parabolic dispersion. For a non-zero magnetization strength, the subbands undergo Zeeman splitting, as shown in panel b for $\lambda = 50$ meV. For a large enough magnetization strength, one pair of subbands ($E_{1,+}$ and $E_{1,-}$) looses the band inversion while the inversion becomes larger for the other two subbands ($E_{2,+}$ and $E_{2,-}$). The unprotected crossings between $E_{2,+}$ and $E_{2,-}$ open up a gap as soon as spin-orbit coupling is included, as shown in panel c. Below, it is shown that the band gap between the subbands opened by spin-orbit coupling is topological and gives rise to a chiral edge state, whereas the band gap between the other pair of subbands (without inversion) is trivial.

When the spin-orbit coupling strength is increased to the full value of $(\mathrm{Bi_xSb_{1\text{-}x}})_2\mathrm{Te_3}$ in Fig. 1.3d), the two subbands, $E_{2,+}$ and $E_{2,-}$, open up completely leading to a direct bandgap for the system of size: $E_{\mathrm{gap}} = 2(|m_0| - |\lambda|) = -90$ meV.[5] Note that in Fig. 1.3 the energy spectra are shown for an upward, out-of-plane magnetization ($\lambda > 0$). The scenario is reversed for the opposite magnetization direction, i.e. spin-orbit coupling will open a topological band gap between $E_{1,+}$ and $E_{1,-}$, while $E_{2,+}$ and $E_{2,-}$ remain trivial. Hence, irrespective of the magnetization direction, there will always be one set of topological

[4] The values used for m_0, m_1, λ, and v_{D} are the same as those for the KWANT simulations performed for the manuscript included in Chapter 2.

[5] Here, $E_{\mathrm{gap}} < 0$ is chosen for the QAHI regime, see also Eq. 1.7.

subbands and one trivial pair, as long as $|\lambda| > |m_0|$. This is also apparent when the total Chern number $\mathcal{C}$ is calculated for the system [13, 58]:

$$\mathcal{C} = \mathcal{C}_1 + \mathcal{C}_2 = \begin{cases} \lambda/|\lambda|, & \text{for} \quad |\lambda| > |m_0| \\ 0, & \text{for} \quad |\lambda| < |m_0| \end{cases}, \tag{1.7}$$

which is the sum of the Chern numbers for $H_1(k)$ and $H_2(k)$ in Eq. 1.3. Notice that the Chern number is independent of the sign of $m_0 m_1$, meaning that the QAHE can be realized irrespective of whether the parent system has a band inversion ($m_0 m_1 < 0$) or not ($m_0 m_1 > 0$) [5]. This means that as long as λ is large enough, it does not matter whether the $(Bi_xSb_{1\text{-}x})_2Te_3$ thin film is in the trivial insulator or quantum spin Hall insulator phase [41]. Hence, film thickness fluctuations are not detrimental for the realization of the QAHI phase.

A non-zero Chern number implies the presence of a 1D chiral edge state at the boundary of the QAHI and a trivial insulator (including the vacuum), see Fig. 1.3c-d. Surprisingly, it turns out that this chiral edge state is spinless, as can be seen from its wavefunction:

$$\psi(y, k_x = 0) = A\left(e^{-\beta_+ y} - e^{-\beta_- y}\right)\left(c^t_{k\uparrow} + \chi c^b_{k\downarrow}\right), \tag{1.8}$$

with

$$\beta_\pm = \frac{\hbar v_\mathrm{D} \pm \sqrt{\hbar^2 v_\mathrm{D}^2 + 4m_1(m_0 - \lambda)}}{2m_1}, \tag{1.9}$$

where the boundary between the QAHI and trivial insulator is chosen to be along the x-direction, A is a normalization factor, and χ parameterizes the asymmetry between the top and bottom surface, see Ref. [59] and Supplementary Note 9 in Chapter 2 for details. The wavefunction $\psi(y, k_x = 0)$ of the chiral edge state is an equal superposition of spin-up on the top-surface and spin-down on the bottom surface, leading to no net spin-polarization. Only when the inversion symmetry between the top and bottom surfaces is broken ($\chi \neq 1$), does the chiral edge state become spin-polarized in the in-plane direction.

1.3 Low-energy Effective Hamiltonian of a Proximitized QAHI

In this section, the superconducting proximity effect on a QAHI in contact to an s-wave SC is discussed. The Bogoliubov-de Gennes (BdG) Hamiltonian for a proximitized MTI is given by [13, 14]

$$\mathcal{H}_\mathrm{BdG}(k) = \frac{1}{2}\sum_k \Psi_k^\dagger H_\mathrm{BdG}(k)\Psi_k, \tag{1.10}$$

$$H_\mathrm{BdG}(k) = \begin{bmatrix} H_0(k) - \mu & \Delta_k \\ \Delta_k^\dagger & -H_0^*(-k) + \mu \end{bmatrix}, \tag{1.11}$$

$$\Delta_k = \begin{bmatrix} i\Delta_1\sigma_y & 0 \\ 0 & i\Delta_2\sigma_y \end{bmatrix}, \tag{1.12}$$

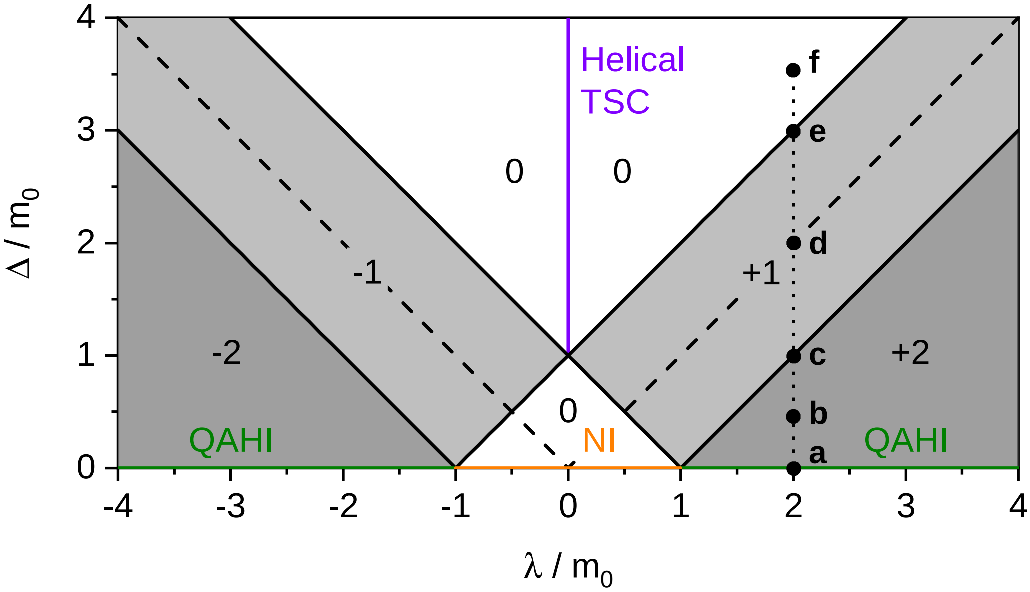

Fig. 1.4 | Phase diagram of the proximitized QAHI, with $\boldsymbol{\Delta = \Delta_1 = -\Delta_2}$ and $\boldsymbol{\mu = 0}$. The regions with different Chern number $\mathcal{N} = \pm 0$, ± 1, and ± 2 are colored in white, light gray, and dark gray, respectively. The solid black lines $\Delta/m_0 = \pm\lambda/m_0 \pm 1$ mark the band closings of the topological transitions. The dashed lines represent $\Delta = \pm\lambda$ and serve as a reference. The QAHI, normal insulator (NI), and helical TSC phases are marked by the green, orange, and purple lines, respectively. For the dotted line with labels 'a' to 'f', the corresponding energy spectra are plotted in Figs. 1.5a-f.

where $\Psi_k = [(c^t_{k\uparrow}, c^t_{k\downarrow}, c^b_{k\uparrow}, c^b_{k\downarrow}), (c^{t\dagger}_{-k\uparrow}, c^{t\dagger}_{-k\downarrow}, c^{b\dagger}_{-k\uparrow}, c^{b\dagger}_{-k\downarrow})]^T$. Here, Δ_1 and Δ_2 correspond to the pairing gaps for the top and bottom surface state respectively, and μ indicates the chemical potential.

For the simple case when $\Delta_1 = -\Delta_2 = \Delta$ and $\mu = 0$, an analytic solution can be found. After a basis transformation, the 8×8 Hamiltonian $H_{\mathrm{BdG}}(k)$ in Eq. 1.11 is block-diagonalized to

$$\tilde{H}_{\mathrm{BdG}}(k) = \begin{bmatrix} H_+(k) & 0 \\ 0 & H_-(k) \end{bmatrix}, \tag{1.13}$$

where

$$H_+(k) = \begin{bmatrix} h_{+,+}(k) & 0 \\ 0 & -h^*_{+,-}(-k) \end{bmatrix}, \tag{1.14}$$

$$H_-(k) = \begin{bmatrix} h^*_{-,-}(k) & 0 \\ 0 & -h_{-,+}(-k) \end{bmatrix}, \tag{1.15}$$

with $h_{\mathrm{a,b}} = \hbar v_{\mathrm{D}}(k_y\sigma_x - k_x\sigma_y) + [m(k) + \mathrm{a}\lambda + \mathrm{b}\Delta]\sigma_z$, where a and b can be $\pm$ 1 and Δ is assumed to be real. The eight eigenvalues then become:

$$E_{\mathrm{a,b},\pm} = \pm\sqrt{\hbar^2 v_{\mathrm{D}}^2(k_x^2 + k_y^2) + [(m_0 + \mathrm{a}\lambda + \mathrm{b}\Delta) + m_1(k_x^2 + k_y^2)]^2}, \tag{1.16}$$

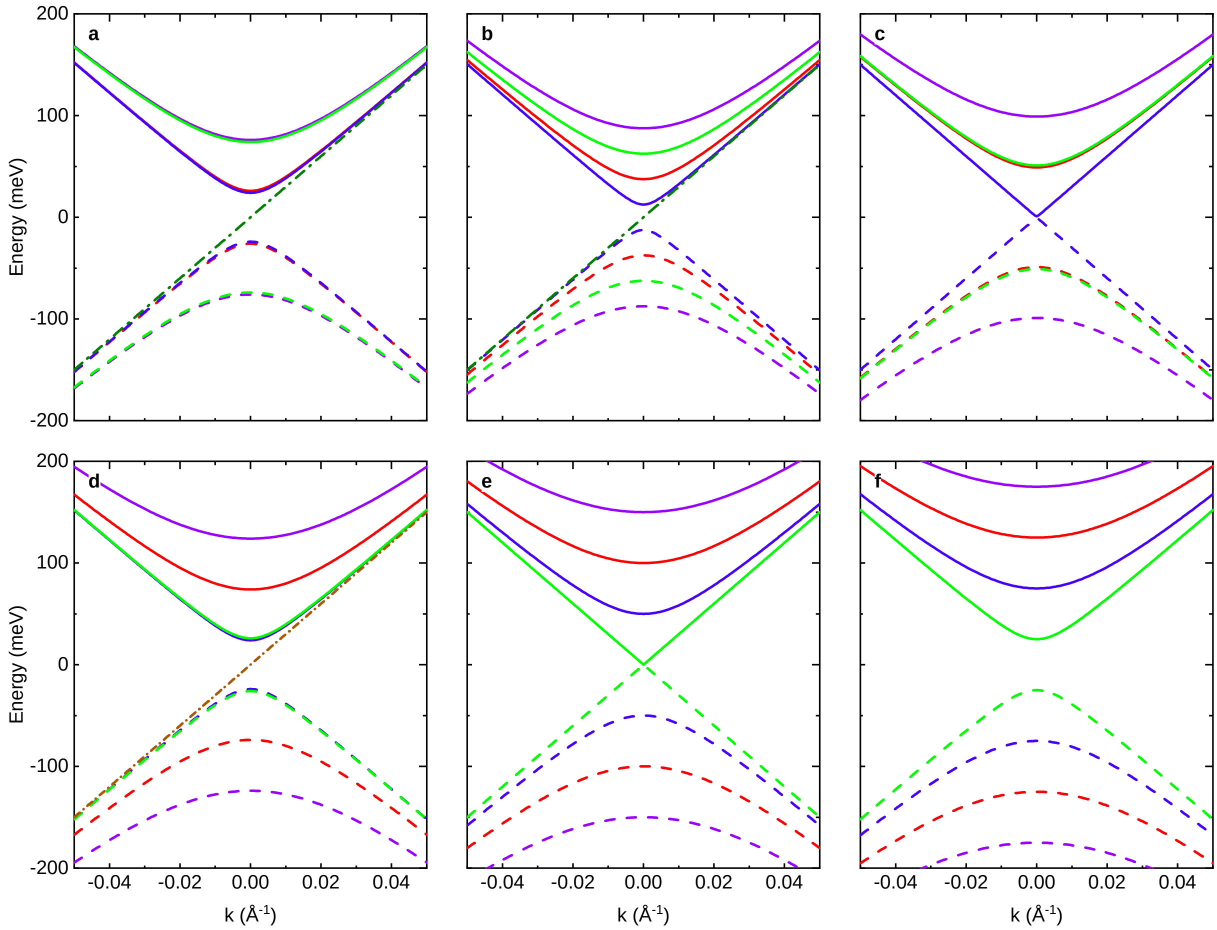

Fig. 1.5 | The energy spectra for the topological phase transition of a QAHI to TSC to normal SC, for the case of $\boldsymbol{\Delta = \Delta_1 = -\Delta_2}$ and $\boldsymbol{\mu = 0}$. The eigenvalues $E_{\mathrm{a,b},+}$ and $E_{\mathrm{a,b},-}$ (Eq. 1.16) are shown by the solid and dashed lines, respectively. The panels a to f correspond to the marked positions along the dotted line in the phase diagram of Fig. 1.4. **a**, QAHI phase ($\Delta = 0$), with band gap $E_{\mathrm{gap}} = 2(|m_0| - |\lambda|) = -50$ meV. The green dash-dotted line represents the 1D chiral Dirac fermion mode on the edge of the sample. **b**, $\mathcal{N} = +2$ TSC phase ($\Delta = 0.5|m_0|$). The green dash-dotted line represents the two degenerate 1D chiral Majorana fermion modes on the edge of the sample. **c**, Gapless superconducting phase ($\Delta = |\lambda| - |m_0|$). **d**, $\mathcal{N} = +1$ TSC phase ($\Delta = \lambda$), with band gap $E_{\mathrm{gap}} = -2|m_0| = -50$ meV. The brown dash-dotted line represents the single 1D chiral Majorana fermion mode on the edge of the sample. **e**, Gapless superconducting phase ($\Delta = |\lambda| + |m_0|$). **f**, Normal SC phase ($\Delta = 3.5|m_0|$). The material parameters used for generating this figure are $m_1 = 15$ meVÅ^2, $\lambda = 50$ meV, and $\hbar v_{\mathrm{D}} = 3$ eVÅ (as in Chapter 2), but the value for m_0 is increased from -5 meV to -25 meV ($= -\lambda/2$) to better visualize the gap opening and closing of the topological transitions.

and the Chern numbers for $H_+(k)$ and $H_-(k)$ are given by,

$$\mathcal{N}_+ = \begin{cases} -2, & \text{for } |\Delta| < -m_0 - \lambda, \\ -1, & \text{for } |\Delta| > |m_0 + \lambda|, \\ 0, & \text{for } |\Delta| < m_0 + \lambda, \end{cases} \tag{1.17}$$

$$\mathcal{N}_- = \begin{cases} 2, & \text{for } |\Delta| < -m_0 + \lambda, \\ 1, & \text{for } |\Delta| > |m_0 - \lambda|, \\ 0, & \text{for } |\Delta| < m_0 - \lambda, \end{cases} \tag{1.18}$$

respectively. The total Chern number of the system is then $\mathcal{N} = \mathcal{N}_+ + \mathcal{N}_-$ [13], and is visualized in Fig. 1.4 as a function of Δ and λ in units of m_0. The conditions in Eqs. 1.17-1.18 define straight lines, $\Delta/m_0 = \pm\lambda/m_0 \pm 1$, separating regions of different Chern number $\mathcal{N}$. For $\Delta = 0$, the system is in the QAHI phase when $|\lambda| > |m_0|$ (Eq. 1.7), as indicated by the green line in Fig. 1.4. This $\mathcal{C} = \pm 1$ phase with one chiral Dirac fermion mode on the edge of the sample is topologically equivalent to the $\mathcal{N} = \pm 2$ topological superconductor (TSC) phase with two chiral Majorana fermion modes on the edge. The energy spectrum for a QAHI with $\lambda = -2m_0$ and $\Delta = 0$ is shown in Fig. 1.5a.[6]

When Δ is increased from point 'a' to 'b' along the dotted line in Fig. 1.4, the $E_{\mathrm{a,b},\pm}$ bands (Eq. 1.16) split and the band gap starts to close, see Fig. 1.5b. For $\Delta/m_0 = \lambda/m_0 - 1$ at point 'c', the system becomes a gapless superconducting, see Fig. 1.5c. Increasing Δ beyond 'c' turns the system into the $\mathcal{N} = +1$ TSC phase with one chiral Majorana edge state. With increasing Δ, the band gap now increases, reaching a maximum at point 'd' when $\Delta = \lambda$ and $E_{\mathrm{gap}} = -2|m_0| = -50$ meV,[7] see Fig. 1.5d. When Δ is increased above 'd', the band gap decreases again and closes at point 'e', see Fig. 1.5e. Finally, for $\Delta/m_0 > \lambda/m_0 + 1$, the system is a normal SC with $\mathcal{N} = 0$, see Fig. 1.5f. Increasing Δ beyond point 'e' will only increase the trivial band gap. The phase diagram in Fig. 1.4 has a special region marked by the purple line, where $\Delta > m_0$ and TRS is not broken ($\lambda = 0$). Here, the system is in the helical TSC phase [13]. However, a discussion of this phase falls outside the scope of this thesis.

When inspecting the phase diagram in Fig. 1.4, several issues become clear, possibly hindering the realization of the $\mathcal{N} = +1$ TSC phase in real material systems: (i) While it is possible to make the MTI films very thin ($\sim$4 nm) to ensure a QAHI with a large m_0 of a few meV [60], the QAHI films in this thesis are $\sim$9 nm thick. For such thicknesses, the top and bottom surface states are well separated and m_0 will be very small [60]. For $m_0 = 0$ the phase diagram in Fig. 1.4 will have no region with $\mathcal{N} = \pm 1$, instead the $\mathcal{N} = \pm 2$ phase will directly transition to $\mathcal{N} = 0$, when $\Delta = \pm\lambda$ (dashed lines in Fig. 1.4). Hence, the region in the phase diagram with $\mathcal{N} = \pm 1$ is very narrow for realistic values of m_0. (ii) The $\mathcal{N} = +1$ TSC state requires a minimum size of the induced gap $\Delta > |\lambda| - |m_0|$, and the most robust $\mathcal{N} = +1$ TSC state is realized when $\Delta = |\lambda|$. For most MTIs, λ is of the order of tens of meV [61]. This is much larger than the superconducting gap of Nb used in this thesis as the SC material [62].

[6] This spectrum is the same as the spectrum shown in Fig. 1.3d, but with a smaller band gap $E_{\mathrm{gap}} = 2(|m_0| - |\lambda|) = -50$ meV, since m_0 is much larger in this example.

[7] Here, negative band gaps are chosen for the topological phases.

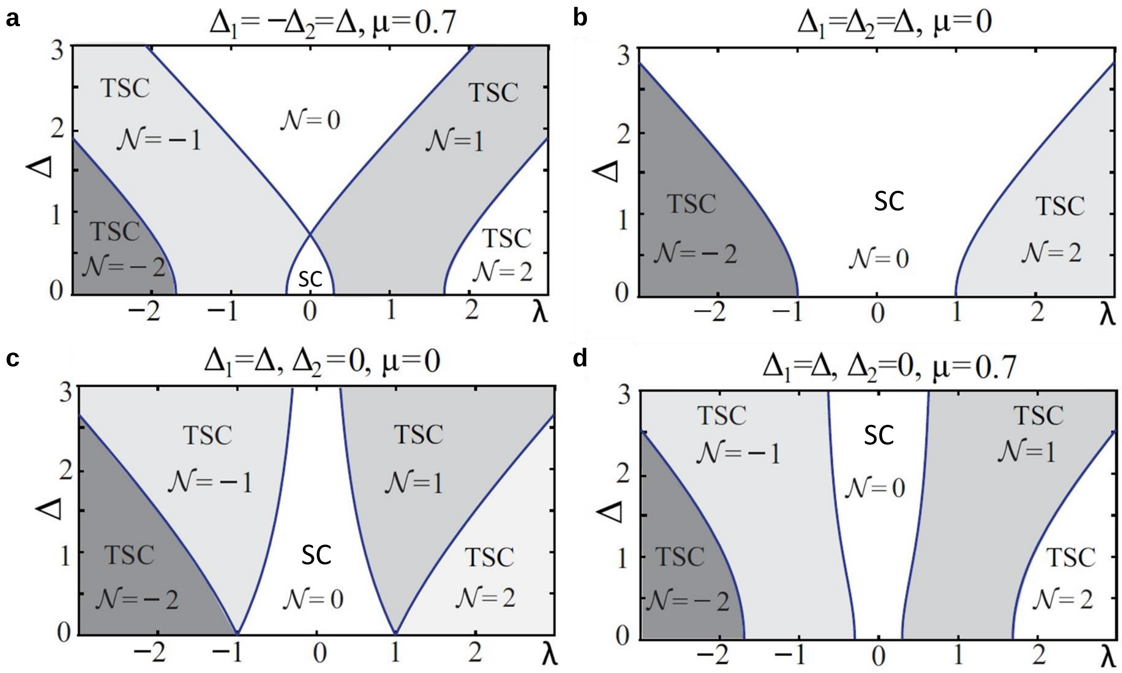

Fig. 1.6 | Phase diagram of the proximitized QAHI, for different choices of μ, Δ_1, and Δ_2. The values of Δ and λ are expressed in units of m_0. **a**, The special case of $\Delta_1 = -\Delta_2 = \Delta$ with nonzero chemical potential $\mu = 0.7$. Moving the chemical potential away from the center of the band gap increases the phase space for $\mathcal{N} = \pm 1$, compared to Fig. 1.4 with $\mu = 0$. **b**, When the top and bottom surface state have the same induced gap $\Delta_1 = \Delta_2 = \Delta$, there is no $\mathcal{N} = \pm 1$ TSC in the phase diagram. **c-d**, Only the top surface is proximitized ($\Delta_1 = \Delta$ and $\Delta_2 = 0$) for zero and finite chemical potential. Due to the broken inversion symmetry between the top and bottom surface, the $\mathcal{N} = \pm 1$ TSC phase space is maximized. Reprinted figure with permission from Ref. [13].

Luckily, there are two parameters in Eqs. 1.10-1.11, which are not explored yet: the chemical potential μ and the top-bottom asymmetry of the induced gaps (Δ_1 and Δ_2). Until now the situation with $\mu = 0$ and $\Delta_1 = -\Delta_2$ was discussed. Wang *et al.* simulated several phase diagrams for different choices of $\mu = 0$, Δ_1, and Δ_2 [13], shown in Fig. 1.6. Two important effects are observed: Firstly, including a nonzero μ, results in an extended region for $\mathcal{N} = \pm 1$ in Fig. 1.6d, as compared to Fig. 1.4. This can be understood by returning to Eq. 1.11, where the chemical potential μ sits on the diagonal of $H_{\mathrm{BdG}}(k)$. This means that the inclusion of μ is equivalent to adding a fourth mass term (in addition to m_0, λ, and Δ) [12]. By moving the chemical potential μ into the 2D conduction or valence band, the minimum size of Δ required to enter the $\mathcal{N} = \pm 1$ phase can be reduced to essentially zero. This situation arises naturally as most SCs contacting the MTI will dope the MTI due to metallization effects [63]. Secondly, notice that the key ingredient to the creation of the $\mathcal{N} = \pm 1$ phase is the broken-inversion symmetry between the induced gap on the top and bottom surface, Δ_1 and Δ_2, respectively. For $\Delta_1 = \Delta_2 = \Delta$, shown in Fig. 1.6b, there is no $\mathcal{N} = \pm 1$ phase. The system transitions directly from the $\mathcal{N} = \pm 2$ TSC to normal SC phase. Interestingly, the $\mathcal{N} = \pm 1$ region is the largest when only one of the surfaces in proximitized ($\Delta_1 = \Delta$ and $\Delta_2 = 0$), see Fig. 1.6c. The phase space

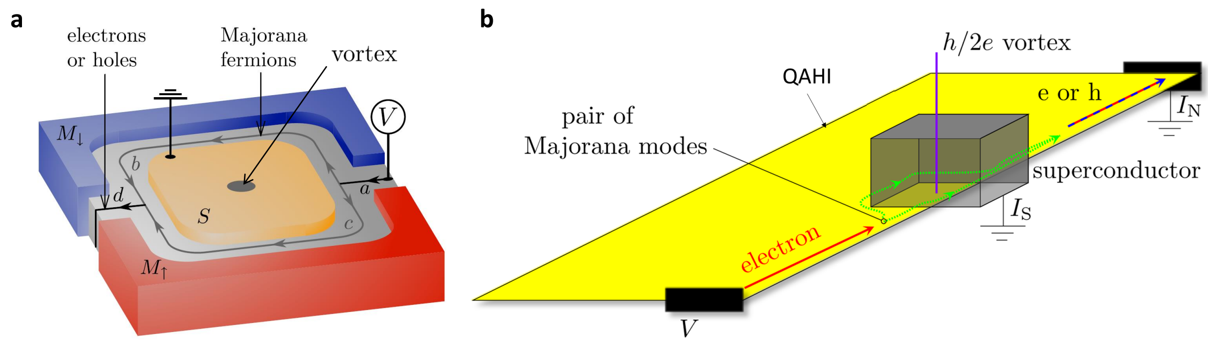

Fig. 1.7 | Majorana interferometer. **a**, Schematic of a 3D TI (grey region) covered by two ferromagnets with opposite magnetization; $M_\uparrow$ (red region) and $M_\downarrow$ (blue region). In the middle of this lies a superconducting island S (orange region). An incoming 1D chiral state with potential V (section 'a') splits into two CMEMs on arrival at the SC, taking different paths (sections 'b' and 'c') around the superconducting island. The CMEMs recombine at section 'd' as an electron or hole, depending on the number of vortices enclosed by the SC is even or odd, respectively. Note that the figure shows the simplest case where the SC has a single vortex. Reprinted figure with permission from Ref. [64] © Copyright (2009) by the American Physical Society. **b**, Illustration of a QAHI thin film (yellow region) with a grounded SC (grey region) contacting one of the 1D chiral edge channels. There are two normal contacts at the ends of the QAHI serving as the source and drain, respectively. An incident electron with potential V splits into a pair of Majorana modes which takes two opposite paths around the SC, indicated by the green dotted lines. Depending on the number of vortices enclosed, the Majorana fermions combine into a hole or electron, denoted by the red and blue dashed line respectively. Note that I_S is the supercurrent entering the grounded SC and I_N is the current through the normal contact acting as the drain. This figure was taken from Ref. [26] with permission.

for $\mathcal{N} = \pm 1$ can then be increased further by increasing the amplitude of the chemical potential ($\mu = 0 \to 0.7$), compare Figs. 1.6a and 1.6b. This leads to the conclusion that the best choice for realizing the $\mathcal{N} = \pm 1$ phase seems to be a rather thick QAHI film covered with the s-wave SC, where only the top surface is proximitized ($\Delta_1 = \Delta$ and $\Delta_2 = 0$) and the SC strongly charge dopes the surface states of the QAHI film ($|\mu| \gg 0$). For such a system a small value for Δ or m_0 are not detrimental.

Hence, coupling a QAHI to an s-wave SC can lead to a 2D TSC, hosting CMEMs. The charge-neutral nature of CMEMs makes their detection extremely challenging. There are a few theoretical proposals based on interference experiments to probe the existence of CMEMs in the TSCs [64, 66]. These proposals rely on a 3D TI with a grounded superconductor island on top. The inclusion of two magnets with opposite out-of-plane magnetization directions ensures that a magnetic domain wall is formed in the 3D TI, i.e. sections 'a' and 'd' in Fig. 1.7a. This magnetic domain wall host a 1D chiral mode, which splits in two CMEMs moving around the superconducting island (sections 'b' and 'c'). When the two CMEMs recombine in 'd', either an electron or hole is injected into the 1D chiral mode leaving from the SC depending on the number of vortices in the superconductor island. Note that this 'Majorana interferometer' is naturally realized when a grounded superconducting electrode covers one edge of a QAHI, see Fig. 1.7b. In this case, no additional magnets are needed and it is the 1D chiral edge state of the QAHI

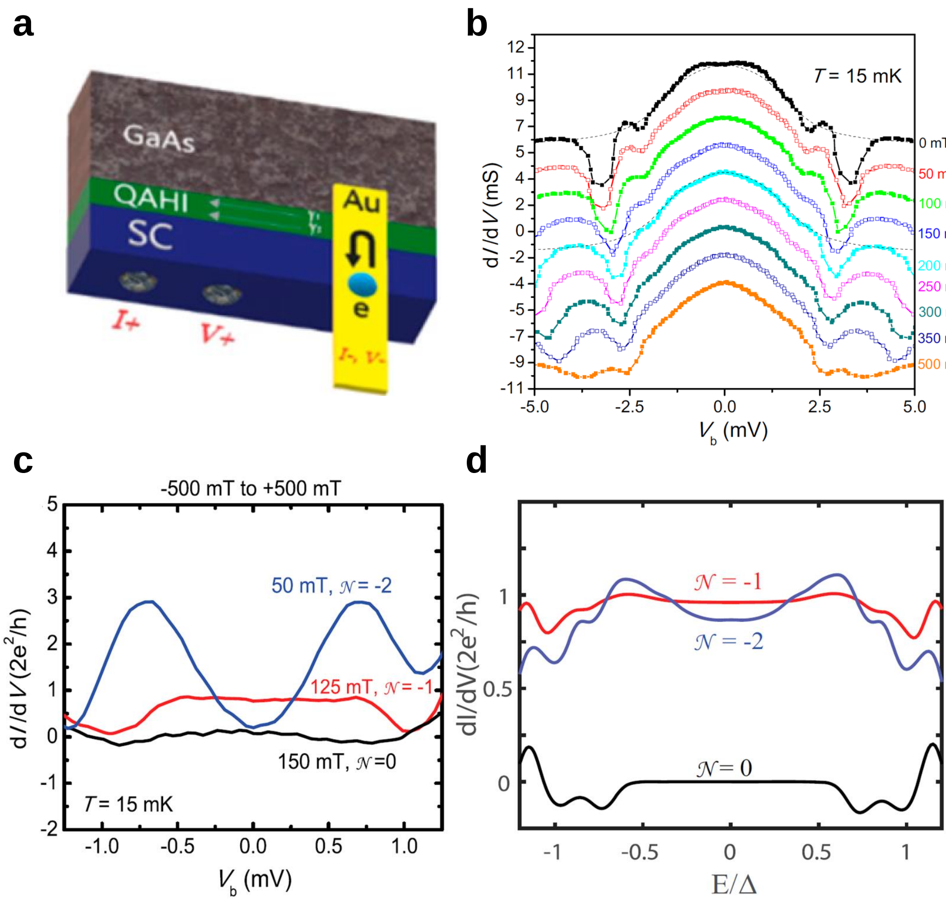

Fig. 1.8 | Point-contact spectroscopy on a SC-QAHI heterostructure. **a**, Schematic of the point-contact device on the edge of a SC-QAHI heterostructure. A 200-nm thick Nb layer is deposited on a 6-nm thick QAHI thin film, which is grown on a GaAs(111) substrate. The device has normal contacts on the surface of the superconducting Nb and point contacts made of 200 to 500-nm wide thin Au strips across the edge of the heterostructure. The arrow represents the Andreev process. Note that the real thin film dimensions were 5 $\times$2 mm^2, and the sketch is not to scale. **b**, The raw differential conductance dI/dV spectra for the point-contact set-up is shown for different applied magnetic fields at T = 15 mK. The broad peak around zero bias voltage (V_{b}) is attributed to AR at the Nb-Au interface. Note that the black dashed lines at the 0-mT and 200-mT curves are fits with the BTK model (with the effective barrier $Z = 0.01$, the superconducting gap $\Delta = 1.6$ meV, broadening parameter $\Gamma = 0.6$ meV), which points to a highly transparent Nb-Au interface. **c**, Selected background subtracted differential conductance (dI/dV) data at different applied magnetic field as the magnetic field is swept from -500 mT to +500 mT, and the magnetization direction of the sample switches at 175 mT. The raw dI/dV spectra at 175 mT is used for the background subtraction. Three different topological regimes are identified, and the curves are marked with their respective Chern numbers $\mathcal{N}$. **d**, For three selected magnetization strengths $\lambda = 0.01m_0(\mathcal{N} = 0)$, $-1.2m_0(\mathcal{N} = -1)$, and $-1.85m_0(\mathcal{N} = -2)$, the simulated d$I$/d$V$ spectra are shown as a function of bias voltage energy (E) normalized by Δ. The simulated curves are qualitative agreement with the experimental data shown in panel c. This figure is taken from Ref. [65], with copyright (2020) National Academy of Sciences.

which splits into the two CMEMs taking different paths around the edge of the SC. When the CMEMs encircle an odd number of vortices, then the incoming electron with potential V from the source enters the SC as a Cooper pair, which results in a hole with potential $-V$ being ejected into the 'downstream' 1D chiral edge state leaving from the SC. When the CMEMs encircle an even number of vortices, an electron is ejected into the downstream edge state and no supercurrent flows into the superconducting electrode.

These CMEMs are still Majorana fermions with fermionic exchange statistics, meaning they cannot be used to perform non-abelian braiding operations. Several theoretical proposals take advantage of the chiral nature of the edge of a proximitized QAHI and use a Josephson junction to inject edge vortices into the CMEMs [15–18]. An edge vortex is a π-phase domain wall containing a Majorana zero mode (MZM) and such edge vortices can be exchanged in real space, unlike the immobile MZM residing in a superconducting vortex core or at nanowire endpoints. However, a prerequisite for these advanced measurement schemes is the experimental verification of the superconducting proximity effect in a QAHI.

1.4 Experiments on SC-QAHI heterostructures

A quantized two-terminal conductance of $e^2/(2h)$ was proposed as evidence for chiral Majorana edge modes at the SC-QAHI interface [13, 23–25]. In chapter 3, an overview of the theory and experiments associated with the half-integer conductance will be discussed. Based on our own Landauer-Büttiker (LB) analysis and experimental data, it is shown that this half-integer quantized conductance is the result of equilibration of the two chiral edge modes arriving at the superconducting electrode (in agreement with Ref. [29]) and that this equilibration is also present in the absence of superconductivity, and hence not related to the superconducting proximity effect.

Another study claimed the spectroscopic evidence of CMEMs in a proximitized QAHI thin film, using point contacts made of thin Au strips on the edge of Nb–Cr-doped $(Bi_xSb_{1-x})_2Te_3$ heterostructures [65]. The sketch of such a device is shown in Fig. 1.8a. The device is said to have high interface transparency with a contact resistance of $< 100\ \Omega$. The raw differential conductance $\mathrm{d}I/\mathrm{d}V$ data shown in Fig. 1.8b is primarily shaped by a broad peak centered at zero bias, which corresponds to the Andreev reflections at the Nb-Au interface. This is confirmed by the fit of the BTK model to the data taken at 0 mT and 200 mT, represented by the black dashed lines in Fig. 1.8b. The differential conductance data were recorded as the applied magnetic field was swept from -500 mT to 500 mT, and the magnetization of the sample is inverted. Shen *et al.* argue that the $\mathrm{d}I/\mathrm{d}V$ spectrum at 175 mT corresponds to the situation of $\lambda < m_0$ (Eq. 1.7) [65], i.e. the QAHI is in the trivial insulating state without a chiral edge state. This leads the authors to conclude that the $\mathrm{d}I/\mathrm{d}V$ spectrum at 175 mT only includes the contribution from the Nb-Au interface, and that the superconducting proximity effect in the Cr-doped $(Bi_xSb_{1-x})_2Te_3$ film is completely suppressed. The $\mathrm{d}I/\mathrm{d}V$ spectra at different magnetic fields are then compared after performing a background subtraction with the spectrum at 175 mT.

Three selected $\mathrm{d}I/\mathrm{d}V$ spectra are shown in Fig. 1.8c, accompanied by the simulated spectra in Fig. 1.8d calculated using the Hamiltonian in Eq. 1.10. Comparing the experimental and simulated curves, a transition of a dip-like feature at 50 mT to a plateau at 125 mT is observed, followed by its disappearance at 150 mT. These changes with magnetic field are interpreted as two different topological phase transitions [65]. Namely, the fully magnetized QAHI transitions from $\mathcal{N} = -2 \rightarrow -1 \rightarrow 0$ as the magnetic domains in the Cr-doped $(Bi_xSb_{1\text{-}x})_2Te_3$ film flip to align with the applied magnetic field. This reduce the value of λ to zero, when the magetization of the sample vanishes at the coercive field. This corresponds to moving on a horizontal line $(-\lambda/m_0 \rightarrow 0)$ in the phase diagram shown in Fig. 1.4. However, a few issues should be raised for this work. Firstly, the assumption that the chemical potential of the Cr-doped $(Bi_xSb_{1\text{-}x})_2Te_3$ thin film underneath the Nb layer is lying in the 2D exchange gap is highly unlikely, as it is known that the SC dopes the (M)TI surface that lies beneath it [14, 63]. This means that for low bias voltages at 175 mT ($\mathcal{N} = 0$) there can still be contributions from the 2D or even 3D bulk states of the Cr-doped $(Bi_xSb_{1\text{-}x})_2Te_3$ thin films, which is not considered in the analysis. These bulk states might be responsible for the features observed in Fig. 1.8c. Secondly, the majority of the side contacted area lies on the Nb layer (as seen in the device sketch in Fig. 1.8a), and the broad peak centered at zero bias stemming from the Nb-Au interface dominates the raw $\mathrm{d}I/\mathrm{d}V$ spectra in Fig. 1.8b. Hence, it is difficult to dismiss trivial effects at the Nb-Au interface as a possible origin for the features in Fig. 1.8c.

A separate study by the same group reported an observation of a conductance peak that slowly evolves into a single zero-bias peak in the presence of an external magnetic field on QAHI nanoribbons coupled to an s-wave SC, attributed to the formation of MZMs at the end of the proximitized MTI nanoribbon [67]. However, it is well-established by now that the mere observation of a zero-bias peak is not convincing evidence for MZMs as it can also be explained by trivial Andreev bound states or weak antilocalization by disorder in the superconducting nanowire [68, 69]. Moreover, for narrow structures ($\lesssim 20\ \mu$m) the breakdown of the QAHE also results in a conductance peak at zero bias since at large biases the conduction takes place through the dissipative bulk [53].[8] In conclusion, neither Ref. [65] nor Ref. [67] give convincing evidence for the realization of the TSC phase in their respective SC-QAHI heterostructures.

1.5 Inducing Superconducting Correlations via Andreev Processes

Until now, the superconducting proximity effect was discussed in terms of an induced superconducting gap in the Hamiltonian describing the material system. A different but equivalent way of describing the superconducting proximity effect is by evaluating the possibility for Andreev processes to occur at the SC-Q(A)HI interface. In Chapter 2 of this thesis, Hall-bar devices in which one edge of the QAHI is contacted by a narrow superconducting electrode are investigated. In addition to Majorana interference (Fig. 1.7), there are different Andreev processes that can occur at such a SC-QAHI interface.

In this section, an overview will be given of the most important experimental studies that report induced superconducting correlations in similar device structures on quantum Hall

[8] For instance, compare the sharp dip in $\mathrm{d}V/\mathrm{d}I$ at zero bias due to the breakdown of the QAHE in Fig. 3b of Ref. [53] with the zero-bias peak in $\mathrm{d}I/\mathrm{d}V$ in Fig. 3a-b of Ref. [67].

insulators (QHIs). Like the QAHI, this 2D system with broken TRS also offers a platform to couple the chiral 1D edge modes to a SC. The experiments outlined below served as the primary motivation for this thesis and inspired the results presented in Chapter 2. Two important distinctions have to be made here between a QAHI and a QHI. Firstly, a QAHI does not require an external magnetic field and its remnant magnetization is only ~4 mT (see Supplementary Note 13 in Chapter 2 for details). This implies that there are no strict requirements regarding the choice of SC. In order to proximitize a QH system, on the other hand, a SC with a high critical field is necessary since a large external magnetic field is required for the formation of Landau levels. Superconducting alloys such as NbN [20, 70, 71], NbTiN [72], MoRe [73, 74] are used for this purpose, and were shown to make highly transparent contacts with graphene and III-V semiconductor 2DEGs. Secondly, the spin-polarized $\nu = 1$ filling factor of the QHI resembles the QAHI edge, but with the key difference that the latter is not fully spin polarized [59].

Below three different processes are discussed: Local Andreev reflection in the metallic phase of a QH and QAH sample, the formation of chiral Andreev edge states in a QHI, and lastly crossed Andreev reflection in a QHI.

Local Andreev Reflection

The 2DEG illustrated in Fig. 1.9a is in a metallic state in the absence of an applied magnetic field. A single electron with energy eV smaller than the superconducting gap (Δ_{SC}) cannot enter the grounded SC due to the energy gap at the E_{F} in the density of states of the SC. However, an electron is allowed to enter the SC by forming a Cooper pair, while a hole is retroreflected to the source of the electron. This phenomenon is known as (local) Andreev reflection (AR). According to the Blonder-Tinkham-Klapwijk (BTK) theory [75], the transparency of an SC-metal interface is given by $t = 1/(1 + Z^2)$, where the barrier strength was characterized by a parameter Z ranging from 0 for an ideal metallic contact to ∞ for a tunnel barrier with vanishing transparency. The Andreev process becomes prominent for high transparency, which leads to a sub-gap conductance of maximum twice the normal-state conductance for a perfect contact ($Z = 0$). This reflects the dual charge transfer mechanism, or in other words the effective doubling of the applied current [76].

In 2017, Lee *et al.* [20] investigated the transparency of the SC-graphene interface by measuring the differential conductance, shown in Fig. 1.9b. Here, the differential conductance is given by $\sigma = dI_{\text{a-d}}/dV_{\text{e-c}}$, where $I_{\text{a-d}}$ is the current flowing from contact a to d and $V_{\text{e-c}}$ is the voltage drop between contact e and c (see inset of Fig. 1.9c). A large backgate voltage was applied such that the graphene 2DEG remained 2D conducting with a negligible sample resistance contribution at large magnetic fields. Note that in Fig. 1.9b, σ was normalized by the conductance at 13 K, which is above the critical temperature (T_{c}) of the SC. The normalized σ shows an enhancement of ~45% up to a bias voltage of ~1 mV in the absence of a magnetic field, pointing at a reasonable interface transparency. Figure 1.9c shows the AR probability (P_{AR}) at different magnetic fields, which was extracted by performing a BTK fit [20]. The amplitudes of σ and P_{AR} are suppressed by increasing the applied magnetic field as seen in Fig. 1.9b-c, indicative of the gradual suppression of superconductivity in the NbN electrode resulting in reduced AR.

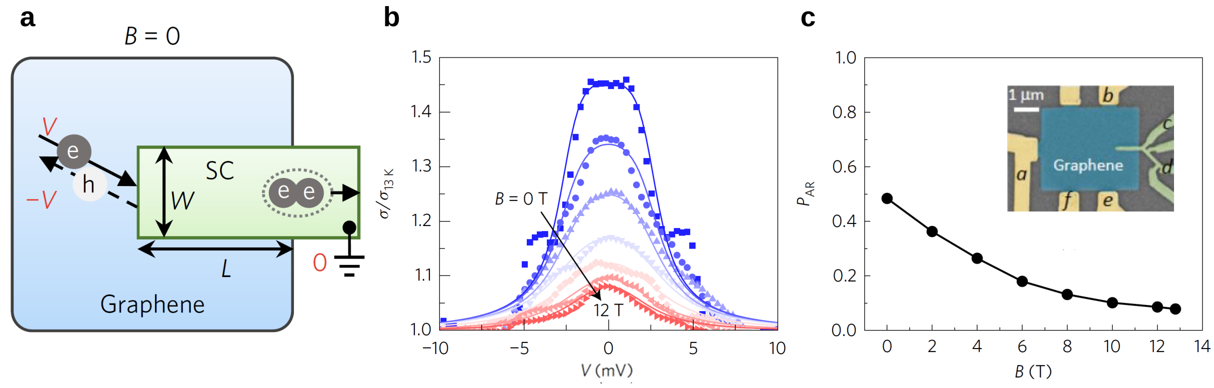

Fig. 1.9 | Magnetic field dependence of Andreev reflection at the NbN-graphene interface. a, Illustration of local AR, where an incoming electron 'e' with potential 'V' retroreflects as a hole 'h' with potential '$-V$' at the interface with the grounded SC in the absence of an external magnetic field. The blue (green) region corresponds to the 2DEG (SC). L and W are the length and width of the SC electrode contacting the 2DEG. **b**, The differential conductance at $T = 1.8$ K normalized with the respective values at $T = 13$ K for different magnetic fields at $V_{\text{bg}} = 60$ V. At $T = 13$ K, NbN is no longer in the superconducting state. The additional normal-state resistance contribution of the NbN electrode was subtracted from $\sigma_{13\text{K}}$ before performing the normalization of $\sigma/\sigma_{13\text{K}}$. The symbols are the experimental data which are well-fitted with the modified BTK theory (represented by the solid lines) with $Z = 0.018$. **c**, The AR probability (P_{AR}) is also estimated from the modified BTK fit. The inset shows the image of the device configuration. This figure is taken from Ref. [20] with permission from SNCSC.

In a similar experiment, Kayyalha *et al.* [29] characterized the SC-MTI interface quality by fabricating narrow SC electrodes of width $W_{\text{Nb}} \approx 200$ nm on top of Cr-doped $(\text{Bi}_x\text{Sb}_{1\text{-}x})_2\text{Te}_3$ thin films, and performing differential conductance measurements. Figure 1.10 shows the upstream ($\sigma_{\text{U}} = I_{6\text{-}8}/V_{7\text{-}8}$) and downstream conductance ($\sigma_{\text{D}} = I_{6\text{-}8}/V_{9\text{-}8}$) normalized by their respective values at $T = 6$ K, above the $T_c \approx 5$ K of the Nb finger electrode. Here, the terminology 'upstream' and 'downstream' refers to the chiral flow of the 1D edge state arriving at and leaving from the superconducting electrode, respectively. The metallic phase of the QAHI was realized by applying a large backgate voltage, tuning the chemical potential out of the exchange gap. The experimental data shows an increase of $\sim$80% with respect to the differential conductance value at $T = 6$ K in zero applied magnetic field. This enhancement cannot be fully attributed to AR at the SC-MTI interface, as it also includes the metal-to-superconductor transition induced by the critical current of the Nb finger. After taking into account the normal-state Nb resistance, the interface conductance enhancement due to AR is estimated to be $\sim$47% [29], indicative of a highly transparent interface. This constitutes the first experimental realization of the superconducting proximity effect in a MTI, i.e. the enhancement of σ by $\sim$47% due to AR proofs that the 2D surface states (and potentially also the 3D bulk states) are proximitized. However, no signatures of Andreev processes were observed when the MTI was tuned into the QAHI phase as the breakdown of the QAHE dominated the measured $\text{d}I/\text{d}V$ [29]. Hence, whether the superconducting correlations can be induced into the 1D chiral edge states remains to be verified. This is the topic of chapter 2.

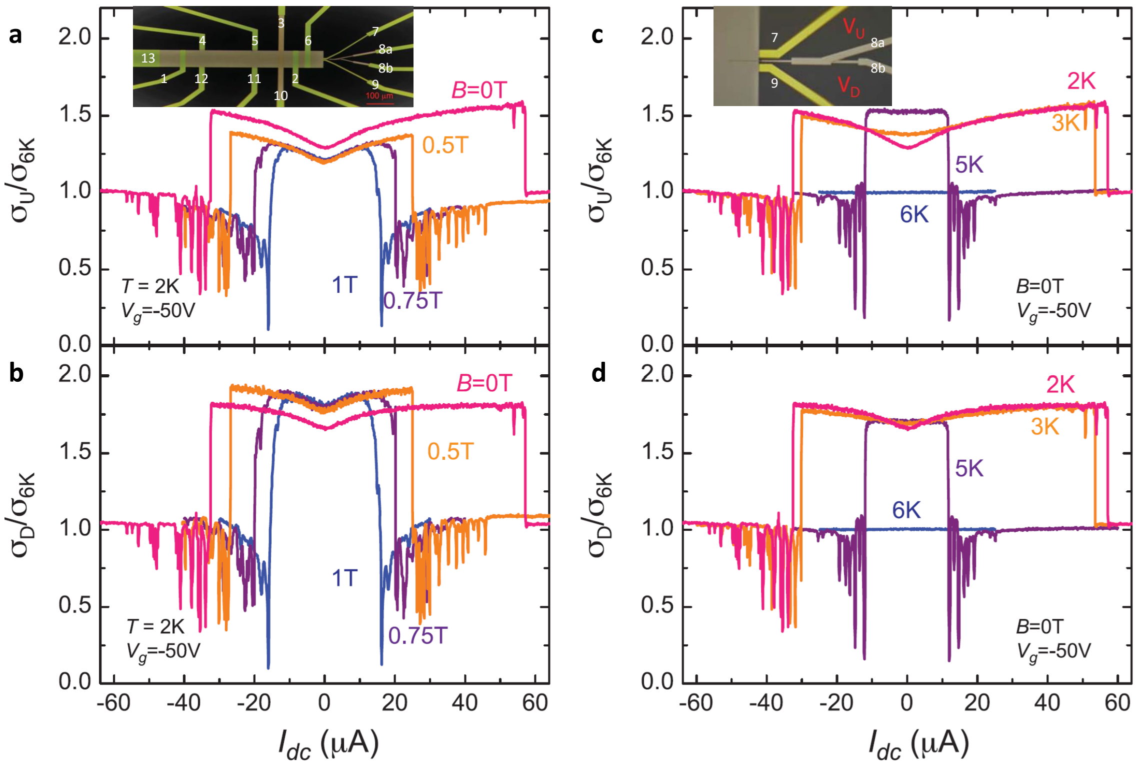

Fig. 1.10 | Interface transparency in the SC-MTI finger device. **a-b**, The normalized upstream (σ_U) and downstream (σ_D) differential conductance of the SC-MTI finger device (see the insets) for different magnetic fields at $T = 2$ K with $V_{bg} = -50$ V. **c-d**, The temperature dependence of the normalized upstream (σ_U) and downstream (σ_D) at $V_{bg} = -50$ V without an applied magnetic field. The hysteresis in all the panels is attributed to Joule heating from the highly resistive MTI layer. This figure is taken from Ref. [29]. Reprinted with permission from AAAS.

Chiral Andreev Edge States

In the presence of a magnetic field, the electron transport predominantly occurs via the 1D chiral edge states in the QH regime due to the emergence of Landau levels which gap out the bulk of the 2DEG. This chiral nature is expected to alter the physics of Andreev reflection at the SC-QH interface [77,78]. Moreover, the type of Andreev processes observed also depends on the relation between the width of the superconducting electrode (W_{SC}) and the superconducting coherence length (ξ_S).

Let us first discuss the regime where $W_{SC} \gg \xi_S$, illustrated in Fig. 1.11a. For a probability for Andreev reflection of $P_{AR} = 100\%$, the incident electron undergoes consecutive Andreev reflections along the edge of the SC electrode, forming what is known as chiral Andreev edge states (CAESs) [20]. In the semi-classical picture, these CAESs are a series of alternating skipping orbits of electrons and holes, propagating in the direction determined by the cyclotron frequency, $\omega_c = eB/m$, where m gives the effective mass, e is the charge, and B is the magnetic field strength. As Andreev reflection flips the signs of both m and e, the cyclotron motion continues in the same direction for electrons and holes, maintaining a single chirality for the CAES [79].

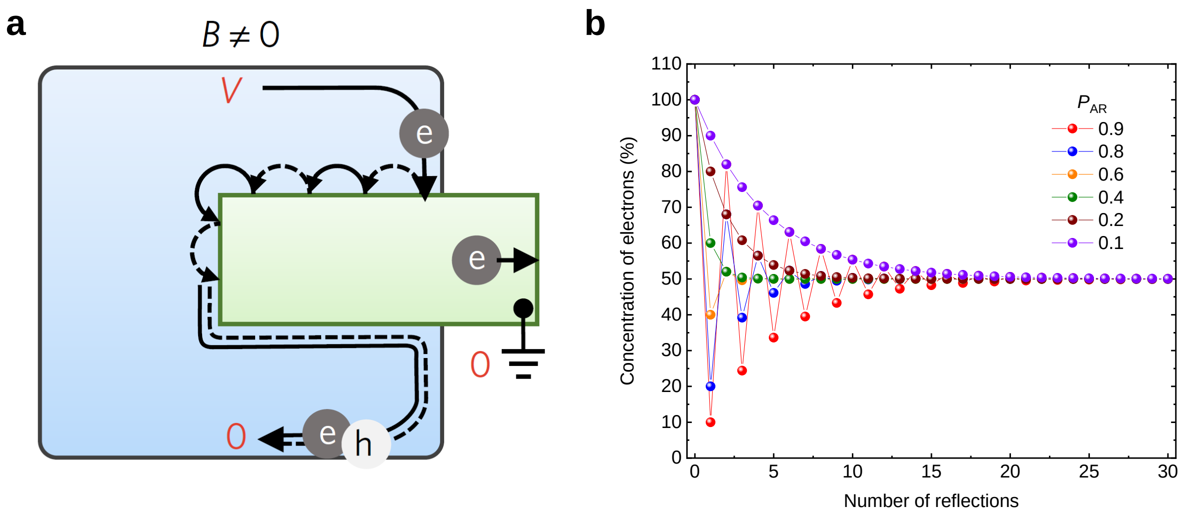

Fig. 1.11 | Semi-classical representation of the CAESs. a, The formation of a CAES along the SC-QHI interface in the presence of an applied magnetic field B for a long and wide grounded SC electrode. The blue (green) region corresponds to the 2DEG (SC). After many skipping orbits at the SC-2DEG interface the CAES becomes an equal mixture of electron 'e' and hole 'h' character, acquiring the same potential as the grounded SC ($V = 0$). This figure is taken from Ref. [20] with permission from SNCSC. **b**, The semi-classical calculation of the concentration of electrons in the CAES after a certain number of reflections along the SC electrode. The Andreev and normal probabilities for a single reflection are P_{AR} and $1 - P_{\mathrm{AR}}$, respectively.

However, the probability for Andreev reflection will generally be finite, as an incoming electron can also undergo normal refection. For a long SC electrode coupled to a QHI, this will result in the CAESs quickly becoming an equal mixture of electron and hole after a couple of reflections at the SC-QH interface, resulting in a downstream potential equal to the chemical potential of the grounded SC (see Fig. 1.11a). This can be demonstrated using a simple statistical argument [20], see Fig. 1.11b. Assuming that $P_{\mathrm{AR}} = 0.9$ for a single reflection and the incoming current consists of 100% electrons, then upon the first reflection 90% is Andreev reflected as holes while 10% is normal reflected as electrons. After the second reflection, the CAES consists of 82% electrons (1% of the 10% electrons normal reflected and 81% of the 90% holes Andreev reflected). This process continues and after a few reflections, the CAES consists of 50% electrons and 50% holes. This corresponds to one electron on average being transferred into the SC for every incoming electron. Figure 1.11b showcases how easy it is for incoming electrons to transform into an equal mixture of electron and hole depending on the value of P_{AR}. Interestingly, for any P_{AR} except when close to 0 and 1, the current leaving from the SC will be an uniform mixture of electron and hole within about 20 reflections. In the work by Lee *et al.* [20], 20 reflections corresponds to < 200 nm of travel distance for an electron along the SC at $B = 8$ T with a magnetic length of about 10 nm [20].

Quantum mechanically, combining Andreev reflection with the QH creates fermionic modes, where electron and hole states hybridize and travel chirally along the SC-QH interface with different wavevectors. In other words, the 1D edge state becomes a superposition of electron and hole, as displayed in Fig. 1.12a [74, 78]. Experimentally, this is probed by measuring the voltage at the downstream normal metal contact with respect to the grounded superconducting contact [20, 72, 74]. According to the Landauer-Büttiker (LB) formalism, the expression for the corresponding intrinsic downstream resistance (R^i_{D}) is then

$$R^{\mathrm{i}}_{\mathrm{D}} = \frac{h}{\nu e^2}\left(\frac{T^{\mathrm{ee}} - T^{\mathrm{eh}}}{1 - T^{\mathrm{ee}} + T^{\mathrm{eh}}}\right), \tag{1.19}$$

where ν is the filling factor and T^{ee} (T^{eh}) is the transmission probability of an electron from the upstream channel to arrive at in the downstream channel as an electron (hole), with $T^{\mathrm{ee}} + T^{\mathrm{eh}} = 1$. For a long CAES, $T^{\mathrm{ee}} = T^{\mathrm{eh}} = 0.5$ is expected, which indeed gives $R^{\mathrm{i}}_{\mathrm{D}} = 0$. However, for short interactions with the SC electrode ($T^{\mathrm{ee}} \neq T^{\mathrm{eh}}$), R_{D} can become nonzero, and even negative when $T^{\mathrm{eh}} > 0.5$. This means more holes than electrons are arriving in the downstream channel.

Zhao *et al.* [74] fabricated devices on graphene encapsulated in hexagonal boron nitride with normal (Cr/Au) and superconducting (MoRe) contacts. The induced superconducting coherence length and the phase coherence of the QH edge state are calculated to be 160 nm and 12 μm [74], respectively. The width of the superconducting electrode was 600 nm, falling between these two values, such that the crossed Andreev reflection (CAR) contribution (discussed below) is suppressed. The device geometry is shown in Fig. 1.12b. The downstream resistance (R_{D}) is measured in a three-terminal measurement set-up, and includes different resistance contribution,

$$R_{\mathrm{D}} = \frac{V_{\mathrm{D}}}{I} = R_{\mathrm{QHI}} + R_{\mathrm{SC}} + R_{\mathrm{contact}} + R^i_{\mathrm{D}}, \tag{1.20}$$

where the sample resistance (R_{QHI}) is zero in the QHI state, the resistance of the SC section lying on the substrate between the film edge and the SC contact (R_{SC}) is zero in the superconducting state, the extrinsic contact resistance (R_{contact}) is negligible for the 600-nm-wide contact in this device, and the intrinsic downstream resistance (R^i_{D}) is the CAES contribution given by Eq. 1.19. This reduces the Eq. 1.20 to $R_{\mathrm{D}} = R^i_{\mathrm{D}}$ when graphene (or the 2DEG) is in the QHI regime and the SC is in the zero-resistance state.

Figure 1.12c shows the Landau fan diagram for R_{D}, with an overall response similar to the typical Landau fan diagram of the longitudinal resistance of a QHI. Note that the standard behavior of longitudinal resistance is that it is zero at the QH plateaus and positive for the regions in-between. The observation of R_{D} being nonzero at the QH plateaus is attributed to the formation of CAESs along the grounded superconducting contact c. In particular, R_{D} seems to strongly fluctuate between positive and negative values when changing the gate voltage or applied magnetic field. This corresponds to $T^{\mathrm{eh}} < 0.5$ and > 0.5 in Eq. 1.19, respectively. The fluctuations in the sign of R_{D} can be explained in the quantum-mechanical picture: Along the SC-QHI interface the superconductor couples the electron edge state with the hole edge state at the same energy, forming a pair of CAES for each electron state. The two CAESs develop a phase difference, stemming from their different wavevectors, as they propagate along the superconducting interface causing mesoscopic fluctuations in the sign and amplitude of R_{D}. When R_{D} is negative (positive), the CAES interference produces a hole (electron) in the downstream QH edge states leaving the SC contact. This hole (electron) will lower (raise) the chemical potential with respect to the grounded superconducting contact c, and travel downstream to contact d [74]. The fluctuations in R_{D} are clearly observed for $\nu = 2$ and $\nu = 6$ highlighted by the

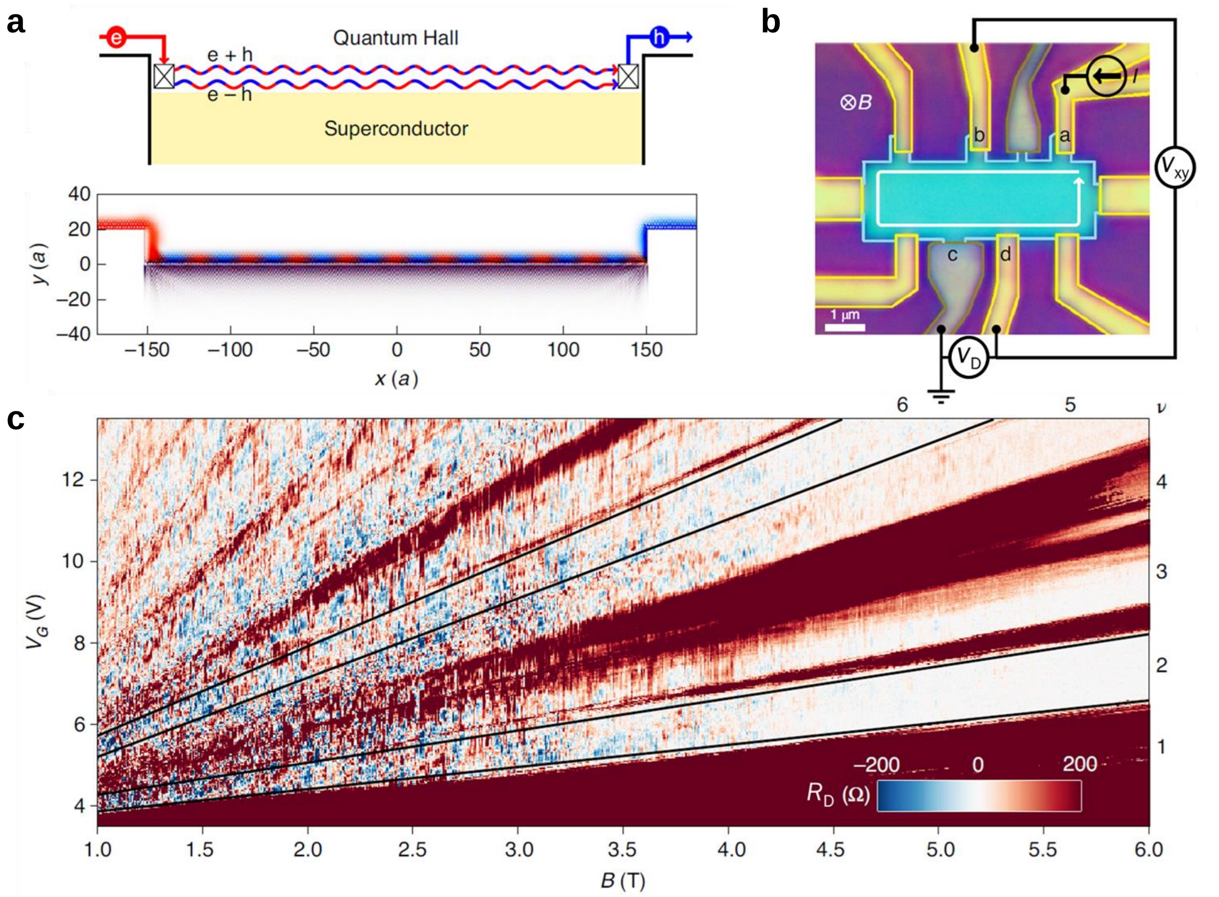

Fig. 1.12 | The interference of CAESs along the SC-QHI edge. **a**, The pictographic representation of the CAESs as a superposition of electron and hole states, where the $e + h$ and $e - h$ states propagate along the SC-QHI interface with different wavevectors. The wavefunction densities of electron e (red) and hole h (blue) are calculated using a tight-binding model, with the dimensions in units of the lattice parameter a of graphene. **b**, The three-terminal measurement geometry is shown using an optical image of the sample. The 1D edge state(s) propagates in the counter-clockwise direction for a downwards, out-of-plane magnetic field. The current enters on contact a and contact c is grounded. The hall voltage ($V_{\mathrm{xy}} = V_{\mathrm{d}} - V_{\mathrm{b}}$) and the downstream voltage ($V_{\mathrm{D}} = V_{\mathrm{d}} - V_{\mathrm{c}}$) are measured simultaneously. The yellow and grey region correspond to the normal and superconducting contacts, respectively. **c**, The R_{D} is plotted as function of the gate voltage V_{G} and magnetic field B. The black lines represent the QH plateaus at $\nu = 2$ and $\nu = 6$. The mesoscopic fluctuations in R_{D} are suppressed with increasing magnetic field. This figure is taken from Ref. [74] with permission from SNCSC.

black lines in Fig. 1.12c. As the superconducting proximity effect is gradually suppressed by increasing the applied magnetic field, the amplitude of the fluctuations in R_{D} is visibly reduced.

In 2022, Hatefipour *et al.* [72] reported on similar experiments involving InAs-based quantum wells. The cross-sectional schematic of the device is depicted in Fig. 1.13a. A multi-terminal hall-bar is fabricated on InAs with 90-nm thick superconducting contacts (NbTiN), as shown in Fig. 1.13b. Contacts 1, 2, 3, 5, and 6 are metallic electrodes, while contact 4 is the superconducting electrode. Note that the SC makes a top-contact to the InAs, unlike the works on graphene discussed in this section [20, 74], where the graphene was etched to form a side contact to the SC (see Fig. 1.14c below). Moreover, the width of the SC-2DEG interface is 150 μm, which is much wider than for the SC-graphene devices [20, 74]. The study in Ref. [72] discusses the results of two devices. Device A includes a deliberate pre-surface cleaning step before the sputter deposition of the SC, aimed at understanding the role of interface quality in inducing superconductivity in QH edge modes. This step is omitted for device B. Figures 1.13c-d show R_{D} as a function of both the applied magnetic field B and the gate voltage V_{g}. For this measurement the current is injected through contact 1 while grounding contact 4". The Hall resistance, measured between contacts 2 and 5, enables the authors to identify the filling factors ν for the Landau fan diagrams of devices A-B in Figs. 1.13c-d, respectively. The value of R_{D}, measured between contacts 5 and 4', is negative when the system is tuned into the QH plateaus (for even filling factors ν). This negative R_{D} is attributed to the emergence of CAESs along the SC-2DEG boundary, indicating that superconducting correlations are induced in the 1D egde modes [72]. The negative amplitude of R_{D} is significantly larger in device A with the additional interface cleaning step during the device fabrication as compared to device B, indicative of a stronger superconducting proximity effect in device A than B.

The authors used the LB formalism to obtain a detailed understanding of the experimental data [72]. Since the 2DEG is in the QHI regime, the SC is in the superconducting state, and the contact resistance is negligible for such large contacts, then Eqs. 1.19-1.20 can be rewritten with $T^{\mathrm{ee}} + T^{\mathrm{eh}} = 1$ as,

$$R_{\mathrm{D}} = R_{\mathrm{D}}^{\mathrm{i}} = \frac{h}{\nu e^2}\left(\frac{1}{2T^{\mathrm{eh}}} - 1\right), \tag{1.21}$$

The extracted transmission probability of Andreev reflection (T^{eh}) from the experimental data is 55% [72], which is large in comparison to the SC-graphene systems [20]. In addition, the persistently negative R_{D} for such a wide SC interface (150 μm) without any fluctuations in the sign of R_{D} in the QH plateaus of the Landau fan diagram (Fig. 1.13c-d) is another striking difference to the earlier work by Zhao *et al.* [74] (Fig. 1.12c). The authors provide two possible explanations [72]: (i) The dephasing of the electron-like and hole-like edge modes along the SC-QH interface might be negligible, corresponding to the regime with small proximity-induced superconducting pairing (Δ_{SC}) and long coherence length (ξ_{S}). (ii) The lack of fluctuations in R_{D} with neither the applied magnetic field nor the gate voltage may point to a scattering process at the superconducting electrode that preferentially drains electrons, causing more holes to end up in the downstream channel even if $T^{\mathrm{eh}} \ll 0.5$. Note that such a scattering process breaks the particle-hole symmetry.

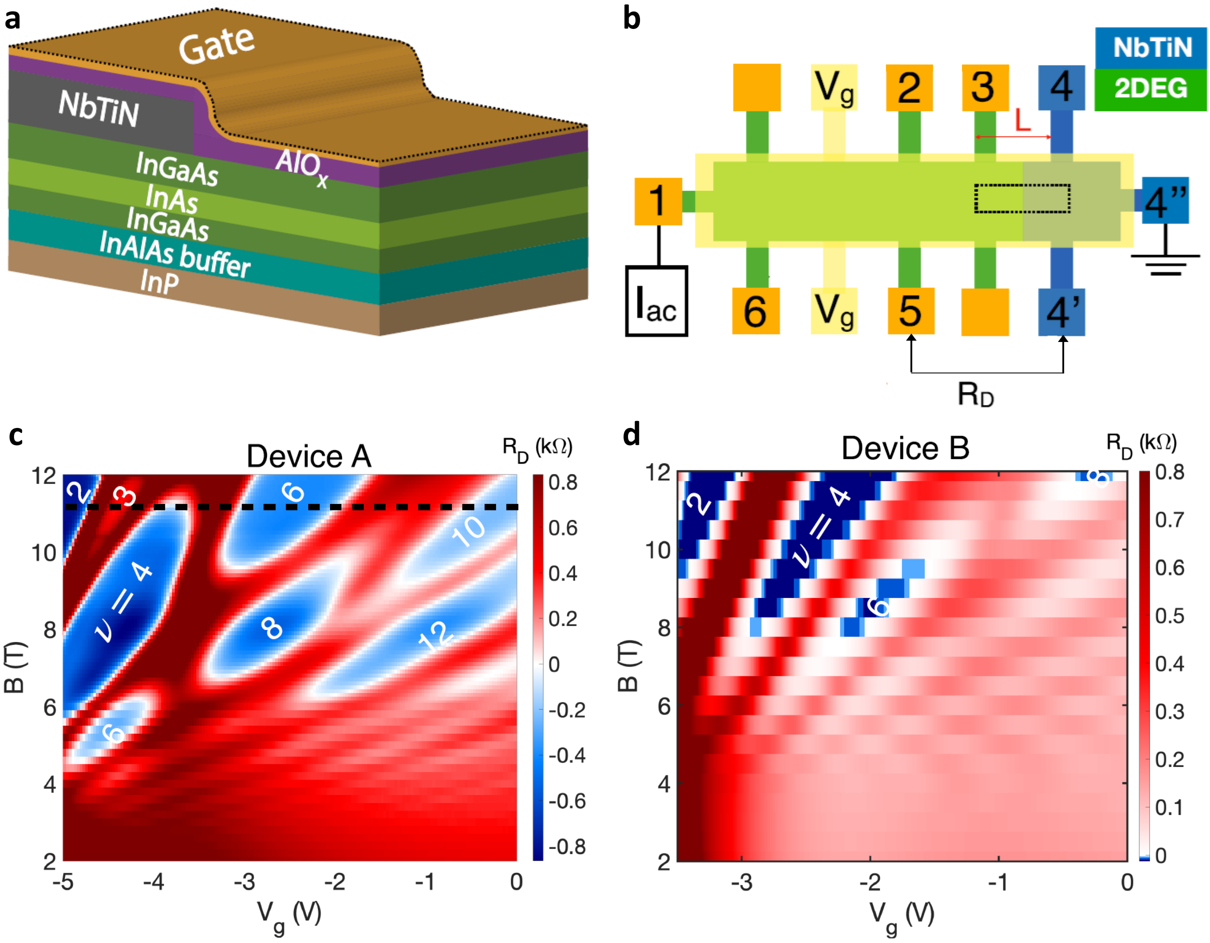

Fig. 1.13 | CAESs along the SC-QHI edge of an InAs quantum well device. **a**, Illustration of the cross-section of the gated NbTiN-InAs device, corresponding to the small section outlined by the rectangle in panel b. **b**, The schematic of the multi-terminal InAs hall-bar device (green) and measurement set-up. The NbTiN superconducting contacts (blue) are 4, 4', 4"; the normal metal contacts (dark yellow) are 1, 2, 3, 5, and 6. The potential of the top-gate (light yellow) is given by V_g. Contacts 1 and 4" are the source and drain, respectively. R_D is measured between contacts 5 and 4', where L is the horizontal separation between two consecutive electrodes. **c**, Measured R_D as a function of B and V_g in device A with a high interface quality. **d**, Measured R_D as a function of B and V_g in device B with low interface quality. The filling factors (ν) mark the QH plateaus in the Landau fan diagrams in panels c and d. Reprinted figure with permission from Ref. [72]. © Copyright (2022) by the American Chemical Society.

Crossed Andreev Reflection

In this section two nonlocal mechanisms are addressed that can take place when $W_{\mathrm{SC}} \ll \xi_{\mathrm{S}}$. Electron co-tunneling (CT) across a narrow superconducting electrode is a quantum transport process in which an electron crosses from the upstream channel arriving at the SC to the downstream channel leaving from the SC without creating a Cooper pair in the superconducting electrode. For crossed Andreev reflection (CAR), on the other hand, an incoming electron (e) with potential V forms a cooper pair to enter the grounded SC by taking an electron from the other side of the SC, see Fig. 1.14a. The converted hole (h) with a potential $-V$ then continues to move forward on the other side of the SC with the chirality of the 1D QH edge state. This regime is particularly fascinating because a long ($L \gg hv_{\mathrm{F}}/\Delta$, h is Planck's constant) and narrow ($W_{\mathrm{SC}} \ll \xi_{\mathrm{S}}$) superconducting electrode coupling the counter-propagating QH edge states with Fermi velocity (v_{F}) is predicted to host two Majorana zero modes, one at the end of the SC and the other in resonance with the 1D chiral edge state, as depicted in the inset of Fig. 1.14a.

Lee *et al.* [20] fabricated multi-terminal hall-bar devices with narrow superconducting (NbN) electrodes of different widths, to investigate the CT and CAR processes in the QH edge states of graphene. The measurement configuration is shown in Fig. 1.14b, where the normal contact 'a' is the source and the superconducting contact 'd' is the drain. The chiral 1D QH edge states are propagating clockwise at the edge of the sample. The upstream (V_{U}) and downstream (V_{D}) potential are measured between contact pairs b-c and e-c, respectively. All the contacts were fabricated by an *in situ* etching technique of the hBN-encapsulated graphene samples, in order to maintain low contact resistance. The normal electrodes are made of Ti/Au and the superconducting contact is NbN which is reactive sputtered in Ar/ N_2 environment. As a result of the employed fabrication recipe, there is no graphene underneath the NbN electrode but a narrow wedge-shaped trench in graphene that is side-contacted by the SC, as shown in Fig. 1.14c.

Recalling Eq. 1.19 for the intrinsic downstream resistance derived using the LB formalism, it is clear that the sign of $R^{\mathrm{i}}_{\mathrm{D}}$ depends on the relative amplitudes of T^{ee} and T^{eh}. We can now express these transmission probabilities as $T^{\mathrm{ee}} = T^{\mathrm{CT}} + T^{\mathrm{N}}$ and $T^{\mathrm{eh}} = T^{\mathrm{CAR}} + T^{\mathrm{A}}$, where T^{CT} (T^{CAR}) represents the nonlocal CT (CAR) process and T^{N} (T^{A}) represents the probability for an electron (hole) to arrive in the downstream channel after travelling along the SC-graphene interface in the CAESs. Using the same statistical argument as above (see Fig. 1.11), the CAESs are expected to become an equal superposition of electron and hole for the device shown in Fig. 1.14b. This means that $T^{\mathrm{N}} = T^{\mathrm{A}}$, combining Eqs. 1.19-1.20 then give the expression for the measured downstream resistance

$$R_{\mathrm{D}} = \frac{V_{\mathrm{D}}}{I} = \frac{h}{\nu e^2}\left(\frac{T^{\mathrm{CT}} - T^{\mathrm{CAR}}}{1 - T^{\mathrm{CT}} + T^{\mathrm{CAR}}}\right) + R_{\mathrm{QHI}} + R_{\mathrm{SC}} + R_{\mathrm{contact}}, \tag{1.22}$$

where the first term in the summation is the intrinsic downstream resistance $R^{\mathrm{i}}_{\mathrm{D}}$, and $R_{\mathrm{QHI}} = 0$ at integer filling factors. Figure 1.14d shows R_{D} as a function of the filling factor ν for different temperatures T, for a graphene device with a 50-nm-wide superconducting electrode. For filling factors, $\nu = 1$, 2, and 6, R_{D} is negative indicating that the CAR process dominates over CT ($T^{\mathrm{CAR}} > T^{\mathrm{CT}}$) [20].

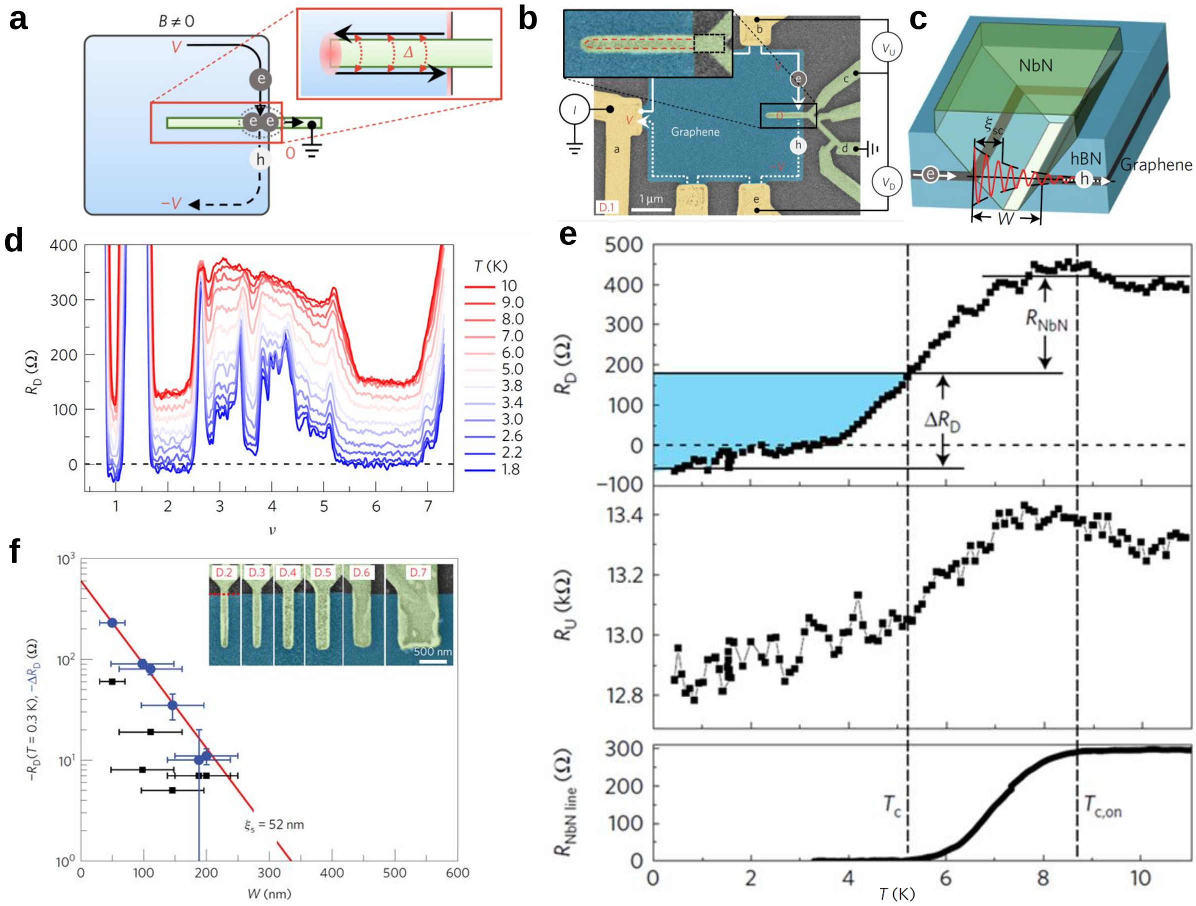

Fig. 1.14 | Negative downstream resistance stemming from CAR at a narrow superconducting electrode contacting a QHI. a, Illustration of the CAR process at a narrow superconducting electrode (green) contacting a QHI (blue) in an applied magnetic field B. Inset of a, the black arrows represent the counter-propagating 1D edge channels of the QHI coupled via the superconducting gap (Δ) leading to the formation of non-abelian MZMs at the ends of the superconducting electrode. **b**, False-color scanning electron microscopy (SEM) image of the SC-QHI device, showing the measurement set-up. Graphene (blue) is contacted by Ti/Au normal contacts (yellow) and a 50-nm-wide NbN superconducting contact (green). Inset of b, the dashed red line highlights the side-contact of NbN to the graphene edge. **c**, The cross-sectional schematic of the NbN contacting the graphene edge. ξ_S represents the superconducting coherence length. **d**, The raw downstream resistance R_D as a function of the filling factor (ν), obtained by sweeping the gate voltage V_g at different temperatures T in an applied magnetic field of $B = 14$ T. The width of the NbN electrode is $W_{SC} = 50$ nm for this device. **e**, Temperature dependence of R_D (top), R_U (middle) and $R_{\text{NbN line}}$ (bottom) for $\nu = 2$ at $B = 8$ T. The blue-shaded region is the change in downstream resistance ΔR_D attributed to CAR at the 50-nm-wide NbN electrode. The curve for R_U in the middle panel mirrors the changes in R_D. The temperature dependence of $R_{\text{NbN line}}$ has an onset critical temperature of $T_{c,\text{ on}} = 8.7$ K, and a critical temperature of $T_c = 5.2$ K below which the NbN electrode reaches the zero-resistance state. **f**, The exponential width dependence of R_D (square symbols) and ΔR_D (circle symbols) at 0.3 K, fitted by $\Delta R_D(W_{SC}) = \Delta R_{D,0} \exp(-W_{SC}/\xi_S)$. All devices with $W_{SC} \lesssim 200$ nm showcase a finite negative raw signal. The inset shows the SEM images of the devices with $W_{SC} = 98$, 111, 146, 188, 200, 600 nm, from left to right, respectively. This figure is taken from Ref. [20] with permission from SNCSC.

Lee *et al.* used the temperature T as a tuning knob to probe the evolution of R_D as the superconductivity is lost in the NbN finger electrode with increasing temperature. Note, that the magnetic field can not be changed as freely, since a large field is required to maintain the graphene in the QH regime at a particular filling factor. Figure 1.14e shows the temperature dependence of both $R_\mathrm{D} = V_\mathrm{D}/I$ and $R_\mathrm{U} = V_\mathrm{U}/I$ for $\nu = 2$, for a device with a 50-nm-wide NbN electrode. In order to determine the normal-state resistance and critical temperature (T_c) of NbN, a small separate section of the NbN electrode was measured independently, see the bottom panel of Fig. 1.14e. The NbN electrode resistance $R_\mathrm{NbN\ line}$ has an onset critical temperature of $T_\mathrm{c,on} = 8.7$ K and enters the zero-resistance state below $T_\mathrm{c} = 5.2$ K. Comparing the different panels in Fig. 1.14e, R_D and R_U are observed to gradually drop around $T_\mathrm{c,on} = 8.7$ K, with R_D eventually becoming negative once the NbN electrode is fully superconducting. The change in R_D of $\sim$250 Ω between $T_\mathrm{c,on}$ and T_c is attributed to the contribution from the small section of the NbN electrode (R_SC in Eq. 1.22), highlighted by the black dashed box in the inset of Fig. 1.14b. After subtracting this NbN resistance contribution, the remaining $\sim$180 Ω at T_c originates from the contact resistance contribution of the SC-graphene interface (R_contact in Eq. 1.22) [20]. The change in R_D is then defined as, $\Delta R_\mathrm{D} = R_\mathrm{D}(T = 0.3\mathrm{K}) - R_\mathrm{D}(T = T_\mathrm{c}) = R^\mathrm{i}_\mathrm{D}$, indicated by the blue-shaded region in the top panel of Fig. 1.14e. The value of $\Delta R_\mathrm{D} = -230\ \Omega$ is considerably larger than the raw value of R_D at the base temperature (0.3 K) and is an estimate for the total contribution of the CAR and CT processes across the superconducting finger electrode. This corresponds to approximately 4% of the maximum negative ΔR_D value, $-h/4e^2$ ($\nu = 2$) under ideal conditions for 100% CAR, according to the LB formalism. This reduced ΔR_D value is stated as a consequence of magnetic-field-induced quasiparticle excitations in the SC in addition to the diminished probability for Andreev processes at the SC-graphene interface due to the large applied magnetic field of $B = 8$ T [20].

In order to estimate the characteristic length-scale associated with the observed CAR process, the width dependence was studied by varying the superconducting electrode width W_SC from 50 nm to 600 nm for different graphene devices, see the inset of Fig. 1.14f. Both R_D (square symbols) and ΔR_D (circle symbols) exhibit an exponential decay with increasing W_SC, see Fig. 1.14f. The data is fitted using the exponential function, $\Delta R_\mathrm{D}(W) = \Delta R_\mathrm{D,0} \exp(-W/\xi_\mathrm{S})$ with $\Delta R_\mathrm{D,0} = -600 \pm 27\ \Omega$ and $\xi_\mathrm{S} = 52 \pm 2$ nm. The extracted value of ξ_S is in agreement with the expected coherence length of NbN, as it lies in-between the clean ($\xi_\mathrm{BCS} = \hbar v^\mathrm{S}_\mathrm{F}/\pi\Delta \sim 200$ nm) and dirty ($\sqrt{\xi_\mathrm{BCS} l_\mathrm{mfp}} \sim 10$ nm) limits of NbN, with the Fermi velocity of NbN $v^\mathrm{S}_\mathrm{F} = 1.8 \times 10^6\ \mathrm{ms}^{-1}$, the superconducting gap $\Delta = 1.8$ meV at $B = 8$ T, and the mean free path $l_\mathrm{mfp} = 0.3$ nm [20].

In a different study [70], Gül *et al.* also observed CAR in the fractional quantum Hall insulating state of graphene contacted by sub-100-nm-wide NbN superconducting electrodes [70]. Negative nonlocal downstream resistances were observed for several fractional filling factors $\nu = 1/3,\ 2/5,\ 2/3,\ 5/3$. This provides a platform to synthesize parafermions that obey rich non-abelian statistics [80]. However, the observed signatures of CAR were rather weak compared to the integer QHI phase of graphene reported above [20]. The suppression of the negative nonlocal downstream resistance occurred either when the bulk contribution dominated resulting in nonquantized Hall resistance, or when the superconductivity in NbN was suppressed with increasing temperature.

Note that the amplitude of R_{D} observed by Lee *et al.* [20] (and Gül *et al.* [70]) is persistently negative (Fig. 1.14), signaling that CAR always dominated over CT. Moreover, the amplitude of R_{D} in Fig. 1.14f shows a strong dependence on the width of the SC disappearing for superconducting electrodes wider than a few hundred nms [20]. The study by Zhao *et al.* (Fig. 1.12), on the other hand, showed fluctuations in the sign of R_{D} [74], meaning that for the CAESs formed along the 600-nm-wide SC-QHI interface the T^{ee} and T^{eh} processes are competing with each other (see Eq. 1.19). This, in turn, contrasts strongly with the persistently negative R_{D} observed by Hatefipour *et al.* for a 150-μm-wide superconducting contact on an InAs quantum well (Fig. 1.13) [72]. In conclusion, the negative R_{D} observed for the extremely wide superconducting electrode in Ref. [72], as well as the apparent dominance of Andreev processes over normal reflections at the SC-QHI interface in Ref. [20, 70, 72] remain open questions.

In chapter 2, the downstream resistance will be characterized for similarly narrow SC-QAHI hybrid structures as shown in Fig. 1.14b, but with the import distinction that the V-doped $(Bi_xSb_{1\text{-}x})_2Te_3$ thin film is not etched underneath the SC. In chapter 3, multi-terminal Hall-bar devices with large (μm-size) superconducting electrodes lying across the full width of the V-doped $(Bi_xSb_{1\text{-}x})_2Te_3$ thin films will be investigated.

Chapter 2

Induced Superconducting Correlations in a Quantum Anomalous Hall Insulator

This chapter is presented in the form of a manuscript and is published in Nat. Phys. as

A. Uday,* G. Lippertz,* K. Moors, H. F. Legg, R. Joris, A. Bliesener, L. M. C. Pereira, A. A. Taskin, and Y. Ando, *Induced superconducting correlations in a quantum anomalous Hall insulator*, Nature Physics, 20, 1589–1595 (2024)

A. A. T. and Y. A. conceived the project. A. U., G. L., A. B., and A. T. did the MBE growth of the ferromagnetic thin films. A. U. optimized the fabrication recipe for acquiring a transparent SC-QAHI interface. A. U. and G. L. did the device fabrication. A. U. did the transport data acquisition and analysis, with the help of G. L., A. A. T., and Y. A. K. M. and H. F. L. gave the theoretical interpretation for the manuscript. R. J. and L. M. C. P. measured the sample's remnant magnetization using SQUID magnetometry. A. U., Y. A., H. F. L., and K. M. wrote the manuscript with input from all authors.

2.1 Overview

This chapter discusses the first report of the observation of CAR across a narrow superconducting electrode lying on top of a QAHI, indicative of induced superconducting correlations in the chiral edge of a QAHI.

In this work, a ferromagnetic TI thin film of V-doped $(Bi_xSb_{1\text{-}x})_2Te_3$ is grown on InP(111)A using MBE. Our samples give a quantized Hall resistance ($R_{yx} = h/e^2$) and vanishing longitudinal resistance with coercive field peaks, confirming that our samples are in the QAHI regime without the need for electrostatic gating. This is a major advantage, as it opens up the top surface of the films for other structures than a gate stack. This allows the fabrication of Hall-bar devices on these films which are contacted by the superconducting Nb-electrodes with widths ranging from 160 to 520 nm (devices A-E), proximitizing the TI surface state as well as maintaining the QAHI state in the rest of the film. The normal contacts were made of Ti/Au.

*A. U. and G. L. contributed equally to this work.

In Ref. [20] discussed in the introduction, the nonlocal resistance is measured as the temperature is increased above the upper critical temperature of the SC for a narrow superconducting electrode contacting a QHI, see Fig. 1.14e. This allows the authors to compare R_D when the SC is in the normal and superconducting state. For a QAHI the temperature is not a good tuning knob, since the zero-resistance state is quite fragile and not maintained for temperatures above ~100 mK (see Supplementary Note 6), which is much less than the critical temperature of the SC. On the other hand, an external magnetic field is not required for the realization of the QAHE (unlike the quantum Hall effect) allowing us to study R_D as a function of the applied magnetic field from 0 T to above the upper critical field of Nb. Another striking difference is that in Refs. [20, 74] the SC is side-contacting the QHI, whereas in this work the SC makes a top-contact to the QAHI. Hence, unlike in the SC-QHI system, there are two SCs to be considered in our experiment: The parent SC which is the Nb-electrode, and the proximitized V-doped $(\mathrm{Bi_xSb_{1\text{-}x}})_2\mathrm{Te}_3$ thin film. If the proximity effect results in a topological superconductor (TSC) underneath Nb, then the $\mathcal{N} = 1$ phase is most-likely realized as the Nb is known to electron-dope TIs and the the inversion symmetry is broken between the top and bottom surface of the QAHI film, see Fig. 1.6d. This means that for an upward out-of-plane magnetization ($M > 0$) one chiral Majorana edge mode (CMEM) will run clockwise along the TSC-QAHI interface and another CMEM counterclockwise along the TSC-vacuum interface. These two CMEMs will then interfere when recombined ejecting either an electron or hole into the downstream QAHI edge state depending on the number of vortices enclosed by the SC [26, 64, 66]. Instead, if the proximity effect results in a trivial superconductor (SC) underneath Nb, then chiral Andreev edge states (CAESs) are formed at the SC-QAHI interface. These CAESs states will accumulate a phase difference as they travel clockwise along the SC-QAHI interface for $M > 0$, ejecting either an electron or hole into the downstream QAHI edge state when they recombine. Lastly, the nonlocal CAR and CT processes can also result in electrons and holes in the downstream edge state. These CAR and CT processes can be mediated by the parent SC (Nb) or via the proximitized SC (which can be trivial or topological).

The magnetic field dependence of device A with the narrowest Nb electrode width ($W_\mathrm{Nb} =$ 160 nm) shows that R_D is negative when Nb is in the superconducting state ($H < H_{c2}$). The observation of negative R_D is the highlight of this work and is attributed to the CAR process taking place across the narrow superconducting electrode, inducing superconducting correlations in the chiral edge states of the QAHI. Majorana interference or the presence of CAES are excluded as the possible origins of the negative resistance, as the long Nb-electrode overlaps with the QAHI film for 5 μm. The CMEMs and CAESs are expected to have self-averaged or equilibrated to the SC potential giving no contribution to the downstream potential. This is confirmed by the width dependence of R_D for which the negative resistance decrease with increasing width and disappear for $W_\mathrm{Nb} > 365$ nm. Such a small increase in the width has almost no impact on the perimeter (~10 μm). Hence, the width dependence of the negative resistance does not agree with the expectations for the CMEMs and CAESs processes. The nonlocal CAR process, however, is exponentially suppressed with increasing W_Nb in our devices, in agreement with Ref. [20] (Fig. 1.14f).

We find that the CAR process disappears with a characteristic length of ∼100 nm, which is much larger than the superconducting coherence length of Nb in the dirty limit (∼30 nm). This indicates that it is the proximitized SC which is facilitating the CAR across the narrow superconducting electrode. This is the second important finding of this work, i.e. the V-doped $(Bi_xSb_{1-x})_2Te_3$ thin film underneath the Nb is proximitized. This means that these heterostructures are a prime candidate to search for CMEMs, which should be present if the electron doping from the Nb is not large enough to move the chemical potential into the 3D bulk bands. If the chemical potential remains in the 3D bulk band gap and the 2D surface states are the only bulk states present, then Eqs. 1.10-1.18 should hold, predicting CMEMs.

In addition, quantum transport simulations using the KWANT package are presented in this work. For wider superconducting electrodes, the KWANT simulations show Majorana interference as a result of path length differences of the two CMEMs encircling the SC. At the same time, for narrow superconducting electrodes, either CAR or CT dominates in the KWANT simulations resulting in a negative or positive downstream resistance, respectively. There was no width dependence observed in the KWANT simulation in contrast to the experimental observation of stable dominance of CAR over CT in our devices. This indicates the presence of additional physics that are not included in the simulations at the moment.

nature physics

Article

https://doi.org/10.1038/s41567-024-02574-1

Induced superconducting correlations in a quantum anomalous Hall insulator

Received: 9 July 2023

Accepted: 31 May 2024

Published online: 10 July 2024

Check for updates

Anjana Uday[1,5], Gertjan Lippertz[1,2,5], Kristof Moors[3], Henry F. Legg[4], Rikkie Joris[2], Andrea Bliesener[1], Lino M. C. Pereira[2], A. A. Taskin[1] & Yoichi Ando[1]

Thin films of ferromagnetic topological insulator materials can host the quantum anomalous Hall effect without the need for an external magnetic field. Inducing Cooper pairing in such a material is a promising way to realize topological superconductivity with the associated chiral Majorana edge states. However, finding evidence of the superconducting proximity effect in such a state has remained a considerable challenge due to inherent experimental difficulties. Here we demonstrate crossed Andreev reflection across a narrow superconducting Nb electrode that is in contact with the chiral edge state of a quantum anomalous Hall insulator. In the crossed Andreev reflection process, an electron injected from one terminal is reflected out as a hole at the other terminal to form a Cooper pair in the superconductor. This is a compelling signature of induced superconducting pair correlation in the chiral edge state. The characteristic length of the crossed Andreev reflection process is found to be much longer than the superconducting coherence length in Nb, which suggests that the crossed Andreev reflection is, indeed, mediated by superconductivity induced on the quantum anomalous Hall insulator surface. Our results will invite future studies of topological superconductivity and Majorana physics, as well as for the search for non-abelian zero modes.

Inducing superconducting (SC) correlations using the SC proximity effect in the one-dimensional (1D) edge state of a two-dimensional (2D) topological system would lead to exotic topological superconductivity hosting non-abelian anyons[1–7] and, hence, has been experimentally pursued in a couple of systems. For the 1D helical edge state of a 2D topological insulator (TI), the induced SC correlations have been detected in Josephson junctions[8,9]. The SC correlations in the quantum Hall edge states are less trivial due to the chiral nature of the edge and large magnetic fields required, but strong evidence has been obtained in terms of the crossed Andreev reflection (CAR)[10–13] or the formation of Andreev edge states[14–16], which cause a negative nonlocal potential in the downstream edge[17–20]. In the CAR process, an electron in the chiral edge entering a grounded SC electrode creates a Cooper pair by taking another electron from the other side of the electrode, causing a hole to exit into the downstream edge (Fig. 1b). This hole is responsible for the negative nonlocal voltage observed experimentally[17,20]. Importantly, SC correlations are induced in the chiral edge state through the CAR process. Very recently, the CAR process has been observed even in the fractional quantum Hall edge states[20], which are an interesting platform for creating parafermions obeying rich non-abelian statistics[21,22].

In this context, the SC proximity effect in a quantum anomalous Hall insulator (QAHI), which is a ferromagnetic TI showing the quantum anomalous Hall effect (QAHE), is highly interesting. If the 1D edge state of a QAHI can be proximitized, one could create a non-abelian

[1]Physics Institute II, University of Cologne, Cologne, Germany. [2]Quantum Solid State Physics, KU Leuven, Leuven, Belgium. [3]Peter Grünberg Institute (PGI-9), Forschungszentrum Jülich & JARA-Fundamentals of Future Information Technology, Jülich-Aachen Research Alliance, Jülich, Germany. [4]Department of Physics, University of Basel, Basel, Switzerland. [5]These authors contributed equally: Anjana Uday, Gertjan Lippertz. e-mail: taskin@ph2.uni-koeln.de; ando@ph2.uni-koeln.de

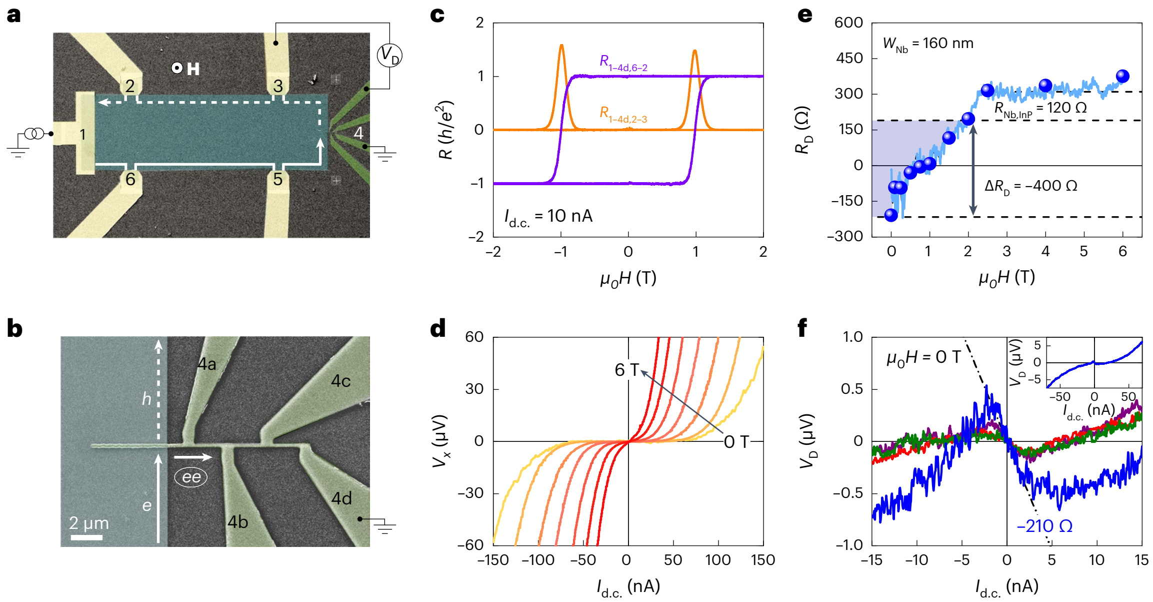

Fig. 1 | CAR across the quantum anomalous Hall edge state. a, False-colour scanning electron microscopy image of device A including the measurement schematics. The SC Nb electrode (green) and the Ti/Au normal electrodes (yellow) are in contact with the V-doped $(Bi_xSb_{1-x})_2Te_3$ thin film (cyan). For an upward, out-of-plane magnetization ($M > 0$), the chiral 1D edge state propagates anticlockwise along the sample edge. The voltage V_D between contacts 3 and 4 gives the downstream resistance $R_D \equiv V_D/I_{d.c.}$. **b**, Magnified image of the 160-nm-wide Nb electrode shown in **a**. The white arrows schematically show the CAR process. **c**, Magnetic-field dependence of the four-terminal resistances, showing the QAHE with vanishing longitudinal resistance $R_{1-4d,2-3} = 0$ and quantized transverse resistances $R_{1-4d,6-2} = h/e^2$ at 25 mK. **d**, Current versus voltage (I–V) characteristics of the four-terminal longitudinal voltage V_x at 17 mK in various applied magnetic fields H from 0 to 6 T in steps of 1 T. The breakdown current decreases with increasing H. **e**, The light blue line shows the downstream resistance R_D continuously measured as a function of H from 0 to 6 T with $I_{d.c.}$ = 2 nA at 25 mK. Blue symbols represent the slopes of the I–V characteristics at $I_{d.c.}$ = 0 at discrete magnetic fields (Supplementary Note 3), which give confidence in the negative R_D indicative of CAR. As the superconductivity in Nb is suppressed with increasing H, R_D increases by 520 Ω, which consists of the normal-state Nb resistance (120 Ω, marked by a dashed line) and the CAR contribution $\Delta R_D \simeq -400$ Ω (marked by blue shading). The R_D level of ~180 Ω marked by the middle horizontal dashed line corresponds to $R_{contact}$, which gives a positive offset to the raw R_D. **f**, I–V curves for the downstream voltage V_D measured in 0 T at 17 mK for different magnetic-field-sweep histories. The magnitude of the negative slope at $I_{d.c.}$ = 0 depends on the history. See Supplementary Note 4 for details. Inset, An I–V curve up to ±70 nA dominated by the current-induced breakdown of the QAHE.

Majorana zero mode by coupling two counter-propagating edges by the CAR process through a superconductor[6,10,17]. If, on the other hand, the 2D surface of the QAHI is proximitized, a chiral Majorana edge state may occur[2,23], which could be a platform for flying topological qubits that transfer information between stationary qubits[24–27]. Hence, proximitized QAHI is an interesting platform for Majorana physics. However, no clear evidence has been reported for the SC proximity effect in a QAHI[28–30].

The QAHI can be realized by doping Cr or V into a very thin film (typically ≲10 nm thickness) of the three-dimensional TI material $(Bi_xSb_{1-x})_2Te_3$ in which the chemical potential is fine-tuned into a magnetic gap that opens at the Dirac point of the surface states as a result of a ferromagnetic order[31–33]. Hence, a QAHI is insulating, not only in the three-dimensional bulk but also in the 2D surface. Inducing SC correlations in bulk-insulating TIs is much more difficult than in bulk-conducting TIs[34], and this is one of the reasons for the lack of clear evidence for the SC proximity effect in a QAHI. In fact, a recent work reported the observation of Andreev reflection in a metallic regime of a magnetic TI film, but when the sample was in the QAHI regime, there was no evidence for any Andreev process[28]. Another work in this context[29] used a device structure that was not optimal for detecting the relevant Andreev process. Recent experiments on quantum Hall systems found a robust signature of CAR even at the spin-polarized $\nu = 1$ filling factor[17,20], which appears to resemble a QAHI edge. However, an important difference is that a QAHI edge is not fully spin polarized[35]. In the present work, we have successfully observed the signature of CAR with a narrow Nb finger electrode (down to 160 nm width) in contact with the QAHI edge. The finger-width dependence of the CAR signal gives the characteristic length of the CAR process that is much longer than the SC coherence length of Nb, which suggests that it is not the superconductivity in the Nb electrode but the proximity-induced pairing in the QAHI beneath the Nb that is mediating the CAR process.

Nonlocal detection of CAR

Our samples are Hall-bar devices of V-doped $(Bi_xSb_{1-x})_2Te_3$ (ref. 36) in contact with SC Nb electrodes with widths ranging from 160 to 520 nm. Figure 1a,b shows false-colour scanning electron microscopy images of device A, which had the narrowest Nb electrode (contact 4). All other contacts were made of Ti/Au with contact resistances of a few ohms (Supplementary Note 1). The 1D chiral edge state propagates in the anticlockwise direction for an upward, out-of-plane magnetization ($M > 0$). For the configuration shown in Fig. 1a, we set a d.c. current to flow between contacts 1 and 4d; namely, a voltage was applied to the normal metal contact 1 and the SC contact was grounded.

In ref. 28, Andreev reflections of the electrons in the 2D 'bulk' states of a magnetic TI film in the metallic regime were observed in devices like the one in Fig. 1a, but here we probe the SC correlations in the 1D chiral edge state of the QAHI. For our purpose, confirmation of the dissipationless edge transport without the contribution of the 2D bulk is essential. In fact, the longitudinal resistance R_{xx} (= $R_{1-4d,2-3}$ measured between contacts 2 and 3 with the current between 1 and 4d) vanishes in our devices, whereas the transverse resistance R_{yx} (= $R_{1-4d,6-2}$ measured between contacts 6 and 2) is quantized to h/e^2, where h is the Planck's constant and e is the elementary charge, without the need for electrostatic gating, as shown in Fig. 1c. Note that a breakdown of the zero-resistance state occurs when the current exceeds a critical current[36–42], and the zero-resistance region is observed to shrink with increasing magnetic field, as shown in Fig. 1d, which is possibly caused by a charge redistribution between the bulk and the QAHI edge in applied magnetic fields[43,44]. This fragility of the QAHI state against current makes it difficult to estimate the contact transparency using current biasing[17,28].

The CAR process converts an incoming electron with an energy eV that is smaller than the SC gap Δ into a hole carrying a potential of $-V$ in the downstream edge (Fig. 1b), which is detected at contact 3 as the downstream voltage V_D with respect to the grounded SC contact 4a. Here, downstream refers to the chiral direction of the edge state (Fig. 1a,b). In addition, there is a finite probability that an upstream electron will tunnel directly into the downstream as an electron carrying a positive potential V. This is called co-tunnelling (CT), and it competes with the CAR process in the nonlocal transport[11–13]. The downstream resistance $R_D \equiv V_D/I_{d.c.}$ observed in this configuration consists of

$$R_D = R_{QAHI} + R_{Nb,InP} + R_{contact} + R_D^i, \qquad (1)$$

where the resistance of the QAHI film R_{QAHI} is zero for low probe currents below the breakdown, $R_{Nb,InP}$ is the resistance of the Nb section lying on the InP wafer between the film edge and the SC contact 4a (which is zero when the Nb is SC), $R_{contact}$ is the extrinsic contact resistance due to the imperfect Nb–QAHI interface and R_D^i is the intrinsic downstream resistance reflecting the CAR/CT contribution. The subgap states in the SC due to, for example, vortices can provide a dissipative channel that dumps electrons to the ground, which will reduce R_D^i (refs. 17–19). Note that the present set-up is a three-terminal configuration and that $R_{contact}$ always gives a finite contribution to V_D. An external magnetic field is not required for the realization of the QAHE, enabling us to examine R_D^i as a function of the applied magnetic field from 0 T up to the upper critical field H_{c2} of SC Nb. This is an important difference from previous studies of the SC proximity effect in quantum Hall edge states[17–20]. The magnetization measurements of our QAHI films found that the magnetic induction produced by the ferromagnetism of the film was only ~4 mT in a near-zero applied magnetic field at 2 K (Supplementary Note 13). This is smaller than the lower critical field of Nb (~180 mT)[45] and would not create vortices, which harbour subgap states and allow incident electrons to be dissipated without the Andreev mechanism[17,46,47]. However, one cannot exclude the possibility that some vortices remain trapped at strong pinning centres. Due to the chiral nature of the edge state, no Andreev reflection occurs into the upstream edge.

Figure 1e shows the magnetic-field dependence of R_D for device A with a Nb electrode of width W_{Nb} = 160 nm, measured with current $I_{d.c.}$ = 2 nA (see Supplementary Notes 3 and 4 for additional data). Below ~1 T, the downstream resistance is negative, signalling the CAR process across the Nb electrode. This is the main result of this work and demonstrates that SC correlations are induced in the chiral edge state across the SC finger by CAR processes in our devices. As the magnetic field is increased, R_D gradually turns positive and saturates as the superconductivity is lost in the Nb electrode. The change in the nonlocal downstream resistance due to the suppression of the CAR/CT process is calculated as $\Delta R_D \equiv -[R_D(H > H_{c2}) - R_D(H < H_{c2}) - R_{Nb,InP}]$, which should be equal to R_D^i provided that R_{QAHI} remains zero and $R_{contact}$ does not change across H_{c2} (which we confirmed in wide-finger devices; see Supplementary Note 14). When ΔR_D is negative (positive), the CAR (CT) process is dominant. We estimate $\Delta R_D \approx -400\ \Omega$ after subtracting the contribution of the normal-state Nb resistance $R_{Nb,InP} \approx 120\ \Omega$ (Fig. 1e and Supplementary Note 2). As $R_D^i = 0$ in the normal state, $R_D = R_{Nb,InP} + R_{contact}$ holds at $H > H_{c2}$ and below the breakdown current, allowing us to evaluate $R_{contact}$ and conclude that the CAR process contributes $\Delta R_D (= R_D^i) \approx -400\ \Omega$, which is much larger than the measured negative R_D. This ΔR_D corresponds to about 3% of the maximum negative downstream resistance $-h/2e^2$ expected for 100% CAR (Supplementary Note 8).

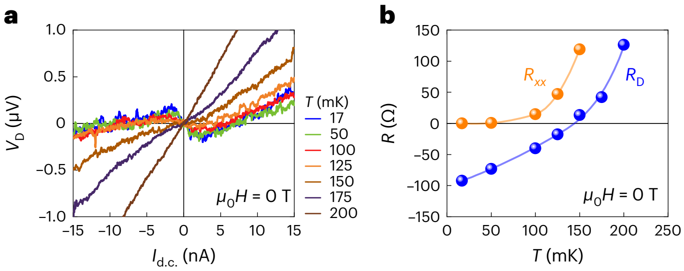

Fig. 2 | Temperature dependence of the downstream potential in device A. **a**, Plots of V_D versus $I_{d.c.}$ at different temperatures measured with the set-up shown in Fig. 1a. **b**, Temperature dependencies of R_D, extracted from the I–V curves in **a** at $I_{d.c.}$ = 0 (blue), and the four-terminal longitudinal resistance R_{xx} (orange). Above 50 mK, R_{xx} deviates from zero, indicating that the dissipationless transport of the QAHE is lost. Consequently, the 2D bulk resistance eventually dominants R_D at $T \gtrsim 100$ mK.

To give confidence that the negative R_D is not just a result of voltage fluctuations, the I–V characteristics for the downstream voltage V_D in 0 T are shown in Fig. 1f. The slope in the zero-current limit (which also gives R_D) is reproducibly negative for all the measured curves for different magnetic histories, even though the magnitude of R_D changes with the magnetic history (Supplementary Note 5), which was probably caused by a change in the disorder profile. The small nonreciprocity seen in Fig. 1f is due to 1D chiral edge transport itself[48,49]. At high current, the breakdown of the QAHE (causing $R_{QAHI} > 0$) dominates the downstream voltage (Fig. 1f, inset). The change in the behaviour of V_D versus $I_{d.c.}$ with increasing temperature is shown in Fig. 2a. The R_D values extracted from these data are plotted in Fig. 2b as a function of temperature along with the four-terminal longitudinal resistance R_{xx}, which starts to deviate from zero above ~50 mK, behaviour typical of the QAHI samples available today[36–40]. Obviously, the CAR contribution in R_D is masked by the contribution of R_{QAHI} at $T > 50$ mK. This observation demonstrates a clear link between the negative R_D and the QAHI edge transport.

Finger-width dependences of the downstream resistance

We further investigated R_D for devices with different Nb finger widths up to 520 nm. The magnetic-field dependence of R_D in device B with W_{Nb} = 235 nm is shown in Fig. 3a (see Supplementary Note 7 for data on devices C–E, which had wider fingers). The estimated Nb finger resistance $R_{Nb,InP}$ is also shown for comparison. Notice that the increase in R_D coincided with the suppression of the superconductivity in Nb. The R_D value fluctuated around zero in this W_{Nb} = 235 nm sample when the Nb was SC, which indicates that the negative CAR contribution (R_D^i) happened to be nearly of the same magnitude as $R_{contact}$, so that the resulting R_D was around zero. Note that simple Andreev reflection can account for only a factor of 2 reduction in the interface resistance[28,50] and cannot explain why R_D went to zero. We estimated $\Delta R_D = -70\ \Omega$ for device B (Fig. 3a). In addition, we confirmed that $R_U - R_D = h/e^2$, where R_U is the upstream resistance, which must hold if ΔR_D is due to Andreev processes whose contribution should cancel in $R_U - R_D$ (Supplementary Notes 8 and 12). Note that not only was $R_D < 0$ observed for device A but also that $R_D = 0$ was observed for devices B (Fig. 3a) and C (W_{Nb} = 365 nm; Supplementary Fig. 7a), which cannot be understood without CAR. Hence, the existence of CAR for W_{Nb} up to 365 nm can be inferred from the raw R_D data without analysis.

For comparison, we show in Fig. 3c the data for a W_{Nb} = 160 nm sample (device F), which was fabricated several months after the film was grown. The ageing of the film caused a large $R_{contact}$, and the CAR contribution $\Delta R_D (= R_D^i)$ could not make R_D become negative or zero, even though the width of this sample was the same as that of device A. Using the estimated $R_{Nb,InP} \simeq 100\ \Omega$, we obtained $R_{contact} \simeq 420\ \Omega$ and

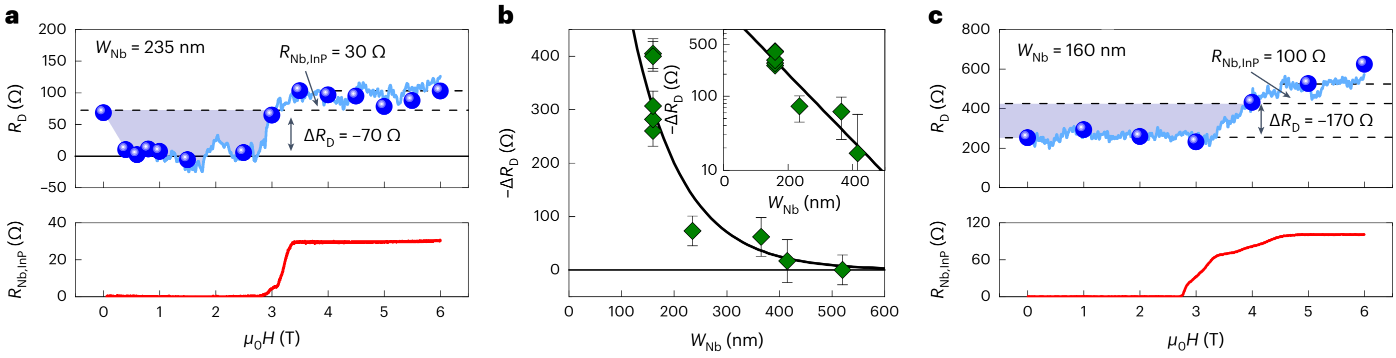

Fig. 3 | Dependencies of CAR on the width and interface quality. a, Magnetic-field dependence of R_D for the 235-nm-wide Nb electrode of device B shown together with $R_{Nb,InP}$. The light blue line shows the R_D continuously measured in a magnetic-field sweep at 25 mK with $I_{d.c.}$ = 2 nA. Blue symbols represent the slopes of the *I*–*V* curves at $I_{d.c.}$ = 0. The R_D level without $R_{Nb,InP}$ is marked by a dashed line. The change in the downstream resistance due to CAR, ΔR_D, is estimated to be about −70 Ω in this sample. **b**, Exponential width dependence of ΔR_D. Green symbols correspond to the data for devices A–E fabricated on the same wafer. The calculations of ΔR_D for five different magnetic histories in device A are explained in Supplementary Note 5. The ΔR_D values for devices B–E were obtained from the data shown in **a** and in Supplementary Fig. 7. The error bars are not due to statistics but represent uncertainties discussed in Supplementary Notes 14 and 15. Inset, The same data on a semi-log plot. The solid black line is a fit of the data to $\Delta R_D = R_0 \exp(-W_{Nb}/\xi_{CAR})$, yielding $R_0 \approx -750$ Ω and $\xi_{CAR} \approx 100$ nm. **c**, Similar measurement as in **a** for the 160-nm-wide Nb electrode of device F, fabricated on a different wafer a few months after film growth. Reflecting the relatively large interface resistance between the QAHI film and the Nb electrode, the R_D of device F was ~255 Ω, even when the Nb was SC, and it increased to ~525 Ω above H_{c2}. Nevertheless, $\Delta R_D \simeq -170$ Ω was still obtained for this 160-nm-wide Nb electrode.

$\Delta R_D \simeq -170$ Ω for this device F, pointing to the robustness of the CAR process even for a poor contact. Note that devices A–E were of higher quality because they were fabricated on a fresh QAHI film immediately after the growth.

As summarized in Fig. 3b, a finite negative ΔR_D was obtained up to $W_{Nb} \simeq 500$ nm. For device A (W_{Nb} = 160 nm), as already mentioned, different values of the negative $R_D(H < H_{c2})$ were obtained for different magnetic-field sweeps due to the changing disorder profiles. These are included in Fig. 3b as individual data points (see Supplementary Note 5 for the calculations of the ΔR_D values). One can see in the inset of Fig. 3b that, on average, the magnitude of ΔR_D was exponentially suppressed with increasing W_{Nb}. A fit to $\Delta R_D = R_0 \exp(-W_{Nb}/\xi_{CAR})$ gives $R_0 \approx -750$ Ω and the characteristic length of the CAR process $\xi_{CAR} \approx 100$ nm. This is much longer than the SC coherence length of dirty Nb, that is $\sqrt{\xi_{BCS} l_{mfp}} \approx 30$ nm, with the BCS coherence length $\xi_{BCS} = \hbar v_F^S/\pi\Delta$, Fermi velocity of Nb $v_F^S = 1.37 \times 10^6$ m s^{-1}, SC gap of Nb Δ = 1.2 meV and the mean-free path $l_{mfp} \approx 3$ nm (refs. 51,52).

Discussion

We now turn to possible scenarios by which SC correlations could be introduced into the edge states through CAR processes, starting first with a scenario in which the SC finger defines a trivial SC region, such that no chiral Majorana edge state can form. The Nb finger is itself trivial and, under certain circumstances, the induced proximitized SC state in the TI surface can also be trivial[23]. Apart from the absence of full spin polarization (Supplementary Notes 9 and 10), this scenario is essentially identical to that of the $\nu = 1$ quantum Hall state that has previously been extensively discussed[11–13,17,47,53]. Note, however, that the disordered nature of the QAHI surface would cause the Andreev edge state to become diffusive and results in an equal mix of electrons and holes, such that the Andreev edge state will not contribute to R_D^i. Taking ξ_s to be the SC coherence length of the mediating superconductor, the CAR processes induce SC correlations across the SC finger and gives rise to negative R_D^i when the finger width W_{SC} is shorter than ξ_s. When $W_{SC} \gg \xi_s$, the transport along the Andreev edge state dominates over CAR.

An alternative scenario is that the proximitized TI surface realizes a topological superconducting (TSC) region that hosts a single chiral Majorana edge mode. This can happen, for instance, if the Nb slightly dopes the TI surface to make the chemical potential lie above the magnetic gap and only the top surface is proximitized[2]. In this case, for a wide finger, an incoming electron hitting the TSC region splits into two chiral Majorana modes that take opposite paths enclosing the region covered by the finger. The two chiral Majorana modes recombine on the opposite side of the TSC region as either an electron or a hole, depending, in principle, on the number of residual vortices trapped in the SC region enclosed by the path[54,55]. However, as the chiral Majorana modes have a finite spatial extent and the QAHI surface is disordered, these processes will probably self-average in our several-micrometres-long Nb finger, resulting in an equal mix of electrons and holes transmitted to the opposite side of the finger due to the chiral Majorana modes, such that $R_D^i \approx 0$. On the other hand, a narrow finger, $W_{SC} \lesssim \xi_s$, allows CAR to the opposite edge through the bulk of the proximitized TSC region and leads to $R_D^i < 0$, as in the previous scenario of trivial SC. We can visualize these qualitatively different regimes of the TSC scenario in quantum transport simulations (Fig. 4a) with a microscopic tight-binding model appropriate for a proximitized QAHI in the TSC regime (see Methods for details). Our simulation results in Fig. 4b,c show that, when the SC finger is much wider than the induced SC coherence length, the current on the top surface is carried by chiral Majorana modes travelling around the proximitized section, with the finger length and the width both affecting the interference. For example, the plot in Fig. 4b for a wide finger shows that the electron to hole conversion probability T_{eh} oscillates regularly as a function of the finger length L_{SC} when $L_{SC} \gg \xi_s$. Here, $T_{eh} > 0.5$ means that holes predominantly come out of the finger into the downstream edge due to the interference of the chiral Majorana modes. In a real situation with a long finger, such an oscillating T_{eh} would self-average to 0.5, resulting in $R_D^i \approx 0$. When the finger is narrower ($W_{SC} \approx \xi_s$), a qualitatively different regime is obtained. In that case, T_{eh} is very sensitive to L_{SC} for $L_{SC} \lesssim \xi_s$, but it stabilizes at large L_{SC} to a nearly fixed value that depends sensitively on W_{SC}. Figure 4b shows the behaviour of T_{eh} for two different widths in the narrow regime. These are stabilized at large L_{SC} to T_{eh} values larger and smaller than 0.5. The simulated local current densities (Fig. 4c) suggest that there are no more well-separated chiral Majorana modes in this regime and that the electron to hole conversion can be attributed to a CAR process that occurs mainly near the QAHI edge.

Therefore, our simulations suggest that, like the trivial SC case, the CAR process can indeed become dominant in the TSC case. We should nevertheless note that the stabilized value of T_{eh} for a narrow

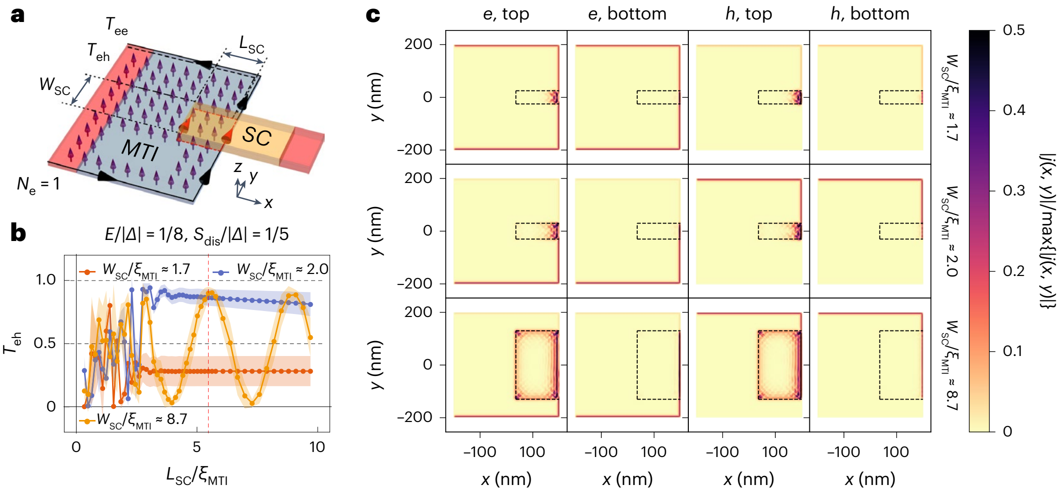

Fig. 4 | Quantum transport simulation of CAR in a proximitized QAHI thin film. **a**, Schematic of the transport simulation set-up with a magnetic TI (MTI) thin film in the QAHI state. The film is covered by a SC finger over a region with length L_{SC} and width W_{SC}. We consider that the top surface of the MTI below the SC finger has been shifted out of the magnetic gap and proximitized into the TSC regime. The leads (red) are set to be semi-infinite. **b**, The disorder-averaged electron to hole conversion probability T_{eh} (standard deviation indicated by shading) across the TSC region at a small bias energy E is shown as a function of L_{SC} for three selected values of W_{SC}. **c**, The components of local current densities carried by electrons and holes as well as at the top and bottom surfaces, plotted for the three different widths of the SC finger (indicated by black dashed lines) used in **b**. The finger length under consideration, indicated by the vertical red dashed line in **b**, yields $T_{eh} > 0.5$ for two out of three examples, corresponding to a regime dominated by CAR for a narrow finger and by the chiral Majorana edge-channel interference for a wide finger.

finger at large L_{SC} is strongly dependent on W_{SC} in our simulation and is not always larger than 0.5 (Supplementary Note 11), which implies that R^i_D would fluctuate between negative and positive values as a function of W_{SC} in the narrow finger regime. Similar oscillatory behaviour has also been predicted by theoretical calculations for the trivial SC case[11–13]. However, in our experiment, we found ΔR_D (= R^i_D) to be always negative for narrow fingers, as was also the case with similar experiments on graphene with a trivial SC finger[17,20]. This stability of negative R^i_D points to the existence of additional physics that are not captured in our simulations. In fact, the reason for the stable dominance of CAR in real experiments is an interesting subject in its own right[13,47,53]. For example, the dissipative channel through vortices in the SC finger, which is not included in our simulations, could be playing a role[19,47]. In this regard, in related experiments to probe the Andreev edge states with a wide SC electrode, oscillatory R^i_D and stably negative R^i_D were both reported[18,19]. The latter is surprising[56], and possible explanations for the dominance of electron to hole conversion in the Andreev edge states have also been proposed[19,46,57,58]. Our result extends the case of the stable dominance of electron to hole conversion and calls for a better theoretical understanding.

One can see from the above considerations that both trivial and non-trivial scenarios are consistent with our observations. Irrespective of its nature, our observation $\xi_{CAR} \gg \xi_{Nb}$ implies that CAR occurs through the superconductivity of the proximitized magnetic TI surface, rather than the SC finger itself. This makes sense, since Nb has negligible spin–orbit coupling and the finger on the top surface does not naturally result in processes coupling to the bottom surface, whereas our simulations suggest that the bottom surface needs to be involved in the CAR processes in the QAHI platform. Furthermore, the dependence on the magnetic history of the device suggests that trapped vortices or the magnetic disorder profile play a role, which is natural in the above scenario for CAR through the proximitized surface. If ξ_{CAR} is taken as the SC coherence length in the QAHI surface, a simple estimate gives the induced SC gap $\Delta_{ind} \approx 0.04$ meV (Supplementary Note 16).

An obvious next step is to confirm whether the induced 2D superconductivity is topological and is associated with chiral Majorana edge states. A possible experiment to address this question would be based on a device like ours but with a much shorter finger electrode, such that the interference between the two chiral Majorana edge states travelling along either sides of the finger can be detected without self-averaging. A transmitted charge switching between an electron and a hole depending on the number of vortices in the finger would give strong evidence for chiral Majoranas[54,55]. Furthermore, by putting two SC fingers close enough together to make a Josephson junction and by applying a voltage pulse across the junction, one could inject an edge vortex in the chiral Majorana edge state. This edge vortex is a non-abelian zero mode and experiments to confirm its non-abelian nature have been theoretically proposed[24]. Therefore, the platform presented here offers ample opportunities to address topological superconductivity, Majorana physics and non-abelian zero modes.

Online content

Any methods, additional references, Nature Portfolio reporting summaries, source data, extended data, supplementary information, acknowledgements, peer review information; details of author contributions and competing interests; and statements of data and code availability are available at https://doi.org/10.1038/s41567-024-02574-1.

References

1. Fu, L. & Kane, C. L. Josephson current and noise at a superconductor/quantum-spin-Hall-insulator/superconductor junction. *Phys. Rev. B* **79**, 161408 (2009).
2. Qi, X.-L., Hughes, T. L. & Zhang, S.-C. Chiral topological superconductor from the quantum Hall state. *Phys. Rev. B* **82**, 184516 (2010).
3. Lindner, N. H., Berg, E., Refael, G. & Stern, A. Fractionalizing Majorana fermions: non-abelian statistics on the edges of abelian quantum Hall states. *Phys. Rev. X* **2**, 041002 (2012).
4. Cheng, M. Superconducting proximity effect on the edge of fractional topological insulators. *Phys. Rev. B* **86**, 195126 (2012).
5. Clarke, D. J., Alicea, J. & Shtengel, K. Exotic non-abelian anyons from conventional fractional quantum Hall states. *Nat. Commun.* **4**, 1348 (2013).
6. Vaezi, A. Fractional topological superconductor with fractionalized Majorana fermions. *Phys. Rev. B* **87**, 035132 (2013).

7. Vaezi, A. Superconducting analogue of the parafermion fractional quantum Hall states. *Phys. Rev. X* **4**, 031009 (2014).
8. Hart, S. et al. Induced superconductivity in the quantum spin Hall edge. *Nat. Phys.* **10**, 638–643 (2014).
9. Wiedenmann, J. et al. 4π-periodic Josephson supercurrent in HgTe-based topological Josephson junctions. *Nat. Commun.* **7**, 10303 (2016).
10. Clarke, D. J., Alicea, J. & Shtengel, K. Exotic circuit elements from zero-modes in hybrid superconductor–quantum-Hall systems. *Nat. Phys.* **10**, 877–882 (2014).
11. Hou, Z., Xing, Y., Guo, A.-M. & Sun, Q.-F. Crossed Andreev effects in two-dimensional quantum Hall systems. *Phys. Rev. B* **94**, 064516 (2016).
12. Beconcini, M., Polini, M. & Taddei, F. Nonlocal superconducting correlations in graphene in the quantum Hall regime. *Phys. Rev. B* **97**, 201403 (2018).
13. Galambos, T. H., Ronetti, F., Hetényi, B., Loss, D. & Klinovaja, J. Crossed Andreev reflection in spin-polarized chiral edge states due to the Meissner effect. *Phys. Rev. B* **106**, 075410 (2022).
14. Hoppe, H., Zülicke, U. & Schön, G. Andreev reflection in strong magnetic fields. *Phys. Rev. Lett.* **84**, 1804–1807 (2000).
15. Chtchelkatchev, N. M. & Burmistrov, I. S. Conductance oscillations with magnetic field of a two-dimensional electron gas–superconductor junction. *Phys. Rev. B* **75**, 214510 (2007).
16. Khaymovich, I. M., Chtchelkatchev, N. M., Shereshevskii, I. A. & Mel'nikov, A. S. Andreev transport in two-dimensional normal-superconducting systems in strong magnetic fields. *Europhys. Lett.* **91**, 17005 (2010).
17. Lee, G.-H. et al. Inducing superconducting correlation in quantum Hall edge states. *Nat. Phys.* **13**, 693–698 (2017).
18. Zhao, L. et al. Interference of chiral Andreev edge states. *Nat. Phys.* **13**, 862–867 (2020).
19. Hatefipour, M. et al. Induced superconducting pairing in integer quantum Hall edge states. *Nano Lett.* **22**, 6173–6178 (2022).
20. Gül, O. et al. Andreev reflection in the fractional quantum Hall state. *Phys. Rev. X* **12**, 021057 (2022).
21. Mong, R. S. K. et al. Universal topological quantum computation from a superconductor-abelian quantum Hall heterostructure. *Phys. Rev. X* **4**, 011036 (2014).
22. Alicea, J. & Fendley, P. Topological phases with parafermions: theory and blueprints. *Annu. Rev. Condens. Matter Phys.* **7**, 119–139 (2016).
23. Wang, J., Zhou, Q., Lian, B. & Zhang, S.-C. Chiral topological superconductor and half-integer conductance plateau from quantum anomalous Hall plateau transition. *Phys. Rev. B* **92**, 064520 (2015).
24. Beenakker, C. W. J. et al. Deterministic creation and braiding of chiral edge vortices. *Phys. Rev. Lett.* **122**, 146803 (2019).
25. Beenakker, C. J., Grabsch, A. & Herasymenko, Y. Electrical detection of the Majorana fusion rule for chiral edge vortices in a topological superconductor. *SciPost Phys.* **6**, 022 (2019).
26. Adagideli, I., Hassler, F., Grabsch, A., Pacholski, M. & Beenakker, C. W. J. Time-resolved electrical detection of chiral edge vortex braiding. *SciPost Phys.* **8**, 013 (2020).
27. Bauerle, C. et al. Coherent control of single electrons: a review of current progress. *Rep. Prog. Phys.* **81**, 056503 (2018).
28. Kayyalha, M. et al. Absence of evidence for chiral Majorana modes in quantum anomalous Hall-superconductor devices. *Science* **367**, 64–67 (2020).
29. Shen, J. et al. Spectroscopic fingerprint of chiral Majorana modes at the edge of a quantum anomalous Hall insulator/superconductor heterostructure. *Proc. Natl Acad. Sci. USA* **117**, 238–242 (2020).
30. Thorp, H. H. Editorial retraction. *Science* **378**, 718 (2022).
31. Yu, R. et al. Quantized anomalous Hall effect in magnetic topological insulators. *Science* **329**, 61–64 (2010).
32. Chang, C.-Z. et al. Experimental observation of the quantum anomalous Hall effect in a magnetic topological insulator. *Science* **340**, 167–170 (2013).
33. Chang, C.-Z. et al. High-precision realization of robust quantum anomalous Hall state in a hard ferromagnetic topological insulator. *Nat. Mater.* **14**, 473–477 (2015).
34. Ghatak, S. et al. Anomalous Fraunhofer patterns in gated Josephson junctions based on the bulk-insulating topological insulator $BiSbTeSe_2$. *Nano Lett.* **18**, 5124–5131 (2018).
35. Zhang, R.-X., Hsu, H.-C. & Liu, C.-X. Electrically tunable spin polarization of chiral edge modes in a quantum anomalous Hall insulator. *Phys. Rev. B* **93**, 235315 (2016).
36. Lippertz, G. et al. Current-induced breakdown of the quantum anomalous Hall effect. *Phys. Rev. B* **106**, 045419 (2022).
37. Kawamura, M. et al. Current-driven instability of the quantum anomalous Hall effect in ferromagnetic topological insulators. *Phys. Rev. Lett.* **119**, 016803 (2017).
38. Fox, E. J. et al. Part-per-million quantization and current-induced breakdown of the quantum anomalous Hall effect. *Phys. Rev. B* **98**, 075145 (2018).
39. Rodenbach, L. K. et al. Bulk dissipation in the quantum anomalous Hall effect. *APL Mater.* **9**, 081116 (2021).
40. Fijalkowski, K. M. et al. Quantum anomalous Hall edge channels survive up to the Curie temperature. *Nat. Commun.* **12**, 5599 (2021).
41. Qiu, G. et al. Mesoscopic transport of quantum anomalous Hall effect in the submicron size regime. *Phys. Rev. Lett.* **128**, 217704 (2022).
42. Zhou, L.-J. et al. Confinement-induced chiral edge channel interaction in quantum anomalous Hall insulators. *Phys. Rev. Lett.* **130**, 086201 (2023).
43. Böttcher, J., Tutschku, C., Molenkamp, L. W. & Hankiewicz, E. M. Survival of the quantum anomalous Hall effect in orbital magnetic fields as a consequence of the parity anomaly. *Phys. Rev. Lett.* **123**, 226602 (2019).
44. Böttcher, J., Tutschku, C. & Hankiewicz, E. M. Fate of quantum anomalous Hall effect in the presence of external magnetic fields and particle-hole asymmetry. *Phys. Rev. B* **101**, 195433 (2020).
45. Saito, K. Critical field limitation of the niobium superconducting RF cavity. In *Proc. 10th Workshop on RF Superconductivity.* 583–587 (High Energy Accelerator Research Organization, 2001).
46. Tang, Y., Knapp, C. & Alicea, J. Vortex-enabled Andreev processes in quantum Hall–superconductor hybrids. *Phys. Rev. B* **106**, 245411 (2022).
47. Schiller, N. et al. Superconductivity and fermionic dissipation in quantum Hall edges. *Phys. Rev. B* **107**, L161105 (2023).
48. Yasuda, K. et al. Large non-reciprocal charge transport mediated by quantum anomalous Hall edge states. *Nat. Nanotechnol.* **15**, 831–835 (2020).
49. Baumgartner, C. et al. Supercurrent rectification and magnetochiral effects in symmetric Josephson junctions. *Nat. Nanotechnol.* **17**, 39–44 (2022).
50. Blonder, G. E., Tinkham, M. & Klapwijk, T. M. Transition from metallic to tunneling regimes in superconducting microconstrictions: excess current, charge imbalance, and supercurrent conversion. *Phys. Rev. B* **25**, 4515–4532 (1982).
51. Ashcroft, N. W. & Mermin, N. D. *Solid State Physics* (Saunders Collage Publishing, 1976).
52. Zaytseva, I., Abaloszew, A., Camargo, B. C., Syryanyy, Y. & Cieplak, M. Z. Upper critical field and superconductor-metal transition in ultrathin niobium films. *Sci. Rep.* **10**, 19062 (2020).

53. Kurilovich, V. D. & Glazman, L. I. Criticality in the crossed Andreev reflection of a quantum Hall edge. *Phys. Rev. X* **13**, 031027 (2023).
54. Fu, L. & Kane, C. L. Probing neutral Majorana fermion edge modes with charge transport. *Phys. Rev. Lett.* **102**, 216403 (2009).
55. Akhmerov, A. R., Nilsson, J. & Beenakker, C. W. J. Electrically detected interferometry of Majorana fermions in a topological insulator. *Phys. Rev. Lett.* **102**, 216404 (2009).
56. Kurilovich, V. D., Raines, Z. M. & Glazman, L. I. Disorder-enabled Andreev reflection of a quantum Hall edge. *Nat. Commun.* **14**, 2237 (2023).
57. David, A., Meyer, J. S. & Houzet, M. Geometrical effects on the downstream conductance in quantum-Hall–superconductor hybrid systems. *Phys. Rev. B* **107**, 125416 (2023).
58. Michelsen, A. B., Recher, P., Braunecker, B. & Schmidt, T. L. Supercurrent-enabled Andreev reflection in a chiral quantum Hall edge state. *Phys. Rev. Res.* **5**, 013066 (2023).

Methods

Material growth and device fabrication

The V-doped $(Bi_xSb_{1-x})_2Te_3$ thin films were grown on InP (111)A substrates by molecular beam epitaxy in a ultrahigh vacuum. High-purity V, Bi, Sb and Te were co-evaporated onto the substrate, which was kept at a temperature of 190 °C to produce a uniform film of thickness ~8 nm. The chemical potential was tuned into the magnetic gap for an optimized Bi:Sb beam-equivalent-pressure ratio of 1:4. A capping layer of 4 nm Al_2O_3 was made ex situ with atomic layer deposition at 80 °C using Ultratec Savannah S200 to protect the film from degradation in air. The Hall-bar devices were patterned using standard optical lithography techniques. The narrow Nb/Au SC contacts (45 nm/5 nm) and the Ti/Au normal metal contacts (5 nm/45 nm) were defined using electron-beam lithography. The Al_2O_3 capping layer was selectively removed in heated aluminium etchant (Type-D, Transene), before the sputter-deposition of the Ti/Au and Nb/Au layers in a ultrahigh vacuum. Devices A–E reported in this paper were fabricated simultaneously on the same wafer, whereas device F was made on a separate wafer. A clean QAHE without the need for gating was observed in all devices. Scanning electron microscopy was used to determine the width of the Nb electrodes, which were covered with 5-nm-thick Au to avoid oxidation.

Measurement set-up

The transport measurements were performed at a base temperature of 17–25 mK in a dry dilution refrigerator (Triton 200, Oxford Instruments) equipped with a 8 T SC magnet. All the data presented in Main were measured using a standard d.c. technique with nanovoltmeters (2182A, Keithley) and a current source (2450, Keithley). The a.c. data shown in Supplementary Note 4 were measured using a standard a.c. lock-in technique at low frequency (3–7 Hz) using lock-in amplifiers (LI5640 and LI5645, NF Corporation). The magnetization measurements were performed using a commercial superconducting quantum interference device (SQUID) magnetometer (MPMS3, Quantum Design). The sample was mounted in a plastic straw, self-clamped, with the sample surface perpendicular to the applied magnetic field.

Quantum transport simulations

We performed the quantum transport simulations using the KWANT[59] package, by considering a 2 × 4-orbital two-dimensional tight-binding model (on a square lattice with lattice constant a = 2 nm), based on the following Bogoliubov–de Gennes model Hamiltonian for a proximitized magnetic TI (MTI) thin film[23,31,60]:

$$H_{\mathrm{BdG}}(k_x,k_y)=\begin{pmatrix} H_{\mathrm{MTI}}(k_x,k_y)-\mu & -\mathrm{i}\sigma_y(1+\rho_z)\Delta/2 \\ \mathrm{i}\sigma_y(1+\rho_z)\Delta^*/2 & \mu-H^*_{\mathrm{MTI}}(-k_x,-k_y)\end{pmatrix}, \quad (2)$$

$$H_{\mathrm{MTI}}(k_x,k_y)=\hbar v_{\mathrm{D}}(k_y\sigma_x-k_x\sigma_y)\rho_z+\left[m_0+m_1(k_x^2+k_y^2)\right]\rho_x+M_z\sigma_z, \quad (3)$$

with $\sigma_{x,y,z}$ and $\rho_{x,y,z}$ the Pauli matrices acting on the spin and pseudospin (for the top and bottom surfaces) degrees of freedom, respectively, and μ the chemical potential. We set the Dirac velocity $\hbar v_{\mathrm{D}}$ = 3 eV Å, the top–bottom surface hybridization m_0 = −5 meV and m_1 = 15 meV Å^2, out-of-plane magnetization strength M_z = 50 meV, and proximity-induced s-wave pairing potential Δ (on the top surface) with $|\Delta|$ = 10 meV (yielding an induced SC coherence length $\xi_{\mathrm{MTI}}=\hbar v_{\mathrm{D}}/|\Delta|$ = 30 nm). These model parameters yielded a magnetic gap $E_{\mathrm{gap}}=2(M_z-|m_0|)$ = 90 meV, meaning that the magnetic gap edge was 45 meV above the Dirac point. We considered the chemical potential μ = 25 meV, such that the Fermi level was nearly centred between the Dirac point and the magnetic gap edge. To obtain a TSC regime in the region below the SC finger, we introduced a local shift of $\Delta\mu$ = 75 meV to bring the local Fermi level well above the magnetic gap. Nonmagnetic (for example, electrostatic) disorder was considered by adding a Gaussian random field to the on-site energies of the TI thin film near the position of the SC finger. The disorder was characterized by the disorder strength S = 2 meV (the standard deviation of the Gaussian) and spatial correlation length λ = 10 nm. Note that the model parameters did not reflect the device properties quantitatively, as that would have required a scattering region several orders of magnitude larger than presently considered in our simulations (in particular, due to the much larger SC finger size and induced SC coherence length). Our aim was to investigate the CAR ($\xi_{\mathrm{MTI}}\approx W_{\mathrm{SC}}$) and Majorana interference ($\xi_{\mathrm{MTI}}\gg W_{\mathrm{SC}}$) regimes qualitatively.

Data availability

Raw data used in the generation of Figs. 1–4 and Supplementary Figs. 1–13 are available via Zenodo at https://doi.org/10.5281/zenodo.11231864 (ref. 61). Source data are provided with this paper.

Code availability

The code used in the quantum transport simulations is available via Zenodo at https://doi.org/10.5281/zenodo.11231864 (ref. 61) along with the raw data.

References

59. Groth, C. W., Wimmer, M., Akhmerov, A. R. & Waintal, X. Kwant: a software package for quantum transport. *New J. Phys.* **16**, 063065 (2014).
60. Chen, C.-Z., Xie, Y.-M., Liu, J., Lee, P. A. & Law, K. T. Quasi-one-dimensional quantum anomalous Hall systems as new platforms for scalable topological quantum computation. *Phys. Rev. B* **97**, 104504 (2018).
61. Uday, A. et al. Induced superconducting correlations in a quantum anomalous Hall insulator. *Zenodo* https://doi.org/10.5281/zenodo.11231864 (2023).

Acknowledgements

We thank Y. Tokura, M. Kawasaki and R. Yoshimi for their advice on the growth of QAHI films. We thank E. Bocquillon for fruitful discussions. This project has received funding from the European Research Council under the European Union's Horizon 2020 research and innovation programme (Grant Agreement No. 741121) and was also funded by the German Research Foundation under Germany's Excellence Strategy – Cluster of Excellence Matter and Light for Quantum Computing EXC 2004/1 (Project No. 390534769) and by the German Research Foundation under CRC 1238 Subprojects A04 and B01 (Project No. 277146847). G.L. acknowledges support from KU Leuven's special research fund and the Research Foundation – Flanders, Belgium (File Nos. 27531 and 52751). K.M. acknowledges support from the Bavarian Ministry of Economic Affairs, Regional Development and Energy within Bavaria's High-Tech Agenda Project 'Bausteine für das Quantencomputing auf Basis topologischer Materialien mit experimentellen und theoretischen Ansätzen' (Grant Allocation No. 07 02/686 58/1/21 1/22 2/23), the QuantERA grant MAGMA and the German Research Foundation (Grant No. 491798118). H.F.L. acknowledges support from the Georg H. Endress Foundation.

Author contributions

A.A.T. and Y.A. conceived the project. A.U., G.L, A.B. and A.A.T. grew the thin films. R.J. and L.M.C.P. performed the SQUID measurements. A.U. and G.L. fabricated the devices. A.U., G.L. and A.A.T. performed the experiments and, with the help of Y.A., analysed the data. K.M. performed the theoretical simulation. A.A.T. and Y.A. interpreted the data with the help of H.F.L. and K.M. A.U., Y.A., H.F.L. and K.M. wrote the manuscript with input from all authors.

Funding
Open access funding provided by Universität zu Köln.

Competing interests
The authors declare no competing interests.

Additional information
Supplementary information The online version contains supplementary material available at https://doi.org/10.1038/s41567-024-02574-1.

Correspondence and requests for materials should be addressed to A. A. Taskin or Yoichi Ando.

Peer review information *Nature Physics* thanks Jing Wang and the other, anonymous, reviewer(s) for their contribution to the peer review of this work.

nature physics

Supplementary information https://doi.org/10.1038/s41567-024-02574-1

Induced superconducting correlations in a quantum anomalous Hall insulator

In the format provided by the authors and unedited

Supplementary Information for "Induced superconducting correlations in a quantum anomalous Hall insulator"

Supplementary Note 1 Contact Resistance for Ti/Au contact

Figure S1a shows the schematics of the 3-terminal measurement for the contact resistance of contact 1. Figure S1b shows the voltage $V_{6\text{-}1}$ as a function of the DC current $I_{2\text{-}1}$ recorded at 17 mK in different magnetic fields. For an upward, out-of-plane magnetization, the 3-terminal (downstream) resistance $R_{2\text{-}1,6\text{-}1} \equiv V_{6\text{-}1}/I_{2\text{-}1}$ consists only of the sample resistance and the contact resistance. Before the current-induced breakdown of the QAHE, the sample resistance is zero. Hence, the slope of 3.5 Ω in the pre-breakdown regime is the contact resistance of the Ti/Au contact 1.

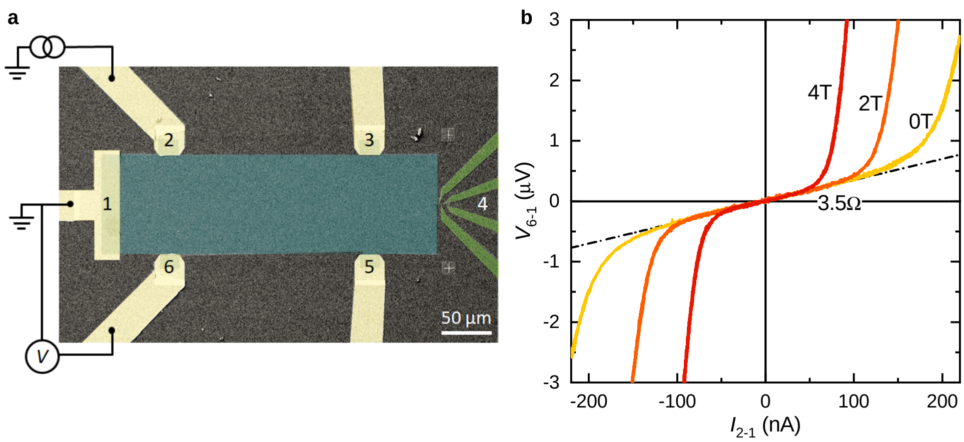

Figure S1: **Three-terminal I-V characteristics in device A for the Ti/Au contact 1. a,** False-colour scanning-electron-microscope image of device A from Fig.1a, including the measurement schematics. The current flew from contact 2 to 1, and the voltage was measured between contacts 6 and 1. For an upward, out-of-plane magnetization ($M > 0$), the chiral 1D edge state propagates in the counter-clockwise direction. **b,** Plots of the 3-terminal voltage $V_{6\text{-}1}$ as a function of the DC current $I_{2\text{-}1}$ for various magnetic field H at 17 mK. The breakdown current of the QAHE decreases with increasing H. The dashed line is a linear fit to the pre-breakdown regime, yielding the slope of ∼3.5 Ω that corresponds to the contact resistance of the Ti/Au contact 1.

Supplementary Note 2 Estimation of the normal-state Nb contribution

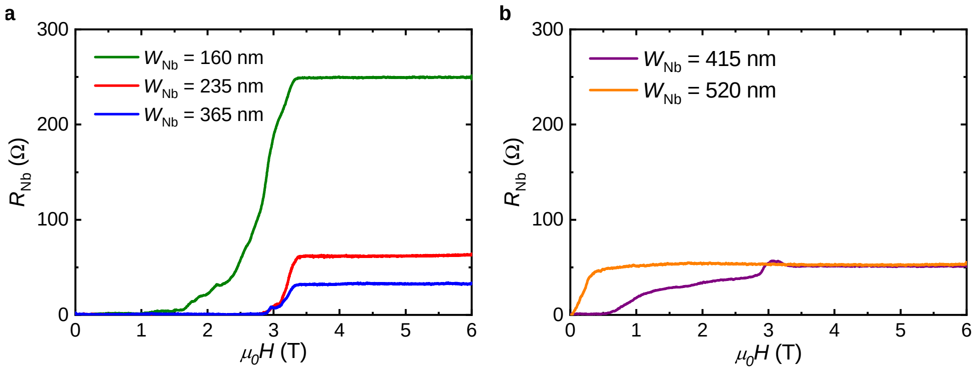

Figure S2: **Magnetic-field dependence of the Nb electrode resistance.** **a,** The 4-terminal Nb resistance R_{Nb} of device A ($W_{\text{Nb}} = 160$ nm), device B ($W_{\text{Nb}} = 235$ nm), and device C ($W_{\text{Nb}} = 365$ nm). **b,** R_{Nb} of device D ($W_{\text{Nb}} = 415$ nm) and device E ($W_{\text{Nb}} = 520$ nm). Although the Nb electrodes on all the devices were fabricated simultaneously, the resistivity of Nb and the upper critical field H_{c2} differ among the devices.

In the main text, Figs. 1a-b show SEM pictures of device A. The Nb electrode contains four contacts (4a, 4b, 4c, and 4d) to allow for a 4-terminal resistance measurement, with separations $L_{\text{Nb,sect.}} \equiv L_{\text{a-b}} = L_{\text{b-c}} = L_{\text{c-d}} = 2.5\ \mu$m. The width is $W_{\text{Nb}} = 160$ nm along the full length of the Nb electrode. The overlap with the V-doped $(\text{Bi}_x\text{Sb}_{1-x})_2\text{Te}_3$ thin film is $L_{\text{Nb,film}} = 5\ \mu$m. The small Nb section on the InP substrate between the edge of the thin film and contact 4a has a length of $L_{\text{Nb,InP}} = 1.2\ \mu$m. Devices B, C, D, and E are identical to device A except for the width of the Nb electrode: $W_{\text{Nb}} = 235$, 365, 415, and 520 nm, respectively. Figure S2 shows the 4-terminal Nb resistance R_{Nb} $(= V_{\text{4b}-\text{4c}}/I_{\text{4a}-\text{4d}})$ as a function of the applied magnetic field. While devices A–E are on the same wafer and the Nb electrodes were fabricated simultaneously, the resistivity of Nb and the upper critical field H_{c2} differ among the devices. The normal-state resistance $R_{\text{Nb,InP}}$ of the $L_{\text{Nb,InP}}$-section contributes to the downstream resistance through $R_{\text{D}} = R_{\text{QAHI}} + R_{\text{Nb,InP}} + R_{\text{contact}} + R^{\text{i}}_{\text{D}}$ as explained in the main text. To estimate $R_{\text{Nb,InP}}$ for each device, the Nb resistance is rescaled by $L_{\mathrm{Nb,InP}}/L_{\mathrm{Nb,sect.}} = 1.2\ \mu\mathrm{m} / 2.5\ \mu\mathrm{m}$. This $R_{\mathrm{Nb,InP}}$ was also used in the calculation of the data points for $\Delta R_{\mathrm{D}} = -[R_{\mathrm{D}}(H > H_{\mathrm{c2}}) - R_{\mathrm{D}}(H < H_{\mathrm{c2}}) - R_{\mathrm{Nb,InP}}]$ shown in Fig.3b.

Supplementary Note 3 *I-V* characteristics at different magnetic fields in device A

In the main text, Fig. 1e shows the magnetic-field dependence of R_{D}; the blue symbols represent the slopes at $I_{\mathrm{DC}} = 0$ extracted from the I-V curves shown in Fig. S3. Negative R_{D} is observed for $\mu_0 H < 1$ T. Moreover, notice the large noise amplitude for the V_{D}-vs-I_{DC} curves displaying negative slopes, whereas a lower noise level is observed for curves measured above the H_{c2} of Nb. This indicates that the noise is intrinsic to the CAR process in this system.

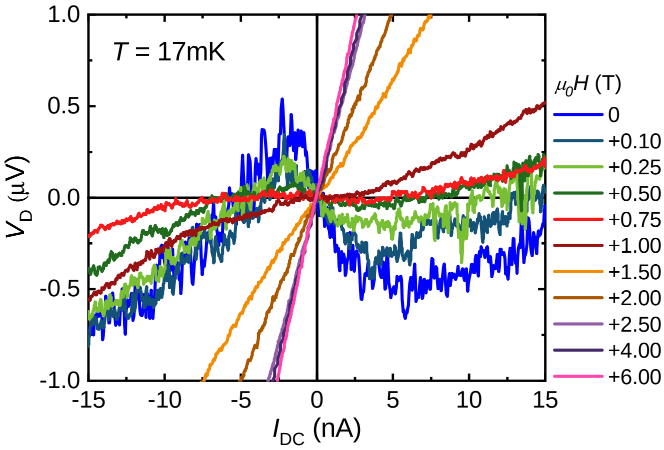

Figure S3: ***I-V* characteristics at different magnetic fields in device A.** The negative slope in the zero-current limit, confirming the negative R_{D}, is reproducibly observed below 1 T, where the Nb electrode is still superconducting.

Supplementary Note 4 Comparison of R_D measured with DC and AC techniques

The plots of V_D vs I_{DC} shown in Fig. S3 were obtained with a DC technique. Up to a DC current of $|I_{DC}| \lesssim 3$ nA, the slope of V_D (and hence R_D) is negative below 1 T. To verify the negative R_D, the sample is remeasured with an AC lock-in technique with a small AC excitation current of $I_{RMS} = 1$ nA (i.e. $I_{peak} = 1.41$ nA) for the same experimental setup as shown in Fig. 1a. Figure S4 shows that the result of the AC measurement agrees well with the slopes of the I-V curves at I_{DC} = 0 measured with the DC technique. Hence, the negative R_D in device A is reproducible between the AC and DC techniques. We note that the sharp spike in R_D near zero magnetic field seen in the AC-measurement data in Fig. S4 is an artifact most likely related to a sharp increase in the temperature upon crossing $H = 0$ due to a magnetocaloric effect, similar to observations by other research groups [1–3].

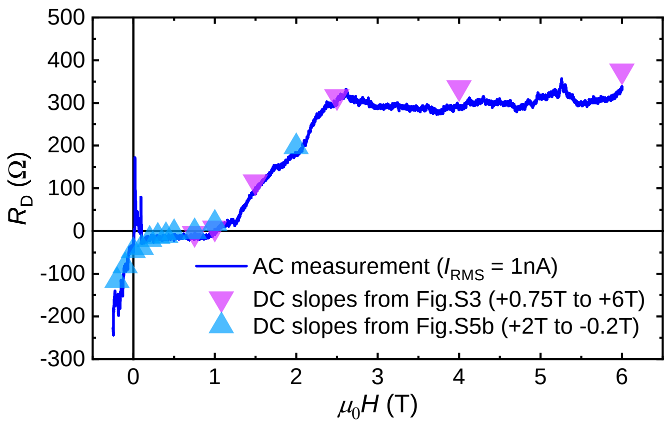

Figure S4: **Validation of the R_D values in device A.** The solid blue line shows R_D measured continuously with an AC technique with $I_{RMS} = 1$ nA at 25 mK as a function of the applied magnetic field; this R_D result is consistent with the R_D values extracted from the slopes of the I-V curves at I_{DC} = 0 measured with the DC technique (magenta and cyan symbols).

Supplementary Note 5 Effect of the magnetic-field-sweep history on R_D in device A

After taking the data shown in Fig. S3 (for which H was increased from 0 to 6 T), we reduced H back to 0 T and took the I-V data shown in Fig. S5a in the order of 0 , -0.1, and -0.25 T. Then, we increased the magnetic field to 2 T and decreased it to -0.2 T, during which we took the series of I-V curves at different magnetic fields shown in Fig. S5b. Interestingly, the R_{D} values in the zero-current limit obtained for the series shown in Fig. S5b are essentially consistent with those obtained in the series shown in Fig. S5a, see Fig. S5d. This suggests that the system has metastable disorder profiles, and it remained in the same profile between the measurements of Fig. S5a and Fig. S5b, while the profile changed from that in the measurements of Fig. S3 (i.e. Fig. 1e in the main text). The temperature dependence data shown in Fig. 2b of the main text were measured after we took the data in Fig. S5b and set the magnetic field to zero again. To check for the effect of thermal cycling, we measured the 0-T I-V curves at 17 mT before and after the sample was heated to 200 mK, and the result is shown in Fig. S5c. It appears that the thermal cycling has little effect on R_{D}.

To summarize the effect of the magnetic-field-sweep history in device A, Fig. S5d shows the R_{D} values obtained in four different magnetic-field sweeps performed to take the data shown in Figs. S3, S5a, S5b, and S5c. Altogether, the obtained negative slopes of $-210\ \Omega$ (Fig. 1f), $-215\ \Omega$ (Fig. S5a), $-117\ \Omega$ (Fig. S5b), $-92\ \Omega$ (Fig. S5c), and $-72\ \Omega$ (Fig. S5c) are used as the values of $R_{\mathrm{D}}(H < H_{\mathrm{c2}})$ for each magnetic cycle to calculate the five data points of $\Delta R_{\mathrm{D}} = -[R_{\mathrm{D}}(H > H_{\mathrm{c2}}) - R_{\mathrm{D}}(H < H_{\mathrm{c2}}) - R_{\mathrm{Nb,InP}}]$ shown in Fig. 3b of the main text for devicd A, along with $R_{\mathrm{D}}(H > H_{\mathrm{c2}}) = 310\,\Omega$ (obtained from the data in Fig. S3) and $R_{\mathrm{Nb,InP}} = 120\,\Omega$ (Fig. S2).

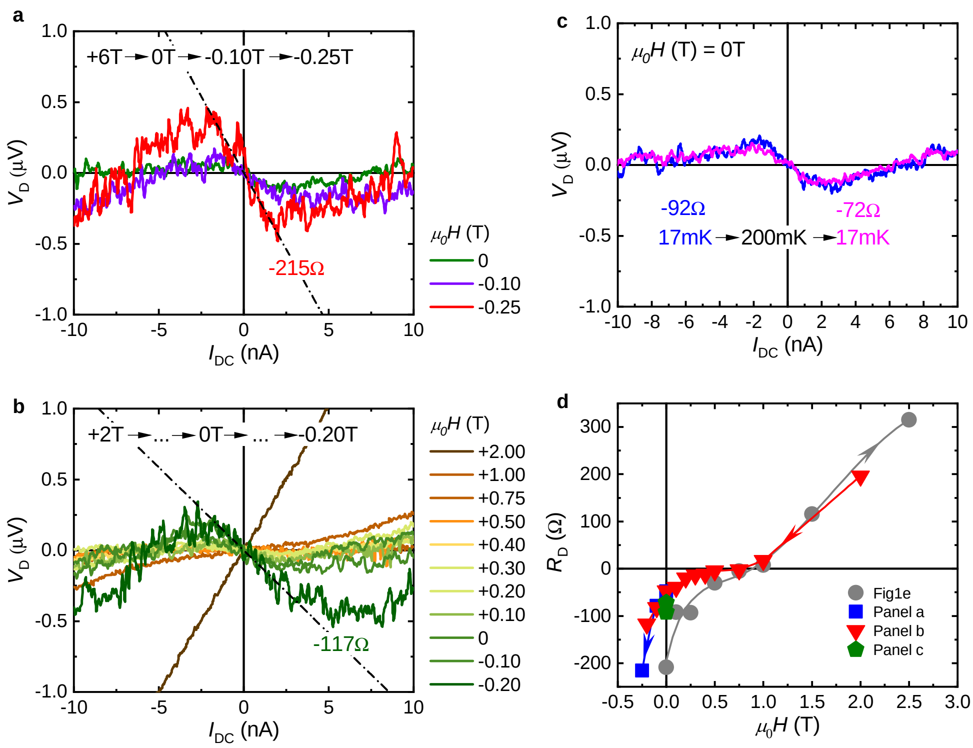

Figure S5: **Effect of the magnetic-field-sweep history observed in device A. a,** I-V characteristics measured at 17 mK in the order of 0 , -0.1, and -0.25 T directly after taking the magnetic-field-dependence data shown in Fig. S3. **b,** I-V characteristics measured at 17 mK in decreasing magnetic fields from 2 T to -0.2 T directly after taking the data shown in panel **a** and bringing the magnetic field to 2 T. The dashed lines in panel **a** and **b** show the maximum negative slopes observed at -0.25 T and -0.2 T, respectively. **c,** I-V characteristics measured at 17 mK in 0 T before (blue) and after (magenta) thermal cycling to 200 mK, directly after taking the data shown in panel **b**. **d,** Collection of the R_D values obtained in four different magnetic-field sweeps. Blue, red, and green symbols are the slopes at I_{DC} = 0 extracted from the data in panels **a**, **b**, and **c**, respectively. The gray symbols are the discrete data points up to 2.5 T shown in Fig. 1e.

Supplementary Note 6   Current- and temperature-induced breakdown of the QAHE

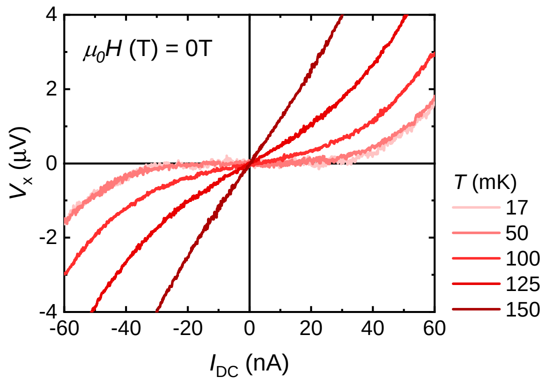

Figure S6: **Breakdown of the QAHE.** Plots of the 4-terminal longitudinal voltage V_x vs I_{DC} in 0 T ($M > 0$) measured in device A at various temperatures. The thermal activation of charge carriers with increasing temperature gives rise to a parallel dissipative conduction channel, causing the zero-resistance state of the QAHI to disappear at $\sim$100 mK, while the current-induced breakdown of the QAHE causes a finite V_x above $\sim$30 nA at 17 and 50 mK.

In Fig. 2b of the main text, the 4-terminal longitudinal resistance R_{xx} is shown as a function of temperature. The data points of R_{xx} were extracted from the I-V curves shown in Fig. S6 as the slope at I_{DC} = 0; here, the current was set to flow between contacts 1 and 4d, and the voltage between contacts 6 and 5 was measured. The 17-mK and 50-mK curves present a well extended zero-voltage plateau up to $\sim$30 nA, after which the current-induced breakdown of the QAHE occurs. At higher temperatures, the zero-resistance state is not realized due to the thermal activation of charge carriers into the gapped 2D surface states of the QAHI [1,4–6].

Supplementary Note 7 Downstream resistance measured with wider Nb electrodes

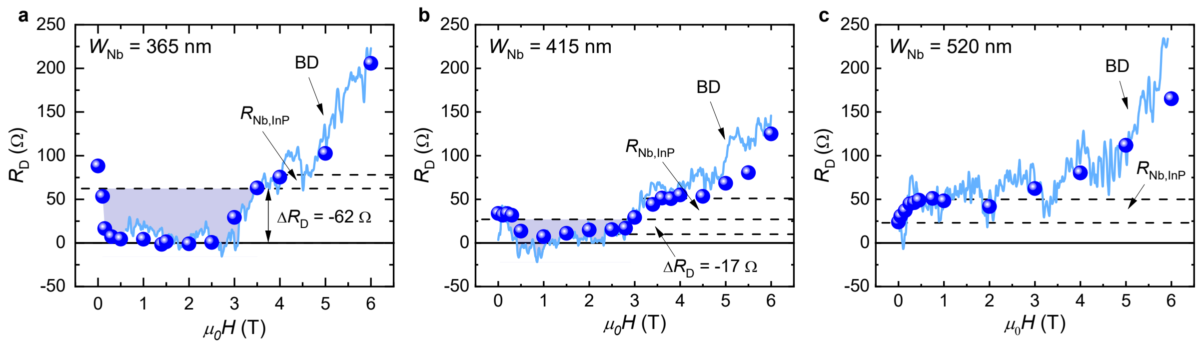

Figure S7: **Downstream resistance in devices with a wider Nb electrode. a-c,** Light blue lines show the magnetic-field dependencies of R_{D} at 25 mK measured with $I_{\mathrm{DC}} = 2$ nA in device C (**a**, $W_{\mathrm{Nb}} = 365$ nm), device D (**b**, $W_{\mathrm{Nb}} = 415$ nm) and device E (**c**, $W_{\mathrm{Nb}} = 520$ nm). Blue symbols represent the slopes in the I-V curves at I_{DC} = 0. Note that above ∼4.5 T, the breakdown (BD) of the QAHE starts to dominate R_{D} in all these devices. The distance between two dashed lines in each panel mark the estimated normal-state Nb contribution $R_{\mathrm{Nb,InP}}$ pointed by an arrow, based on which the CAR contribution ΔR_{D} is estimated.

Figure S7 shows R_{D} as a function of the applied magnetic field measured at 25 mK in devices C, D, and E having the Nb-electrode width of 365, 415, and 520 nm, respectively. Note that the increase in R_{D} above ∼4.5 T observed in all devices is due to the breakdown of the QAHE, see Fig. 1d of the main text. In devices C and D, the normal-state Nb contribution was ∼16 Ω and ∼24 Ω, yielding ΔR_{D} of about $-62\,\Omega$ and $-17\,\Omega$, respectively, when one compares R_{D} before and after the superconductivity is suppressed. In device E, on the other hand, the normal-state Nb contribution of ∼27 Ω accounts for the full increase in R_{D} upon the suppression of superconductivity. Hence, ΔR_{D} is zero for the 520-nm-wide Nb electrode of device E. The ΔR_{D} values of these devices are included in Fig. 3b of the main text.

Supplementary Note 8 Landauer-Büttiker formalism

For the measurement configuration shown in Fig. 1a of the main text, the current flows from contact 1 to 4. The chiral edge state runs counter-clockwise along the sample edge for an upward, out-of-plane magnetization. The current-voltage relation in the linear-response Landauer-Büttiker formalism [7,8] is given by

$$I_i = \sum_{j=1, j\neq 4}^{6} a_{ij} \left(V_j - V\right), \tag{S1}$$

where I_i is the current flowing into contact i, V_j is the potential at contact j, and V is the potential of the superconducting electrode (contact 4). The proportionality coefficients $a_{\mathrm{i\,j}}$ in Eq. S1 at zero temperature are given by

$$a_{ij} = \frac{e^2}{h} \left(N_i^\mathrm{e} \delta_{ij} - T_{ij}^\mathrm{ee} + T_{ij}^\mathrm{eh}\right). \tag{S2}$$

Here, N_i^e is the number of available channels for electron-like excitation in contact i:

$$N_i^\mathrm{e} = \sum_{j=1, j\neq 4}^{6} \left(T_{ij}^\mathrm{ee} + T_{ij}^\mathrm{eh}\right), \tag{S3}$$

where $T_\mathrm{ij}^\mathrm{ee}$ ($T_\mathrm{ij}^\mathrm{eh}$) is the transmission probability of an electron from the j-th contact to arrive as an electron (hole) at the i-th contact. Since a QAHI possesses only a single chiral edge state, $N_i^\mathrm{e} = 1$ for all contacts. Notice that the potential difference in Eq. S1 is expressed with respect to the potential of the grounded superconducting contact 4 ($V = V_4 = 0$), and the summation in Eqs. S1 and S3 runs only over the normal metal contacts. The non-zero transmission probabilities T_ij are simply T_{12}^ee = T_{23}^ee = T_{56}^ee = T_{61}^ee = 1, T_{35}^ee, and T_{35}^eh. The non-zero proportionality coefficients $a_{\mathrm{i\,j}}$ then become

$$a_{11} = a_{22} = a_{33} = a_{55} = a_{66} = \frac{e^2}{h}, \tag{S4}$$

$$a_{12} = a_{23} = a_{56} = a_{61} = -\frac{e^2}{h}, \tag{S5}$$

$$a_{35} = \frac{e^2}{h}\left(-T_{35}^{\mathrm{ee}} + T_{35}^{\mathrm{eh}}\right). \tag{S6}$$

Using $I_1 = -I_4 = I$ and $I_2 = I_3 = I_5 = I_6 = 0$, Eq. S1 gives a set of equations which can be solved for I and V_i. The expressions for the current I, downstream resistance $R_{\mathrm{D}}^{\mathrm{i}}$, and upstream resistance $R_{\mathrm{U}}^{\mathrm{i}}$ for an ideal (dissipationless) superconducting contact [9,10] then become

$$I = \frac{e^2}{h}\left(1 - T_{35}^{\mathrm{ee}} + T_{35}^{\mathrm{eh}}\right) V_{\mathrm{SD}}, \tag{S7}$$

$$R_{\mathrm{D}}^{\mathrm{i}} = \frac{V_{\mathrm{D}}}{I} = \frac{h}{e^2}\left(\frac{T_{35}^{\mathrm{ee}} - T_{35}^{\mathrm{eh}}}{1 - T_{35}^{\mathrm{ee}} + T_{35}^{\mathrm{eh}}}\right), \tag{S8}$$

$$R_{\mathrm{U}}^{\mathrm{i}} = \frac{V_{\mathrm{U}}}{I} = \frac{h}{e^2}\left(\frac{1}{1 - T_{35}^{\mathrm{ee}} + T_{35}^{\mathrm{eh}}}\right), \tag{S9}$$

where $V_{\mathrm{SD}} \equiv V_1 - V_4$, $V_{\mathrm{D}} \equiv V_3 - V_4$, and $V_{\mathrm{U}} \equiv V_5 - V_4$. Notice that $R_{\mathrm{U}}^{\mathrm{i}} - R_{\mathrm{D}}^{\mathrm{i}} = h/e^2$ as expected.

T_{35}^{ee} and T_{35}^{eh} are not independent parameters, they represent transmission probabilities of an electron leaving contact 5 and should satisfy the following relation:

$$T_{35}^{\mathrm{ee}} + T_{35}^{\mathrm{eh}} + T^{\mathrm{D}} = 1, \tag{S10}$$

where T^{D} is the probability of the direct transfer of the electron into the SC contact 4. The $T^{\mathrm{D}} = 0$ condition represents the case of a perfect superconductor, for which an electron with the energy smaller then the SC gap cannot enter SC contact directly, but only through Andreev processes with finite T_{35}^{eh}. In the extreme case of 100% Andreev process with T_{35}^{eh} = 1, one should observe a doubling of the current I (see Eq. S7), resulting in the maximally negative downstream resistance

$-h/(2e^2)$ (see Eq. S8). On the other hand, $T^{\mathrm{D}} = 1$ represents the case when the contact 4 acts as a perfect metal, which can be achieved in our experiment, for example, by applying a magnetic field and fully suppressing the superconductivity in the finger. In this case, $R^{\mathrm{i}}_{\mathrm{D}} = 0$ (see Eq. S8) as expected for an ideal metallic contact. For $0 < T^{\mathrm{D}} < 1$, the observation of a negative downstream resistance $R^{\mathrm{i}}_{\mathrm{D}} < 0$ is a direct indication that $T^{\mathrm{ee}}_{35} < T^{\mathrm{eh}}_{35}$ (see Eq. S8), i.e., there are more holes than electrons that arrive at contact 3.

Both T^{ee}_{35} and T^{eh}_{35} represent total probabilities for electrons and holes to get into the downstream channel after interacting with the SC finger and finally reach the contact 3. It is useful to distinguish between different contributions. In particular, crossed Andreev reflections (CAR) and direct tunneling of electrons from upstream to downstream channel (so called electron co-tunneling, CT) are expected to decay exponentially with increasing width of the finger. We can write $T^{\mathrm{ee}}_{35} = T^{\mathrm{CT}} + T^{\mathrm{N}}$ and $T^{\mathrm{eh}}_{35} = T^{\mathrm{CAR}} + T^{\mathrm{A}}$, where T^{N} and T^{A} represent the probabilities of all other processes at the finger to get into the downstream channel as an electron and hole, respectively. In most processes such as the transport through the Andreev edge state or the chiral Majorana edge state, one would expect an equal mixture of electron and hole on a long finger, i.e. $T^{\mathrm{N}} = T^{\mathrm{A}}$. Moreover, in real devices the SC-QAHI interface is never ideal and always contains a finite contact resistance R_{contact}. The expression for the apparent R_{D} is then given by

$$R_{\mathrm{D}} = R^{\mathrm{i}}_{\mathrm{D}} + R_{\text{contact}} = \frac{h}{e^2}\frac{T^{\mathrm{CT}} - T^{\mathrm{CAR}}}{1 - \left(T^{\mathrm{CT}} - T^{\mathrm{CAR}}\right)} + R_{\text{contact}}. \tag{S11}$$

This R_{D} becomes negative only when CAR occurs more often than CT and the resulting negative contribution is large enough to overcome R_{contact}. Nevertheless, even when the apparent R_{D} remains positive, one can identify negative $R^{\mathrm{i}}_{\mathrm{D}}$ by subtacting R_{contact} from the apparent R_{D}, which is done by calclulating ΔR_{D} used in the main text.

Note that in the experimental setup shown in Fig. 1a, there are two additional contributions to the downstream resistance (see Eq. 1): the resistance R_{QAHI} of the QAHI film (which is zero for low probe currents below the breakdown) and the resistance $R_{\mathrm{Nb,InP}}$ of the Nb section lying on the InP wafer between the film edge and the SC contact 4a (which is zero when the Nb is superconducting).

Supplementary Note 9 Wavefunction of chiral edge state

Following similar derivations in Refs. 11, 12, without loss of generality and neglecting coupling to the two split-off bands far from the Fermi-level that do not have a band inversion resulting from the magnetization, we write the two lowest energy states as $|+\uparrow_z\rangle = (|t\uparrow_z\rangle + |b\uparrow_z\rangle)/\sqrt{2}$ and $|-\downarrow_z\rangle = (|t\downarrow_z\rangle - |b\downarrow_z\rangle)/\sqrt{2}$, where $(+)$ is a symmetric (bonding) and $(-)$ is an antisymmetric (anti-bonding) state spread over the top and bottom surface with spin $\uparrow_z$ and $\downarrow_z$ along the magnetization axis. In the basis $(|+\uparrow_z\rangle, |-\downarrow_z\rangle)$ the Hamiltonian of the lowest energy states is then given by

$$H = \begin{pmatrix} m_k - M & -iv(k_x + ik_y) \\ iv(k_x - ik_y) & -m_k + M \end{pmatrix} = (m_k - M)\,\tau_z + v\,(k_y\tau_x + k_x\tau_y)\,, \tag{S12}$$

where $m_k = m + B(k_x^2 + k_y^2) > 0$. A magnetization $M > m$ ensures that there is a band inversion that results in the existence of the chiral edge mode.

We consider an edge state on a boundary parallel to the x-axis such that the state lives in the region $y > 0$ and k_x remains a good quantum number. For $k_x = 0$ we make the Ansatz that the edge state can be expressed $\psi(y, k_x = 0) = A\boldsymbol{\xi}\exp(-y/\lambda)$, which means that $1/\lambda$ has to satisfy

$$\left[\left(m - M - \frac{B}{\lambda^2}\right)\tau_z + \frac{iv}{\lambda}\tau_x\right]\boldsymbol{\xi} = 0, \tag{S13}$$

which has non-trivial solutions if $\boldsymbol{\xi} = (1, \chi i)/\sqrt{2}$ with $\chi = \pm 1$ and

$$\frac{1}{\lambda} = \frac{-\chi v \pm \sqrt{v^2 + 4B(m - M)}}{2B}. \tag{S14}$$

Since physical states must decay and we consider the case where the edge state is in the region $y > 0$, only $\lambda > 0$ is a valid solution. Furthermore, since $m < M$, only $\chi = -1$ ensures that both spinor components always satisfy this condition. Therefore, the edge state takes the form[11,13]:

$$\psi(y, k_x = 0) = f(y)(|t\uparrow_z\rangle + i\,|t\downarrow_z\rangle) + (|b\uparrow_z\rangle - i\,|b\downarrow_z\rangle))/\sqrt{2} = f(y)(|t\uparrow\rangle + |b\downarrow\rangle), \tag{S15}$$

where $f(y) \sim \exp(-y/\lambda)$ and $\uparrow$, $\downarrow$ refers to spin in the plane of the QAHI perpendicular to the edge (here, y-direction).

Supplementary Note 10 Difference from the $\nu = 1$ state of a quantum Hall insulator

At first sight, the chiral edge state of a QAHI appears similar to the $\nu = 1$ state of a quantum Hall insulator[14,15]. However, the spin-polarised nature of the $\nu = 1$ state necessitates, for instance, a superconductor with strong spin-orbit coupling or a nonuniform magnetic field distribution in order for CAR processes to occur[9,14,15]. In contrast, the edge state of the QAHI considered in our work is a superposition of spin states on the top and bottom surfaces. Furthermore, when brought into proximity with a superconductor, the resultant doping of the TI surface[16,17] will lead to an induced superconductivity that inherently has strong spin-orbit coupling. In a simple approximation and at zero-momentum, the wavefunction of the chiral edge in the x-direction of a QAHI takes the form of Eq. S15. If we consider an asymmetry χ between the top and bottum surfaces, the wavefunction is generalized to

$$\Psi(y) = f(y) \left(|t \uparrow\rangle + \chi \, |b \downarrow\rangle \right) . \tag{S16}$$

In the isotropic case, $\chi = 1$, the edge state has no net spin-polarisation and the CAR process will not be hindered as long as the SC finger is narrow enough. Superconducting pairing across the finger will be only slightly suppressed by a partial spin-polarisation of the edge states, which may arise in realistic situations [13]. Even in the extreme case of a fully spin-polarised edge, $\chi = 0$, CAR can still occur due to spin-orbit coupling, if the superconductivity is induced on the TI surface.

Supplementary Note 11 Quantum transport simulations

Here, we present more quantum transport simulation results for the setup of Fig. 4a. In Fig. S8, we show T_{ee} and T_{eh} as a function of the bias energy E and the disorder strength S_{dis} for fixed L_{SC} = 191 nm and W_{SC} = 260 nm in the case of no doping, i.e., without shifting the chemical potential outside of the magnetic gap into the TSC regime below the SC finger; the local current density distributions for two representative disorder levels are also shown. In this case, the top surface remains undoped and the chiral edge channel displays perfect CT at low bias and low disorder strengths. When S_{dis} becomes large enough to push the system locally out of the magnetic gap, electron-hole conversion starts to appear ($T_{\mathrm{eh}} > 0$). Note that S_{dis} is the standard deviation of the Gaussian random field added to the on-site energies to simulate the disorder potential. At larger S_{dis}, the disordered region is effectively doped and T_{eh} fluctuates around 0.5 with a large standard

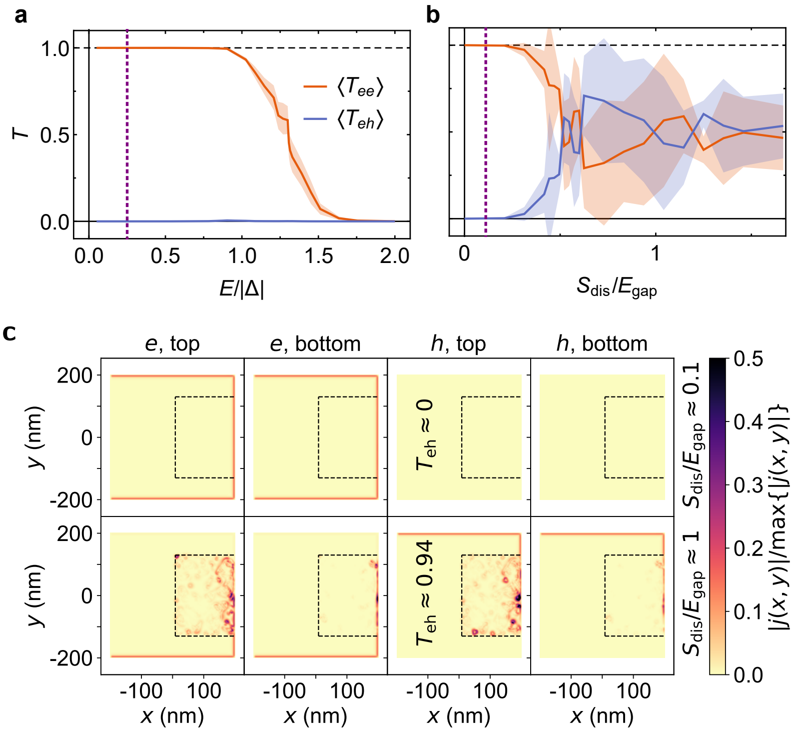

Figure S8: **Quantum transport simulation of proximitized QAHI without doping from the SC finger. a,b,** $\langle T_{ee} \rangle$ and $\langle T_{eh} \rangle$ obtained after averaging the results for various disorder distributions (one standard deviation is indicated by shading) shown as a function of bias energy E ($|\Delta|$ = 10 meV) in **a**, and as a function of the disorder strength S_{dis} (relative to the magnetic gap E_{gap} = 90 meV) in **b**. The disorder strength (bias energy) considered in the calculations for **a** (**b**) is indicated by the dashed purple line in **b** (**a**). Here, we fixed L_{SC} = 191 nm and W_{SC} = 260 nm. **c,** Components of the local current densities for $S_{\mathrm{dis}}/E_{\mathrm{gap}} = \frac{1}{9}$ (top) and $S_{\mathrm{dis}}/E_{\mathrm{gap}} = \frac{10}{9}$ (bottom) at the bias energy $E/|\Delta| = \frac{1}{8}$; for the latter, a disorder configuration that gave a particularly high T_{eh} is chosen for demonstration purpose.

deviation. This scenario is unlikely to apply to the experimental setup, as the QAHI state is well established in the sample. This suggests that a TSC phase due to uniform doping below the SC finger is needed in the proximitized top surface in order to mediate Andreev processes of the chiral edge channel with its peculiar spin polarization [see Eq. (S15)]. Note that, with this simulation setup, we do not consider alternative (trivial) scenarios, e.g., the possibility of the QAHI edge state leaking into a subgap state in the SC finger and undergoing Andreev processes there before going back into the QAHI edge state as a hole. Furthermore, note that we model the SC lead (shown in Fig. 4a) by a two-dimensional tight-binding model that is lattice-matched to the TI thin film model, considering parameters for a free electron gas with s-wave pairing (Δ). It is only relevant for energies above the SC gap $|\Delta|$ when QP tunneling into the SC lead is possible, yielding $T_{\mathrm{ee}} + T_{\mathrm{eh}} < 1$ (see Fig. S8a). However, in the presence of vortices, tunneling into the SC lead is possible even for $E < |\Delta|$, causing $T_{\mathrm{ee}} + T_{\mathrm{eh}} < 1$ even at low energies.

In Fig. S9, we present T_{eh} as a function of the SC finger length L_{SC} as in Fig. 4b, but for different biases and disorder strengths. Increasing the disorder strength reduces the amplitude of the Majorana edge channel interference pattern around the average $T_{\mathrm{eh}} \leq 0.5$, whereas increasing the bias energy pushes down the amplitude of the interference pattern towards $T_{\mathrm{eh}} = 0$. This indicates that, for obtaining a clean Majorana edge-channel interference pattern in wide fingers and for identifying a qualitatively different CAR/CT-dominated regime in narrow fingers, disorder and bias should be sufficiently small compared to the magnetic gap and the proximity-induced pairing potential.

Although our quantum transport simulations for narrow SC fingers indeed support the possibility of CAR to take place in the QAHI edge, they do not yield a regime with $T_{\mathrm{eh}} > 0.5$ that is robust against small variations in the setup (e.g., finger width or bias energy). This is different from experiment. As we mentioned in the main text, there should be additional physics which causes the stable dominance of CAR in real situations. One such possibility is the dissipation into subgap states in the SC finger (not included in our simulation setup, where $T_{\mathrm{ee}} + T_{\mathrm{eh}} = 1$ is as-

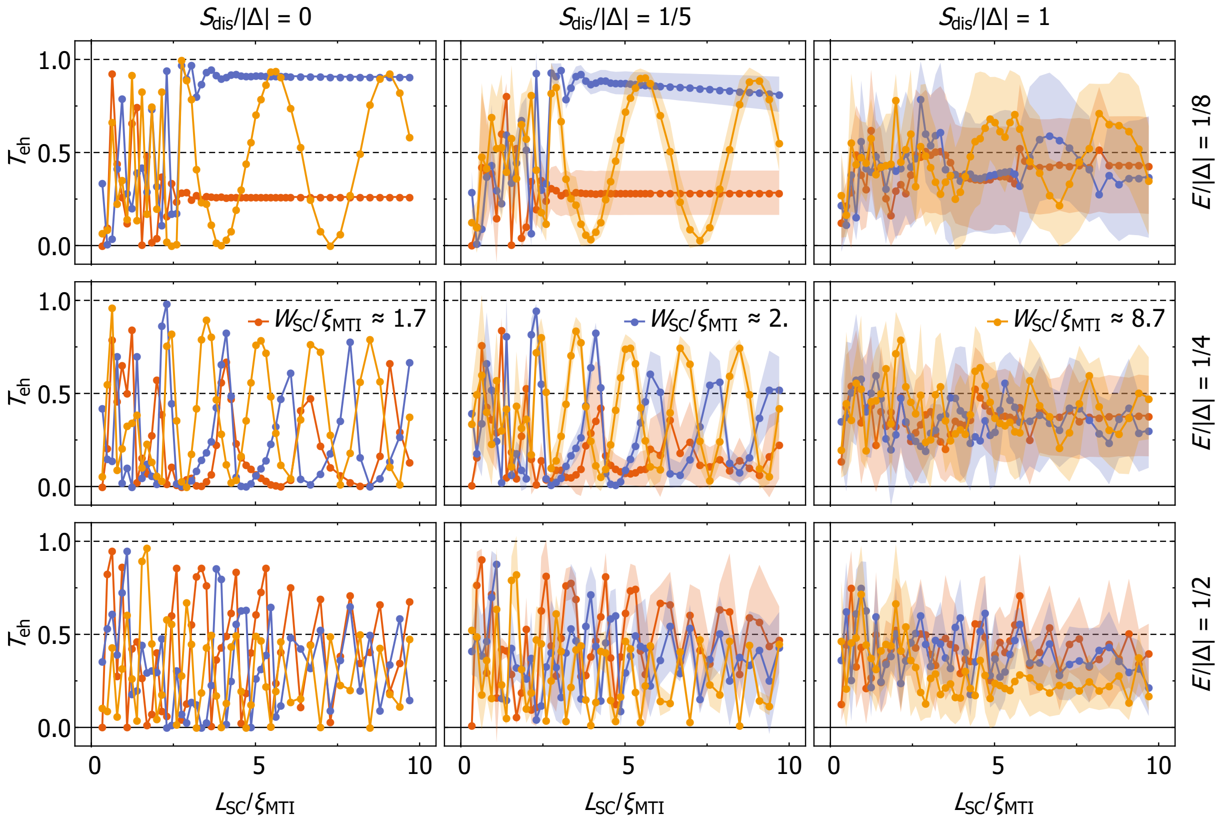

Figure S9: **Quantum transport simulation of crossed Andreev reflection in a proximitized QAHI (extended).** The disorder-averaged electron-hole conversion probability T_{eh} (standard deviation indicated by shading) as a function of SC finger length as in Fig. 4b for different energies E and disorder strengths S_{dis} for three selected SC finger widths (orange, blue, and dark-yellow colour correspond to $W_{\mathrm{SC}}/\xi_{\mathrm{MTI}}$ values of 1.7, 2.0, and 8.7, respectively).

sumed for all subgap energies $E < |\Delta|$), as suggested in Ref. 10. When tunneling of electrons into the SC (which leads to dissipation) is allowed at low energies in addition to the tunneling into the downstream edge, the CT process would compete more with such a tunneling process than CAR, yielding $\langle T_{\mathrm{eh}} \rangle > \langle T_{\mathrm{ee}} \rangle$ even when CAR and CT are equally likely in the case without dissipation. We can further speculate that such an (imbalanced) dissipative process only starts to appear when the SC finger is narrow enough, because for wide fingers the chiral Majorana edge channels are well formed and they may short-circuit the tunneling processes.

We note that our simulations considered the TSC state with a single Majorana mode per edge ($\mathcal{N}$ = 1). Theoretically, there can also be a different TSC state with double Majorana modes per edge ($\mathcal{N}$ = 2) [18]. If a TSC state with $\mathcal{N}$ = 2 is realized on the undoped (or only slightly doped) QAHI surface as considered in Ref. 18, the $\mathcal{N}$ = 2 edge state is equivalent to a single chiral QAH edge state and it provides a direct path for an incoming edge electron to travel to the downstream as argued in Ref. 18, leading to a large positive ΔR_{D} especially for wide fingers where CAR is suppressed. We never observed such a positive ΔR_{D} for wide fingers, and therefore we believe that this scenario is not likely. The other possibility to have a TSC state with $\mathcal{N}$ = 2 is that both top and bottom surfaces are sufficiently doped and each hosts a TSC state with $\mathcal{N}$ = 1, such that the total $\mathcal{N}$ number becomes 2. In this case, the edge state will surround the finger and the transport of electrons and holes for a long and wide finger will self-average to give zero contribution to ΔR_{D}, similar to the case of the Andreev edge state of a trivial SC phase.

Supplementary Note 12 Comparison of the up- and downstream resistances

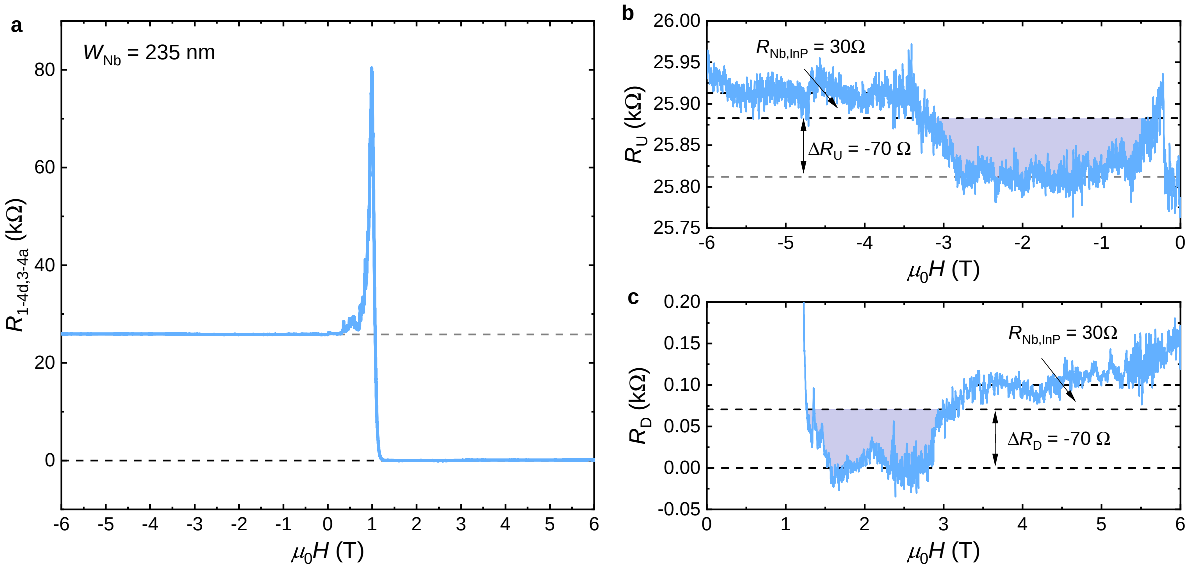

Figure S10: **Magnetic-field dependence of the up- and downstream resistances for the 235-nm-wide Nb electrode of device B. a,** The three-terminal resistance $R_{\text{1-4d,3-4a}}$ changes by h/e^2 when crossing the coercive field upon up-sweep. **b,** Zoom of $R_{\text{1-4d,3-4a}}$ for negative field values where it corresponds to R_{U}. **c,** Zoom of $R_{\text{1-4d,3-4a}}$ for positive field values where it corresponds to R_{D}. The relation $R_{\text{U}} - R_{\text{D}} = h/e^2$ holds in both the SC and the normal states.

In this work, the focus was made on the measurements of R_{D}, because a negative R_{D} presents a clear signature of the CAR process. However, according to Eqs. S8-S9, R_{U} should change in the corresponding manner so that $R_{\text{U}} - R_{\text{D}}$ always yields the quantized value h/e^2. Figure S10 shows $R_{\text{1-4d,3-4a}}$ upon sweeping the magnetic field from -6 T to $+6$ T. For the negative field range up to the coercive field of the QAHI thin film, $R_{\text{1-4d,3-4a}}$ corresponds to R_{U}, whereas beyond the coercive field $R_{\text{1-4d,3-4a}}$ corresponds to R_{D}. One can see that $\Delta R_{\text{U}} = \Delta R_{\text{D}} = -70\ \Omega$ and the relation $R_{\text{U}}(-H) - R_{\text{D}}(+H) = h/e^2$ indeed holds in both the SC and the normal states.

Supplementary Note 13 Effect of sample magnetization on the Nb superconductivity

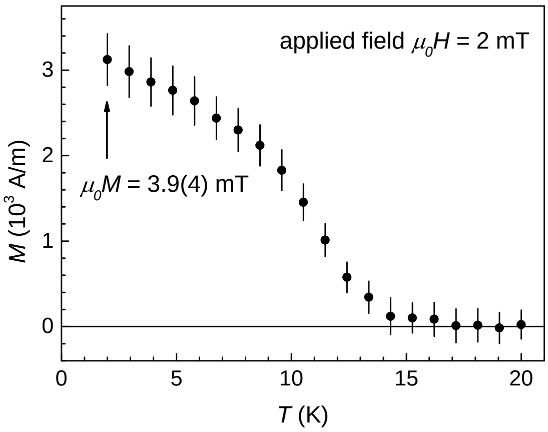

Figure S11: **Magnetization measured using SQUID magnetometry.** Magnetization (M) between 2 and 20 K, after applying at 2 K a saturating field ($\mu_0 H$) of 7 T and reducing it to 2 mT, i.e. to a near-remanence state, and measuring the magnetization upon heating keeping the applied 2 mT field. A non-zero positive field was applied to avoid that trapped-field effects associated with the superconducting magnet could result in an effectively negative applied magnetic field. The error bars are determined based on conventional error propagation, taking into account (i) the standard deviation of multiple SQUID magnetometry measurements at each constant temperature step, (ii) the subtraction of the diamagnetic contribution from the substrate, (iii) the normalization of the magnetic moment with respect to the film volume.

The vicinity to a ferromagnetic film may be detrimental to the superconducting properties of the Nb electrode, due to the magnetic field originating from the film. In order to evaluate if such effects could play a role in our experiments, we carried out magnetization measurements of our QAHI samples using SQUID magnetometry (Quantum Design MPMS®3). The typical magnetization of our samples was found to be about 3×10^3 A/m at 2 K, corresponding to a magnetic induction of about 4 mT. This is well below the lower critical field of Nb, which is $H_{c1} \approx 180$ mT [19]. As an example, Fig. S11 shows the near-remanence magnetization as a function of temperature, measured from 2 to 20 K. Given the square hysteresis of our QAHI films (at 2 K and below), the near-remanent magnetization measured here is approximately equal to both the

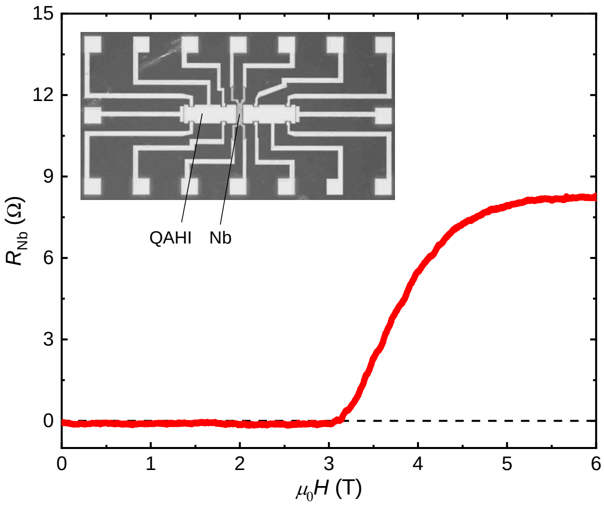

Figure S12: **Magnetic-field dependence of the resistance of a 20-μm-wide Nb strip lying across of a 100-μm-wide QAHI Hall-bar device.** The magnetic field was applied perpendicular to the film. A picture of the device is shown in the inset.

remanant and saturation magnetizations. These magnetization values are expected to only slightly increase when the temperature is further decreased from 2 K to the mK temperatures used in the transport experiments reported here, since 2 K is already significantly below the Curie temperature (Fig. S11). Hence, for all relevant conditions in the experiments presented here (temperature and applied magnetic field), the magnetic induction originating from the QAHI film is negligible compared to the applied magnetic fields as well as to the critical field of niobium.

To directly confirm that the Nb superconductivity is not affected by the magnetization of the QAHI film, we also measured the SC properties of a 20-μm-wide Nb strip lying across a 100-μm-wide QAHI Hall-bar device. The inset of Fig. S12 shows a picture of the device, and the main panel shows a typical magnetic-field dependence of the Nb-strip resistivity, which is similar to that of our Nb finger electrodes on the InP substrate. We found no evidence for weakened superconductivity in this Nb strip. Hence, the potentially detrimental effect of the QAHI film on the Nb superconductivity can safely be neglected.

Supplementary Note 14 Magnetic-field dependence of the extrinsic contact resistance

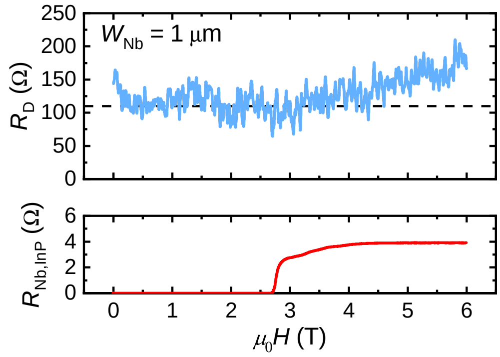

Figure S13: **Magnetic-field dependence of R_D for the 1-μm-wide Nb electrode of device G, shown together with $R_{Nb,InP}$.** The value of R_D, measured at 25 mK with $I_{RMS} = 1$ nA, remained essentially unchanged up to about 4.5 T, above which R_D starts to increase due to the breakdown of the QAH effect. The size of $R_{RNb,InP}$ is much smaller than the noise level in R_D, making its contribution above 3 T to be hardly visible.

In our analysis of ΔR_D, we assumed that the extrinsic contact resistance $R_{contact}$ due to an imperfect Nb-QAHI interface included in Eq. 1 of the main text remains unchanged across the superconducting transition of the Nb electrode. To verify this assumption, we measured R_D for a 1-μm-wide Nb electrode (device G) together with $R_{Nb,InP}$ of this finger, and the results are shown in Fig. S13. In this wide electrode, we did not observe any noticeable change in R_D across the SC transition at around ~2.8 T within the noise level of about 50 Ω. This result justifies our calculation of ΔR_D using Eq. 1 of the main text (assuming a constant $R_{contact}$ across H_{c2}) within an uncertainty of about 50 Ω.

Supplementary Note 15 Estimation of errors

The ΔR_{D} values shown in Fig. 3b of the main text contain uncertainties, which are indicated with error bars. The main source of the uncertainty comes from the assumption that R_{contact} is constant across the SC transition, which is justified within the uncertainty of 50 Ω as discussed in the previous section. The other source of errors is the uncertainties in the determination of the values of $R_{\mathrm{D}}(H < H_{\mathrm{c2}})$ and $R_{\mathrm{D}}(H > H_{\mathrm{c2}})$. Here, the measurement noise of about 3 Ω gives one contribution. An additional contribution occurs when the observed $R_{\mathrm{D}}(H > H_{\mathrm{c2}})$ is constantly increasing, as was the case for our samples C and D shown in Fig. S7; for these samples, we considered extra errors of 16 Ω and 24 Ω, respectively. These considerations lead to the estimated total errors of 56 Ω (devices A, B, E), 72 Ω (device C), and 80 Ω (device D).

Supplementary Note 16 Estimation of the induced SC gap on the QAHI surface

By identifying ξ_{CAR} as the induced SC coherence length, one can try to infer the induced SC gap Δ_{ind} in the QAHI surface. Since the surface-state mean free path ℓ_{mfp} of our QAHI fims is unknown, we take 5 nm as a typical value for the surface of a TI device [20]. Using $v_F = 4 \times 10^5$ m/s [21] with the same dirty-limit formula as for Nb, we obtain $\Delta_{\mathrm{ind}} \approx 0.04$ meV, which is only 3% of the Nb gap. This Δ_{ind} is probably a lower bound, since other effects of proximate Nb, such as v_F renormalization and screening of charge impurities, would make ℓ_{mfp} longer. Nevertheless, considering the presence of ferromagnetism, a small Δ_{ind} is reasonable. Note that if the 2D surface is so disordered that only puddles of metallic regions are induced, such a patchy system cannot support CAR/CT processes which require superconducting coherence.

References:

1. Kawamura, M. et al. Current-driven instability of the quantum anomalous Hall effect in ferromagnetic topological insulators. Phys. Rev. Lett. **119**, 016803 (2017).

2. Bestwick, A. J. et al. Precise quantization of the anomalous hall effect near zero magnetic field. Phys. Rev. Lett. **114**, 187201 (2015).

3. Kou, X. et al. Scale-invariant quantum anomalous hall effect in magnetic topological insulators beyond the two-dimensional limit. Phys. Rev. Lett. **113**, 137201 (2014).

4. Fox, E. J. et al. Part-per-million quantization and current-induced breakdown of the quantum anomalous Hall effect. Phys. Rev. B **98**, 075145 (2018).

5. Fijalkowski, K. M. et al. Quantum anomalous Hall edge channels survive up to the Curie temperature. Nat. Commun. **12**, 5599 (2021).

6. Lippertz, G. et al. Current-induced breakdown of the quantum anomalous Hall effect. Phys. Rev. B **106**, 045419 (2022).

7. Datta, S. Electronic Transport in Mesoscopic Systems. Cambridge Studies in Semiconductor Physics and Microelectronic Engineering (Cambridge University Press, 1995).

8. Lambert, C. J. & Raimondi, R. Phase-coherent transport in hybrid superconducting nanostructures. J. Phys.: Condens. Matter **10**, 901–941 (1998).

9. Galambos, T. H., Ronetti, F., Hetényi, B., Loss, D. & Klinovaja, J. Crossed Andreev reflection in spin-polarized chiral edge states due to the Meissner effect. Phys. Rev. B **106**, 075410 (2022).

10. Hatefipour, M. et al. Induced superconducting pairing in integer quantum Hall edge states. Nano Lett. **22**, 6173–6178 (2022).

11. Yu, R. et al. Quantized anomalous Hall effect in magnetic topological insulators. Science **329**, 61–64 (2010).

12. Zhang, R.-X., Hsu, H.-C. & Liu, C.-X. Electrically tunable spin polarization of chiral edge modes in a quantum anomalous Hall insulator. Phys. Rev. B **93**, 235315 (2016).

13. Shen, J. et al. Spectroscopic fingerprint of chiral Majorana modes at the edge of a quantum anomalous Hall insulator/superconductor heterostructure. Proc. Nat. Acad. Sci. **117**, 238–242 (2020).

14. Lee, G.-H. et al. Inducing superconducting correlation in quantum Hall edge states. Nat. Phys. **13**, 693–698 (2017).

15. Gül, O. et al. Andreev reflection in the fractional quantum Hall state. Phys. Rev. X **12**, 021057 (2022).

16. Legg, H. F., Loss, D. & Klinovaja, J. Metallization and proximity superconductivity in topological insulator nanowires. Phys. Rev. B **105**, 155413 (2022).

17. Rüßmann, P. & Blügel, S. Proximity induced superconductivity in a topological insulator. arXiv:2208.14289 (2022).

18. Wang, J., Zhou, Q., Lian, B. & Zhang, S.-C. Chiral topological superconductor and half-integer conductance plateau from quantum anomalous Hall plateau transition. Phys. Rev. B **92**, 064520 (2015).

19. Saito, K. Critical field limitation of the niobium superconducting rf cavity. In The 10th Workshop on RF Superconductivity, Tsukuba, Japan, 583–587 (2001).

20. Ghatak, S. et al. Anomalous Fraunhofer patterns in gated Josephson junctions based on the bulk-insulating topological insulator $BiSbTeSe_2$. Nano Lett. **18**, 5124–5131 (2018).

21. Yoshimi, R. et al. Dirac electron states formed at the heterointerface between a topological insulator and a conventional semiconductor. Nat. Mater. **13**, 253–257 (2014).

Chapter 3

Non-Majorana-origin of the half-quantized conductance in SC-QAHI heterostructures

This chapter is presented in the form of a manuscript and the preprint is available on arXiv as

A. Uday,* G. Lippertz,* B. Bhujel, A. A. Taskin, and Y. Ando, *Non-Majorana-origin of the half-integer conductance quantization elucidated by multi-terminal superconductor-quantum anomalous Hall insulator heterostructure*, arXiv:2411.14903 (2024)

A. A. T. and Y. A. conceived the project. A. U., G. L., B. B., and A. T. did the MBE growth of the ferromagnetic thin films. A. U. optimized the fabrication recipe for acquiring a transparent SC-QAHI interface. A. U. and G. L. did the device fabrication. A. U. did the transport data acquisition and analysis, with the help of G. L., A. A. T., and Y. A. The manuscript was written by A. U. and Y. A., with input from all authors.

3.1 Overview

This chapter discusses the edge transport in a multi-terminal SC-QAHI heterostructure using the LB formalism. The aim is to obtain a deeper understanding on the origin of the half-quantized two-terminal conductance, measured in a QAHI Hall-bar with a superconducting strip lying across the full width of the device. In 2011, Chung *et al.* predicted that this feature is a signature of the chiral Majorana edge transport in a proximitized QAHI in the topological superconductor (TSC) phase with $\mathcal{N} = 1$ [13, 23]. Let us recall the phase diagram for a QAHI proximitized by an s-wave SC, discussed in chapter 1 and reproduced in Fig. 3.0a. When an external magnetic field is applied opposite to the magnetization direction of this SC-QAHI system, the out-of-plane magnetization of the QAHI can be inverted. During such a magnetization reversal, the amplitude of the magnetization strength λ undergoes a sign change, as depicted in Fig. 3.0a by the dotted

*A. U. and G. L. contributed equally to this work.

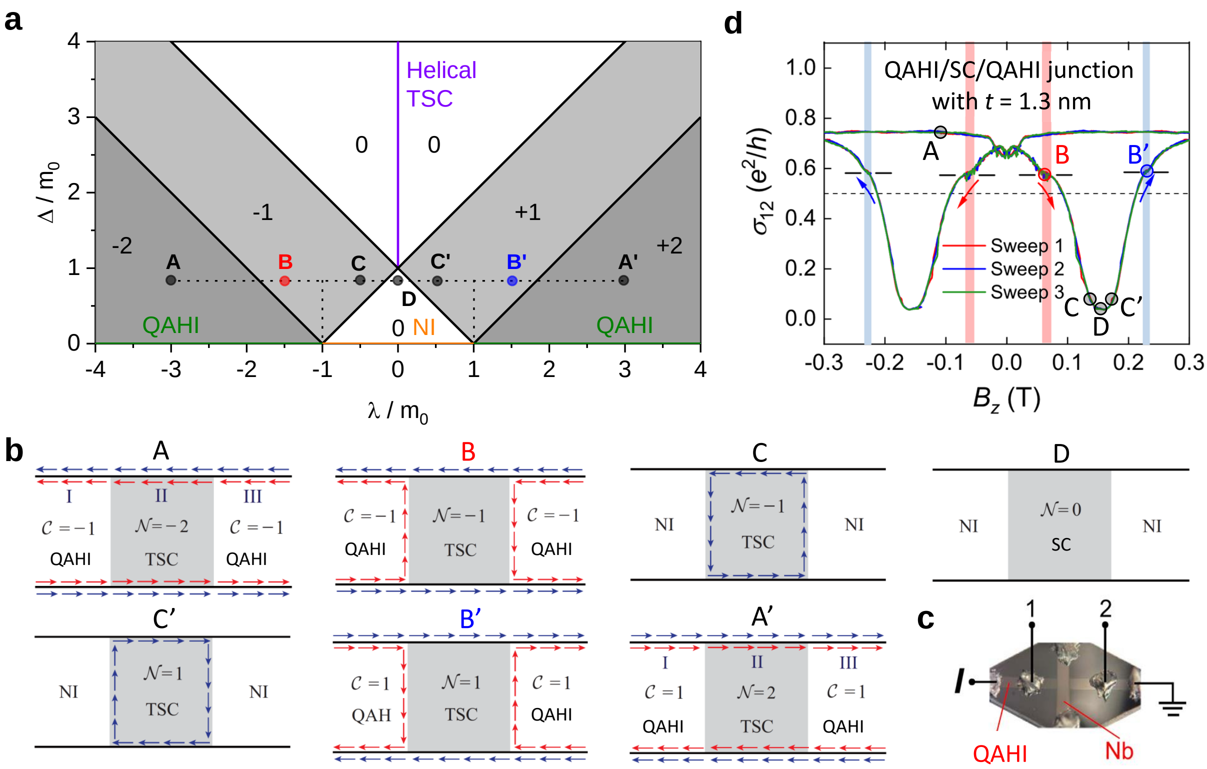

Fig. 3.0 | Half-integer conductance quantization in SC-QAHI heterostructures. **a**, Phase diagram of the proximitized QAHI with regions of different Chern number $\mathcal{N} = \pm 0$ (white), ± 1 (gray), and ± 2 (dark gray). The solid black lines $\Delta/m_0 = \pm\lambda/m_0 \pm 1$ mark the band closings of the topological transitions (see Eqs. 1.17-1.18), where Δ, λ and m_0 represent the induced superconducting gap, the magnetization strength and the hybridization gap. The QAHI, normal insulator (NI), and helical TSC phases are marked by the green, orange, and purple lines, respectively. The dotted line from label A to A' corresponds to a magnetization reversal from $-\lambda$ to $+\lambda$. **b**, The chiral Majorana edge transport configuration for labels A, B, C, D, C', B', and A, in panel a. Note that the unproximitized regions of the QAHI (shown in white) follow the same horizontal path from $\Delta/m_0 = -3$ to $+3$ in panel a, but at $\Delta/m_0 = 0$. Reprinted figure with permission from Ref. [13]. © Copyright (2015) by the American Physical Society. **c**, A picture of a QAHI ribbon with a superconducting Nb strip lying across the full width of the device. The measurement configuration to determine the two-terminal conductance σ_{12} for panel d is shown. **d**, The magnetic field dependence of σ_{12} measured across the QAHI-SC-QAHI junction with a 1.3-nm-thick AlO_x layer inserted between the Nb and QAHI thin film. Panels c and d reproduced from Ref. [81] with permission. © IOP Publishing. All rights reserved.

line from A to A'. This causes the proximitized QAHI to undergo several topological phase transition, in which the Chern number changes as: $\mathcal{N} = -2$ (A) $\rightarrow -1$ (B-C) $\rightarrow 0$ (D) $\rightarrow$ $+1$ (C'-B') $\rightarrow +2$ (A') (see Eqs. 1.17-1.18 for details).

Figure 3.0b shows schematic representations of the corresponding chiral Majorana edge state configurations for a QAHI ribbon in which the middle region is proximitized. For situation A, the unproximitized QAHI regions with $\Delta = 0$ (shown in white) have a Chern number of $\mathcal{C} = -1$. This is topologically equivalent to the TSC phase (shown in gray) with $\mathcal{N} = -2$. Consequently, Chung *et al.* predicted a perfect transmission of the two chiral Majorana modes on the top and bottom edges of the sample [13, 23]. When the amplitude of λ is reduced to B, one chiral Majorana edge mode is lost in the TSC. Now the unproximitized QAHI and TSC regions are topologically different, creating a topological phase boundary between them, hosting one chiral Majorana edge mode. In this case, one chiral Majorana edge mode is transmitted longitudinally through the TSC (shown by the blue arrows) and the other transversely to the counter-propagating edge on the other side of the sample (red arrows). Since only one of the two Majorana modes (i.e. half of a chiral Dirac fermion mode) is transmitted, the two-terminal conductance σ_{12} is predicted to decrease from e^2/h at A to $e^2/(2h)$ at B [13, 23]. When the amplitude of λ is reduced further to C, the unproximitized QAHI regions enter the trivial normal insulator (NI) phase with $\mathcal{C} = 0$, when $|\lambda|$ becomes smaller than the hybridization gap $|m_0|$ (see Eqs. 1.7 for details). In this case, no edge states are transmitted and $\sigma_{12} \approx 0$. When λ becomes zero in D, the proximitized region of the QAHI becomes a trivial SC with $\mathcal{N} = 0$. In this state, the sample has zero net magnetization. By increasing the magnitude of the external magnetic field, the sample can then be magnetized in the other direction, causing λ to increase from 0 at D to $3m_0$ at A'. Here, A', B', and C' are equivalent to A, B, and C, respectively, but with an opposite chirality of the edge states.

In 2017, He *et al.* claimed to have observed these topological transitions in the hysteresis loop of the two-terminal conductance as $\sigma_{12} = e^2/h \leftrightarrow e^2/(2h) \leftrightarrow 0 \leftrightarrow e^2/(2h) \leftrightarrow e^2/h$ plateaus, when the external magnetic field is swept [82]. However, the data came under immediate scrutiny [26–29], and the publication was ultimately retracted under suspicion of scientific misconduct in 2022 [83]. Nevertheless, the first author recently published a second work [81] investigating the SC-QAHI heterostructure, shown in Fig. 3.0c. The claim is that by introducing an AlO_x oxide barrier between the QAHI and SC the formation of an electrical short through the SC electrode is suppressed, whereas the superconducting proximity effect survives up to slightly higher barrier thicknesses. Note that the formation of an electrical short via the SC between the counter-propagating edge states on opposite sides of the QAHI sample would effectively turn the SC-QAHI heterostructure into two QAHI connected in series by the SC [29]. Hence, such an electrical short would be a trivial origin for the $e^2/(2h)$ two-terminal conductance, as compared to e^2/h for a QAHI without a superconducting strip.

Figure 3.0d shows the magnetic-field dependence of the two-terminal conductance σ_{12} of the device shown in Fig. 3.0c with an AlO_x oxide barrier of $\sim$1.3 nm. The observations of kinks at $\sigma_{12} \approx 0.57$-$0.59\, e^2/h$ in the magnetic-field sweeps are interpreted as signatures of the $\mathcal{N} = 1$ TSC state, whereas the samples shows $\sigma_{12} \approx 0.74\, e^2/h$ in the supposed $\mathcal{N} = 2$ TSC state at large fields B_z [81]. The quantization of σ_{2T} is very poor, only to within 10-30% of the expected values for a TSC with $\mathcal{N} = 1$ and 2. Moreover, the two-terminal measurement set-up has two major disadvantages: Firstly, it is not possible to disentangle the longitudinal sample resistance from the quantized resistance at the superconducting electrode. For example, the kinks at $\sigma_{12} \approx 0.57\text{-}0.59\, e^2/h$ in Fig. 3.0d could also be caused by temperature effects [6] or inhomogeneous switching of the magnetization [84, 85], affecting the longitudinal conductance of the QAHI film. Secondly, the set-up does not allow to individually determine the potentials of the two edge states leaving from the superconducting electrode.

In the manuscript presented in this chapter, the Landauer-Büttiker formalism is used to reevaluate the proposed half-integer-quantized two-terminal conductance as a signature of the superconducting proximity effect in a QAHI hall-bar with a μm-size SC lying across the width of the device. By including equilibration mechanisms for the edge states, like through the formation of chiral Andreev edge states (CAESs) and a single-particle current into the SC via subgap states, it is shown that the $e^2/(2h)$ feature is *not* unique to Majorana edge transport. Moreover, the formulas derived in the manuscript are used to analyze the experimental results on multi-terminal devices made of V-doped $(Bi_xSb_{1\text{-}x})_2Te_3$ thin films proximitized by Nb superconducting electrodes. Rather than to only characterize the two-terminal conductance, the potentials of all the chiral edge states in the multi-terminal devices are individually determined. From this analysis it is unambiguously shown that the half-integer-quantized two-terminal conductance arises from the edge state equilibration of the two chiral edge states arriving at the superconducting electrode (in agreement with Ref. [29]). This is a trivial effect which also occurs in the absence of superconductivity (i.e. for magnetic fields larger than the upper critical field of Nb).

Lastly, while the QAHI devices with sub-μm-size superconducting electrodes in chapter 2 showed clear evidence of the superconducting proximity effect in the form of a negative downstream resistance R_D, in this chapter it will be shown that the chiral 1D edge states leaving from a μm-size SC always have a potential equal to that of the SC, i.e. $R_\mathrm{D} = 0$. This suggests that signatures of the superconducting proximity effect in proximitized QAHI films can only be observed within the length scale of the superconducting coherence length, unlike the case of NbTiN-InAs heterostrutures in the quantum Hall regime [72] (see Fig. 1.13).

Editors' Suggestion

Non-Majorana origin of the half-integer conductance quantization elucidated by multiterminal superconductor–quantum anomalous Hall insulator heterostructure

Anjana Uday [*], Gertjan Lippertz [*], Bibek Bhujel, Alexey A. Taskin [†] and Yoichi Ando [‡]
Physics Institute II, University of Cologne, D-50937 Köln, Germany

(Received 14 November 2024; accepted 7 January 2025; published 22 January 2025)

Chiral one-dimensional transport can be realized in thin films of a surface-insulating ferromagnetic topological insulator called quantum anomalous Hall insulator (QAHI). When superconducting (SC) pairing correlations are induced in the surface of such a material by putting an s-wave superconductor on the top, the resulting topological superconductivity gives rise to chiral Majorana edge modes. A quantized two-terminal conductance of $\frac{1}{2}(e^2/h)$ was proposed as a smoking-gun evidence for the topological SC phase associated with a single chiral Majorana edge mode. There have been experiments to address this proposal, but the conclusion remains unclear. Here we formulate the edge transport in a multiterminal superconductor–QAHI heterostructure using the Landauer-Büttiker formalism. Compared to the original proposal for the $\frac{1}{2}(e^2/h)$ quantization based on a simple two-terminal model, our formalism allows for deeper understanding of the origin of the quantization. The analysis of our experiments on multiterminal devices unambiguously shows that the half-integer conductance quantization arises from the equilibration of the potentials of the incoming edge states at the SC electrode, and hence it is not of Majorana origin.

DOI: 10.1103/PhysRevB.111.035440

I. INTRODUCTION

A thin film of a surface-insulating ferromagnetic topological insulator showing the quantum anomalous Hall effect (QAHE) [1–3] is called quantum anomalous Hall insulator (QAHI). Inducing superconducting (SC) correlations in a QAHI through the SC proximity effect has been actively pursued in recent years, because it would lead to exotic topological superconductivity hosting one-dimensional (1D) chiral Majorana edge modes [4,5]. The creation of a π-phase domain boundary in these edge modes is predicted to lead to mobile Majorana zero modes, which could transfer quantum information between stationary topological qubits [6–8]. Alternatively, if two counterpropagating chiral edge states of a QAHI is brought close together, either by etching a trench in the QAHI film or by etching the QAHI film into a nanostrip, then introduction of SC correlations between these two edges via the crossed Andreev reflection (CAR) using the SC proximity effect would lead to a quasi-1D topological superconductor with a pair of Majorana zero modes at the ends [9–12]. Hence, the proximitized QAHI constitutes an interesting platform for Majorana physics.

The QAHE showing the Hall resistance quantized to h/e^2 with vanishing longitudinal resistance is realized by doping ultrathin films of the 3D TI material $(Bi_xSb_{1-x})_2Te_3$ with Cr or V, and fine-tuning the composition x to move the chemical potential into the magnetic gap opened at the Dirac point of the surface states as a result of the ferromagnetic order [1–3].

No conclusive evidence was reported for the SC proximity effect in a QAHI [13–15] until the recent observation of a negative resistance due to CAR across a narrow Nb finger electrode on top of a V-doped $(Bi_xSb_{1-x})_2Te_3$ thin film by our group [16]. The negative nonlocal potential in the downstream edge stemming from the holes created as a result of the CAR process was observed only when the width of the Nb electrode was less than ~500 nm. Since this experiment had a long finger-shaped SC electrode which promotes the CAR process beneath the finger, it is an interesting question if the negative resistance of different origin, such as Majorana interference [17,18] or Andreev edge-state transport [19,20], could be observed over a longer length scale in a differently-shaped electrode as a signature of SC proximity effect.

Another possible signature of the SC proximity effect in a QAHI is the quantized two-terminal conductance of $\frac{1}{2}(e^2/h)$ [5]: If a topological SC phase with only one Majorana edge mode ($\mathcal{N} = 1$) [4] is realized as a result of the SC proximity effect underneath a SC strip lying across the full width of a QAHI [Fig. 1(a)], then one chiral Majorana edge mode is transmitted longitudinally across the SC strip and the other transversely to the counterpropagating edge state on the other side of the sample, leading to the conductance of $\frac{1}{2}(e^2/h)$ [5,21]. This reduction in two-terminal conductance by a factor of two, as compared to e^2/h for a bare QAHI without a SC strip, was experimentally observed [13,22], but its origin is still under intense debate as other trivial mechanisms were proposed [13,22–26].

In the present work, we use the Landauer-Büttiker formalism to reevaluate the proposed half-integer-quantized two-terminal conductance as a signature of the SC proximity effect in a QAHI Hall bar with a micrometer-size SC electrode lying across the width of the device. With the formula

[*]These authors contributed equally to this work.
[†]Contact author: taskin@ph2.uni-koeln.de
[‡]Contact author: ando@ph2.uni-koeln.de

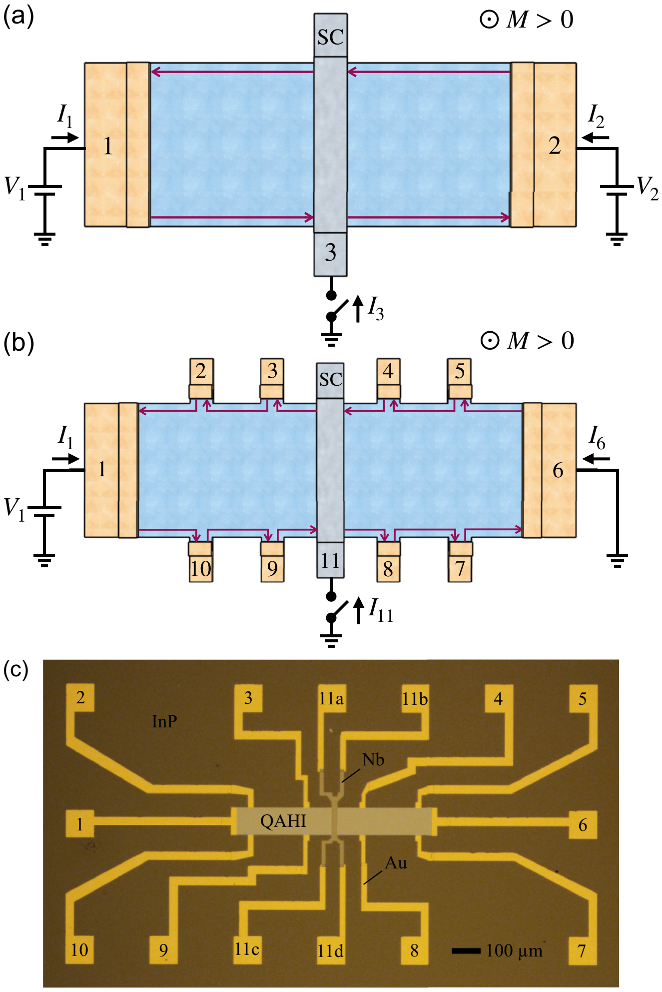

FIG. 1. (a) Simple two-terminal setup on a QAHI thin film, in which contacts 1 and 2 are normal-metal contacts and the SC contact 3 can be grounded. (b) Schematic for a multiterminal Hall bar with the SC electrode 11 lying across the center of the device. Contacts 1 to 10 are normal-metal contacts. Current can flow into the QAHI film through contacts 1, 6, and 11. The other contacts are floating and serve as voltage probes. The chiral edge state of the QAHI is represented by the red arrows and shown for an upward, out-of-plane magnetization ($M > 0$). (c) False-color image of the measured multiterminal Hall bar device A with a SC Nb electrode lying across the center of the V-doped $(Bi_xSb_{1-x})_2Te_3$ thin film. The overlap of the superconductor with the QAHI thin film is $20 \times 100\ \mu m^2$.

derived for a multiterminal device made on such a structure [Fig. 1(b)], we analyze our experimental results on thin films of V-doped $(Bi_xSb_{1-x})_2Te_3$ proximitized by micrometer-size Nb superconducting electrodes. Rather than to only characterize the two-terminal conductance, we individually determine the potentials of all the chiral edge states in our multiterminal devices. We show unambiguously that the half-integer-quantized two-terminal conductance arises from the edge state equilibration of the two chiral edge states arriving at the SC electrode (in agreement with Ref. [13]). This is a trivial effect which also occurs in the absence of superconductivity. Last, no negative nonlocal edge potentials are observed in our devices, suggesting that signatures of the SC proximity effect in proximitized QAHI films can only be observed within the length scale of the SC coherence length, unlike the case of NbTiN-InAs heterostrutures in the quantum Hall insulator (QHI) regime which employs SC electrodes of similar (or even larger) sizes [20].

II. HALF-INTEGER CONDUCTANCE QUANTIZATION

It is instructive to revisit the original prediction of the half-integer quantization of the two-terminal conductivity for a QAHI Hall bar with an s-wave superconductor strip lying across the full width of the device [5,21], as shown in Fig. 1(a). To allow for Andreev scattering within the linear-response Landauer-Büttiker formalism [27,28], the current-voltage relation can be written as

$$I_{\mathrm{i}} = \sum_{j=1}^{3} a_{\mathrm{ij}}(V_{\mathrm{j}} - V_{\mathrm{SC}}), \tag{1}$$

where I_{i} is the single-particle current flowing into contact i, V_{j} is the potential at contact j, and $V_{\mathrm{SC}} = V_3$ is the potential of the SC electrode (contact 3). The proportionality coefficients a_{ij} in Eq. (1) at zero temperature are given by

$$a_{\mathrm{ij}} = \frac{e^2}{h}\left(N_{\mathrm{i}}^{\mathrm{e}}\delta_{\mathrm{ij}} - T_{\mathrm{ij}}^{\mathrm{ee}} + T_{\mathrm{ij}}^{\mathrm{eh}}\right), \tag{2}$$

where $N_{\mathrm{i}}^{\mathrm{e}}$ is the number of available channels for electron-like excitation in contact i and $T_{\mathrm{ij}}^{\mathrm{ee}}$ ($T_{\mathrm{ij}}^{\mathrm{eh}}$) is the transmission coefficients of an electron from the jth contact to arrive as an electron (hole) at the ith contact. For the setup shown in Fig. 1(a), the relevant transmission coefficients are then:

$$\begin{aligned} T_{1,1}^{\mathrm{ee}} &= T_{2,2}^{\mathrm{ee}} \equiv T_T^{\mathrm{ee}}, \\ T_{1,1}^{\mathrm{eh}} &= T_{2,2}^{\mathrm{eh}} \equiv T_T^{\mathrm{eh}}, \\ T_{1,2}^{\mathrm{ee}} &= T_{2,1}^{\mathrm{ee}} \equiv T_L^{\mathrm{ee}}, \\ T_{1,2}^{\mathrm{eh}} &= T_{2,1}^{\mathrm{eh}} \equiv T_L^{\mathrm{eh}}, \\ T_{1,3}^{\mathrm{ee}} &= T_{3,1}^{\mathrm{ee}} = T_{2,3}^{\mathrm{ee}} = T_{3,2}^{\mathrm{ee}} \equiv T^D, \end{aligned}$$

with $T_T^{\mathrm{ee}} + T_T^{\mathrm{eh}} + T_L^{\mathrm{ee}} + T_L^{\mathrm{eh}} + T^D = 1$, where the subscripts "L" and "T" refer to the transmission of a particle longitudinally underneath the SC strip and transversely across the width of the Hall bar along the SC strip, respectively. T_L^{ee} and T_T^{ee} describe all the processes for an electron arriving at the SC electrode with an energy smaller than the SC gap to leave as an electron in one of the two edge states originating from the superconductor; these processes include: electron co-tunneling (CT), the transmission through chiral Andreev edge states (CAESs), and the transmission through chiral Majorana edge modes (CMEMs). T_L^{eh} and T_T^{eh} describe all the processes that result in an electron arriving at the SC electrode with an energy smaller than the SC gap to leave as a hole in one of the two edge states originating from the superconductor; these processes include CAR, CAESs, and CMEMs. Moreover, T^D is included to describe single electrons entering the SC electrode with an energy smaller than the SC gap though subgap states, e.g., via the interaction with vortices or due to the presence of a soft gap.

Using Eqs. (1) and (2), it is then easy to show that:

$$\frac{I_1 - I_2}{V_1 - V_2} = \frac{e^2}{h}(1 + k), \tag{3}$$

with

$$k \equiv \left(T_L^{ee} - T_L^{eh}\right) - \left(T_T^{ee} - T_T^{eh}\right). \tag{4}$$

Notice that within the expression for k the T_i^{ee} and T_i^{eh} coefficients are competing with each other, as well as the longitudinal and transverse processes.

For a floating SC electrode ($I_1 = -I_2$), or when the voltage is applied symmetrically ($V_1 = -V_2$) with respect to a grounded SC electrode ($V_3 = 0$), the expression for the two-terminal (2T) conductance becomes

$$\sigma_{2T} = \frac{I_1}{V_1 - V_2} = \frac{e^2}{2h}(1 + k). \tag{5}$$

The fact that Eq. (5) only depends on the parameter k is the first disadvantage of using the two-terminal conductance to characterize the SC proximity effect; it is not possible to extract the individual transmission coefficients.

In the original proposals [5,21], Chung *et al.* predicted that for a proximitized QAHI in the $\mathcal{N} = 1$ topological SC state, the transmission coefficients obey the constraint $T_T^{ee} = T_T^{eh} = T_L^{ee} = T_L^{eh}$, as one chiral Majorana edge mode is transmitted underneath the SC electrode and the other across the width of the Hall bar along the SC strip. For the $\mathcal{N} = 2$ topological SC state with two CMEMs, they predicted $T_T^{ee} = T_T^{eh} = T_L^{eh} = 0$, as both chiral Majorana edge modes are transmitted underneath the SC electrode. The expressions for the two-terminal conductance [Eq. (5)] then become

$$\sigma_{2T} = \frac{e^2}{2h} \quad \text{for} \quad \mathcal{N} = 1, \tag{6}$$

$$= \frac{e^2}{2h}(2 - T^D) \quad \text{for} \quad \mathcal{N} = 2. \tag{7}$$

Chung *et al.* did not include T^D in their original model [5,21], resulting in perfect half-integer and integer quantization of σ_{2T} for $\mathcal{N} = 1$ and $\mathcal{N} = 2$, respectively. However, if the single-particle current into the SC electrode is large ($T^D \approx 1$), then the $\mathcal{N} = 2$ topological SC state will also give $\sigma_{2T} = e^2/(2h)$.

It is important to point out that (i) this half-integer σ_{2T} signature is not unique to the above-mentioned choice of transmission coefficients and can show up for many combinations of T_L^{ee}, T_L^{eh}, T_T^{ee}, and T_T^{eh}. (ii) The situation where $T_L^{ee} = T_L^{eh}$ and $T_T^{ee} = T_T^{eh}$ corresponds to the QAH edge states leaving the SC electrode as an equal superposition of electron and hole, carrying a potential equal to the chemical potential of the SC electrode. As pointed out before [12,13], this does not require chiral Majorana edge modes and occurs naturally for chiral Andreev edge states traveling along a SC electrode over a long distance; for example in the case of a superconductor-QHI heterostructure over many skipping orbits. (iii) If the single-particle current into the SC electrode is large ($T^D \approx 1$), then the two-terminal conductance is always $\sigma_{2T} \approx e^2/2h$. In this case the superconductor is indistinguishable from a normal metal contact. Hence, the half-integer quantization of the two-terminal conductivity is *not* a smoking gun evidence for the $\mathcal{N} = 1$ topological SC state in a proximitized QAHI.

III. EXPERIMENTS ON MULTITERMINAL HALL-BAR DEVICES WITH A SC STRIP

Hatefipour *et al.* observed a negative downstream resistance with respect to a 150-μm-wide grounded SC electrode in NbTiN-InAs heterostructures in the quantum Hall regime [20]. This is a remarkably long length scale as compared to the SC coherence length of NbTiN, which poses the question whether negative nonlocal resistances can also be observed in proximitized QAHI heterostructures containing micrometer-size SC electrodes. For this purpose, we added additional voltage terminals to our devices, see Figs. 1(b) and 1(c). By measuring the four-terminal resistances of our multiterminal Hall bar devices with SC strip, we can directly determine the potential of the downstream edge. This configuration also helps to better understand the cause of the $e^2/(2h)$ quantization.

We will limit our discussion to the case of an upward, out-of-plane magnetization ($M > 0$) of the QAHI thin films, which corresponds to a counterclockwise motion of the chiral 1D edge state. Note that under time-reversal symmetry, the transmission coefficients change as $T_{ij}(M > 0) = T_{ji}(M < 0)$, which means the expressions for the resistances across SC electrode defined below change as: $R_{3\text{-}4}(M > 0) = R_{9\text{-}8}(M < 0)$ and $R_{3\text{-}4}(M < 0) = R_{9\text{-}8}(M > 0)$.

A. Fabrication details

The QAHI samples used in this study are uniformly V-doped $(Bi_xSb_{1-x})_2Te_3$ thin films with a thickness of ∼8 nm, grown on InP (111)A substrates by molecular beam epitaxy in an ultra-high vacuum (UHV) environment. The details of the growth were already published in Refs. [16,29]. Atomic layer deposition at 80°C (Ultratec Savannah S200) is used to cover the freshly grown films *ex situ* with a 4-nm-thick Al_2O_3 capping layer to avoid degradation in air. The Hall bar devices are patterned using standard optical lithography techniques. The Nb/Au SC contacts (45/5 nm for device A and 90/5 nm for device B) and the Ti/Au normal metal contacts (5/45 nm) are defined using electron-beam lithography. Aluminum etchant (Transene, Type-D) at 50°C is used to selectively remove the Al_2O_3 capping layer before the sputter-deposition of the Ti/Au and Nb/Au layers in UHV. All QAHI films in this work display a quantized R_{yx} and vanishing R_{xx} without the need of electrostatic gating, see Fig. 2(b).

This fabrication process was previously shown to result in good proximitization of V-doped $(Bi_xSb_{1-x})_2Te_3$ thin films with a low contact resistance [16]. Hence, it is reasonable to assume, that by following the same recipe for the fabrication of the micrometer-size Nb electrodes in this work, the V-doped $(Bi_xSb_{1-x})_2Te_3$ underneath is also well proximitized.

B. Floating SC electrode

First, we treat the experimental setup in which the SC contact 11 is floating, and the current flows from contact 1 to 6, see Fig. 1(b). This is the same setup as used in

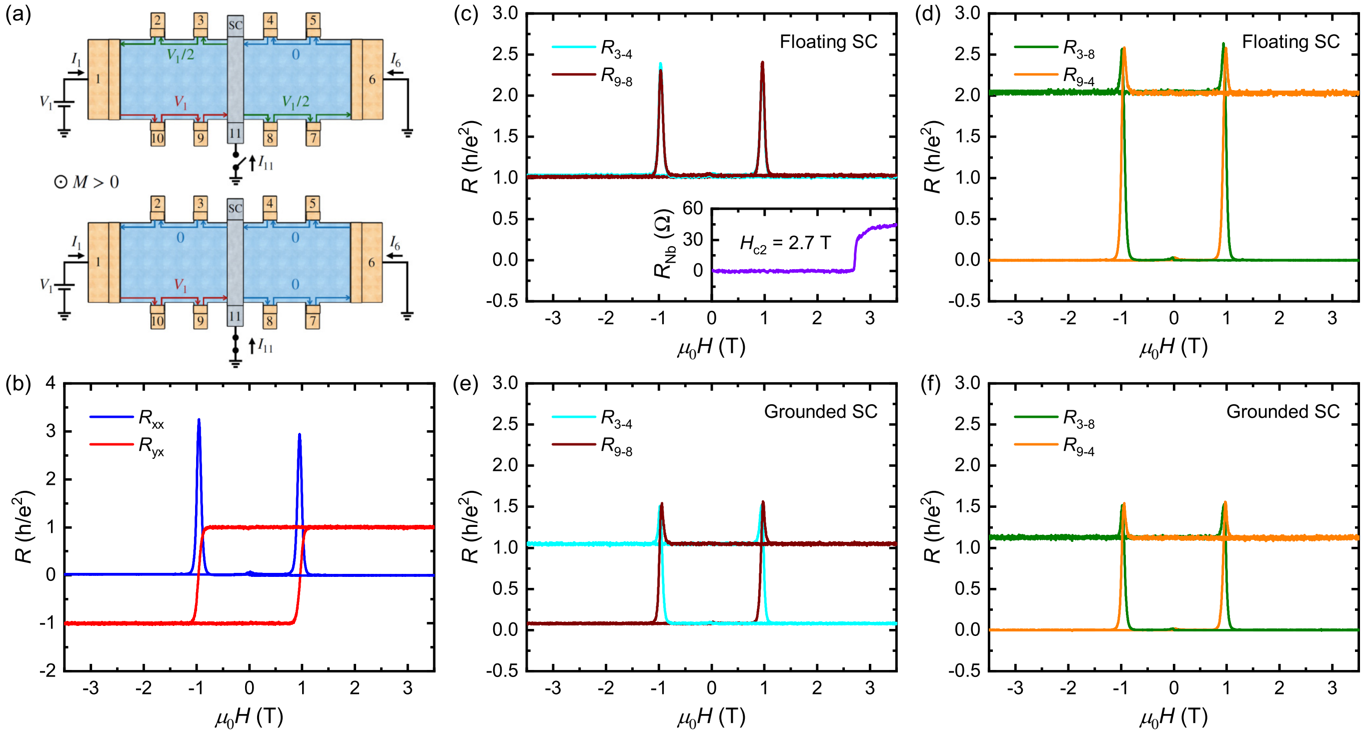

FIG. 2. (a) Schematic of the floating and grounded configurations, with the allowed edge potentials indicated near the arrows to show the edge states. (b) Longitudinal (transverse) resistance R_{xx} (R_{yx}) at 65 mK for device A, showing a vanishing (quantized) value indicative of a clean QAHE realized in our device even after fabrication. [(c)–(f)] The magnetic-field dependencies of the resistances $R_{i\text{-}j} \equiv (V_i - V_j)/I_1$ at 65 mK for device A, measured between contacts i and j divided by the total current flowing into contact 1 ($I_1 = 1$ nA), for the floating [(c) and (d)] and grounded [(e) and (f)] configurations. From these resistance values, the edge potentials shown in (a) can be inferred. Inset of (c): Nb-electrode resistance vs external magnetic field, showing the upper critical field $H_{c2} \approx 2.7$ T.

Refs. [13,22], which investigated σ_{2T} for a superconductor-QAHI heterostructures. Solving Eq. (1) with $I_1 = -I_6$ together with Eqs. (A1) and (A2) from the Appendix, yields

$$V_{11} = \frac{V_1 + V_6}{2} = \frac{V_2 + V_7}{2}, \tag{8}$$

independent of the choice of T^D, T_L^{ee}, T_L^{eh}, T_T^{ee}, and T_T^{eh}. Equation (8) shows that when the SC strip is floating, V_{11} equilibrates the incoming edge state potentials (V_1 and V_6), but the outgoing chiral edge states need not be at the same potential (V_2 and V_7).

The resistances across the SC strip, $R_{3\text{-}4}$ and $R_{9\text{-}8}$, then become

$$\frac{V_3 - V_4}{I_1} = \frac{V_9 - V_8}{I_1} = \frac{h}{e^2}\frac{(1-k)}{(1+k)}, \tag{9}$$

with k given by Eq. (4). Note that $R_{3\text{-}4}$ and $R_{9\text{-}8}$ cannot become negative, since $-1 \leqslant k \leqslant 1$.

Figures 2(c) and 2(d) shows the magnetic-field dependencies of the resistances measured across the Nb strip for this floating configuration. The potentials of the chiral edge states leaving the SC electrode are then easily determined: $V_3 \approx V_8 \approx V_1/2$, as illustrated in Fig. 2(a) (top). This corresponds to $k \approx 0$. Notice that $R_{3\text{-}4}$ and $R_{9\text{-}8}$ remain unchanged when the magnetic field is swept (even for $H > H_{c2}$), with the exception of the peaks at the coersive field where the sample's magnetization inverts. This means that if the sample undergoes a $\mathcal{N} = 1$ to $\mathcal{N} = 2$ topological SC phase transition, it cannot be seen in the transport data. Note that the value of $R_{3\text{-}4} \approx R_{9\text{-}8} \approx h/e^2$ corresponds to a two-terminal conductance $\sigma_{2T} \approx e^2/(2h)$ for the sample.

The observation of $k \approx 0$ can have two origins, i.e., either the single-particle current into the superconductor is large ($T^D \approx 1$), or the transmission coefficients are $T_T^{ee} \approx T_T^{eh}$ and $T_L^{ee} \approx T_L^{eh}$ as the CMEMs (or CAESs) at the superconductor-QAHI interface become an equal superposition of electron and hole for such large SC electrodes. In both cases, the superconductor essentially acts as a good metal contact, equilibrating the potentials of the incoming edge states. This is in agreement with the earlier report by Kayyalha *et al.* [13]. In passing, the concept of edge-state equilibration also plays an important role [30–34] in understanding the peculiar conductance quantization across a quantum point contact made on the $\nu = 2/3$ fractional quantum Hall state [35,36].

C. Grounded SC electrode

Next we ground both the SC contact 11 and the metallic contact 6 (i.e., $V_{11} = V_6 = 0$). This setup is similar to the nonlocal measurement of the downstream resistance performed with respect to a grounded SC electrode on top of (fractional) QHI and QAHI thin films [12,16,19,20,37]. The resistances across the SC strip then become

$$R_{3\text{-}4} = \frac{V_3 - V_4}{I_1} = \frac{h}{e^2}\frac{\left(T_T^{ee} - T_T^{eh}\right)}{\left(1 - T_T^{ee} + T_T^{eh}\right)}, \tag{10}$$

$$R_{9\text{-}8} = \frac{V_9 - V_8}{I_1} = \frac{h}{e^2}\frac{\left(1 - T_L^{ee} + T_L^{eh}\right)}{\left(1 - T_T^{ee} + T_T^{eh}\right)}, \tag{11}$$

where $R_{3\text{-}4}$ is negative when $T_T^{eh} > T_T^{ee}$. For this grounded configuration, the resistances no longer depend on the parameter k. By combining various measurement configurations, one can now determine the amplitudes of T_L^{ee}, T_L^{eh}, T_T^{ee}, and T_T^{eh} independently. Notice that $R_{3\text{-}4}$ is sensitive to the transverse transmission coefficients.

To probe the longitudinal transmission coefficients T_L^{ee} and T_L^{eh}, it is useful to measure the resistance $R_{8\text{-}4}$ given by

$$R_{8\text{-}4} = \frac{V_8 - V_4}{I_1} = \frac{h}{e^2}\frac{\left(T_L^{ee} - T_L^{eh}\right)}{\left(1 - T_T^{ee} + T_T^{eh}\right)}, \tag{12}$$

which becomes negative when $T_L^{eh} > T_L^{ee}$; note that this $R_{8\text{-}4}$ is different from the usual transverse resistance $R_{yx} = -(V_8 - V_4)/I_6 = +h/e^2$, see Eq. (A4) in the Appendix. Hence, the grounded SC configuration allows for a straightforward differentiation between (T_L^{ee}, T_L^{eh}) and (T_T^{ee}, T_T^{eh}), unlike the floating superconductor configuration where all the resistances only depend on k [Eq. (4)].

Figures 2(e) and 2(f) show the magnetic-field dependencies of the resistances measured across the Nb strip for this grounded configuration. The potentials of the chiral edge states leaving the SC electrode are found to be $V_3 \approx V_8 \approx V_6 = 0$, as illustrated in Fig. 2(a) (bottom). This corresponds again to the Nb strip equilibrating the potentials of the incoming edge states. However, notice that $R_{3\text{-}4}(M > 0)$ and $R_{9\text{-}8}(M < 0)$ in Fig. 2(e) are now nonzero and positive, respectively. Similarly, $R_{3\text{-}8}(M > 0)$ and $R_{9\text{-}4}(M < 0)$ in Fig. 2(f) deviate strongly from h/e^2. Rather than to attribute this to $T_T^{ee} > T_T^{eh}$ and $T_L^{ee} > T_L^{eh}$, we interpret this to be an artifact of nonideal contacts. In an actual experiment, both contacts 11 and 6 will always have a finite contact resistance to the QAHI film. This will cause the current to be divided between the two grounds [see Eq. (A5) in the Appendix]. In device A, we estimate ~8% of the total current flew through contact 6.

Regardless of the above-mentioned artifact, the resistances in Figs. 2(e) and 2(f) do not change as the magnetic field is increased above the upper critical field of Nb $H_{c2} = 2.7$ T [see inset of Fig. 2(c)]. This leads us to conclude that $T_T^{ee} \approx T_T^{eh}$ and $T_L^{ee} \approx T_L^{eh}$.

D. Floating SC electrode with trench

It is important to investigate whether the observation of $T_T^{ee} \approx T_T^{eh}$ and $T_L^{ee} \approx T_L^{eh}$ in our experiment could correspond to the $\mathcal{N} = 1$ topological SC state, in which one chiral Majorana edge mode is transmitted underneath the SC electrode and the other across the width of the Hall bar along the SC strip [5,21]. We fabricated a second Hall-bar device where the QAHI thin film is interrupted by a 10-μm-wide gap underneath the SC electrode (30 × 100 μm^2). This ensures that $T_L^{ee} = T_L^{eh} = 0$ and no chiral Majorana mode can be transmitted. All the current flowing from contact 1 to 6 has to go through the SC electrode now. Nevertheless, we still find the same edge potentials for the floating configuration: $V_3 = (1 - k)V_1/2 \approx V_1/2$ and $V_8 = (1 + k)V_1/2 \approx V_1/2$, as can be deduced from Fig. 3. Hence, $k = T_T^{eh} - T_T^{ee} \approx 0$ for this device. This means that the edge potentials remain unchanged regardless of how the contact is made to the SC electrode.

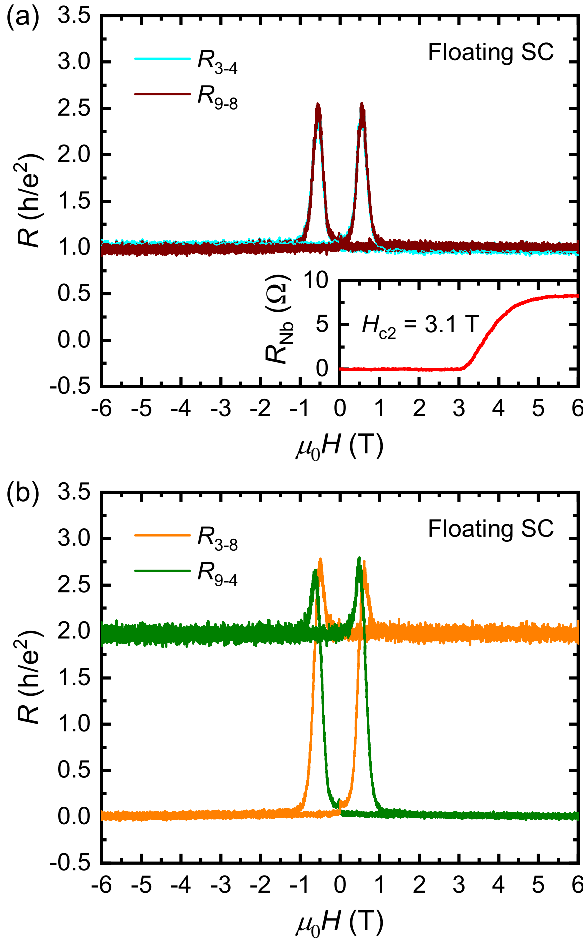

FIG. 3. [(a) and (b)] The magnetic-field dependencies of the resistances $R_{i\text{-}j} \equiv (V_i - V_j)/I_1$ at 65 mK for device B in the floating configuration. In this device, the QAHI film is interrupted by a 10-μm-wide gap underneath the SC electrode, creating two Hall-bar regions connected in series via the Nb strip. Inset of (a): Nb-electrode resistance vs external magnetic field, showing the upper critical field $H_{c2} \approx 3.1$ T.

E. Absence of negative nonlocal resistance

Last, we comment on possible negative downstream potentials measured with respect to the floating SC electrode, as the observation of negative potentials is complicated in the grounded configuration due to the presence of two grounded contacts. A negative potential can, in principle, be observed for V_2 or V_7 as an offset from the equilibrated potential $V_{11} = (V_1 + V_6)/2$ of the floating superconductor, see Eq. (8). The resistances measured with respect to the floating SC

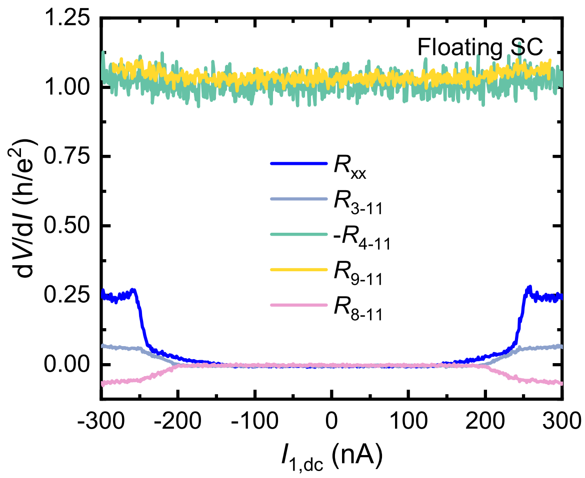

FIG. 4. Differential resistances at 17 mK measured as a function of the dc bias current flowing into contact 1 with a small ac excitation of 1 nA, for device A in the floating configuration. The measurement setup is shown in Fig. 2(a). The resistances $R_{3\text{-}11}$ and $R_{8\text{-}11}$ are zero at low dc bias, meaning that there are no signatures of CAR or CT processes. At high bias, the resistances become dominated by the breakdown of the QAHE at $I_{\mathrm{BD}} \approx 235$ nA [29], with already a slight onset of dissipation at ~140 nA. The sample was magnetized at +1.5 T before performing the $\mathrm{d}V/\mathrm{d}I$ measurements at 0 T.

contact 11 then become

$$R_{3\text{-}11} = -R_{8\text{-}11} = -\frac{h}{e^2}\frac{k}{(1+k)}, \tag{13}$$

$$R_{4\text{-}11} = -R_{9\text{-}11} = -\frac{h}{e^2}\frac{1}{(1+k)}, \tag{14}$$

where $R_{3\text{-}11}$ or $R_{8\text{-}11}$ can become negative depending on k [Eq. (4)]. Notice that $R_{8\text{-}11}$ (and $R_{4\text{-}11}$) are defined in the direction opposite to the current flow. This means that at elevated temperature or high bias current the nonzero longitudinal resistance can cause $R_{8\text{-}11}$ to become negative as well. The measurement setup used for Eqs. (13) and (14) has an advantage over the setup used in Refs. [12,16,19,20,37], where the SC electrode was grounded. Namely, when performing the experiment on a real device there will be no extrinsic contact resistance contribution to the resistances in Eqs. (13) and (14), as they are measured in a four-terminal configuration.

Figure 4 shows the differential resistances measured with respect to the floating SC electrode 11, together with the longitudinal resistance R_{xx}, as a function of the dc bias current. The sample remains in the zero-resistance state up to ~140 nA, after which there is an onset of dissipation in R_{xx} in the prebreakdown regime [38]. At $I_{\mathrm{BD}} \approx 235$ nA the sharp increase in R_{xx} signifies the breakdown of the QAHE [29,38–43], likely due to the electric-field-driven percolation of charge puddles across the width of the sample [29]. As a result, the negative value of $R_{8\text{-}11}(M > 0)$ stems from the nonzero longitudinal resistance at high dc bias current. At low bias, before the onset of dissipation, $R_{8\text{-}11}(M > 0)$ is zero in Fig. 4. Hence, no negative downstream resistances are observed when a V-doped $(\mathrm{Bi}_x\mathrm{Sb}_{1\text{-}x})_2\mathrm{Te}_3$ QAHI is proximitized by a micrometer-size SC electrode on top of the film.

This means that, unlike the case of a superconductor-QHI system based on InAs [20], the signatures of SC proximity effect in QAHI require a SC electrode with dimensions of the order of the (induced) coherence length. When it is satisfied, T_L^{eh} and T_T^{eh} correspond to the probabilities of crossed Andreev reflection at the SC electrode in the longitudinal and transverse directions, respectively. The corresponding electron cotunneling processes are then described by T_L^{ee} and T_T^{ee}, respectively. In this regard, the recent submicrometer-size Hall bars of QAHI reported in Ref. [40,41] may be a good platform to observe negative nonlocal resistances if SC electrodes are fabricated with dimensions comparable to the (induced) SC coherence length [16].

IV. CONCLUSION

We have shown that the proposed detection of the chiral Majorana edge mode in a superconductor-QAHI heterostructure through the observation of a two-terminal conductance of $e^2/(2h)$ is ill conceived. This conclusion was derived by formulating a Landauer-Büttiker model for the relevant multiterminal setup and performing experiments to elucidate the transmission coefficients, using multiterminal devices made of V-doped $(\mathrm{Bi}_x\mathrm{Sb}_{1\text{-}x})_2\mathrm{Te}_3$ thin films proximitized by Nb superconductor. Any experimental results on the two-terminal configuration can be explained by the SC electrode equilibrating all the chiral edge state potentials, possibly due to the presence of in-gap states at the superconductor-QAHI interface. While the submicrometer-size SC electrodes in our previous study showed clear evidence of the SC proximity effect in the form of negative downstream edge potentials [16], the chiral 1D edge states leaving from the micrometer-size SC electrodes in the present study always had a potential equal to that of the SC electrode. This shows that SC contacts on the order of the (induced) SC coherence length are required for the study of the SC proximity effect.

ACKNOWLEDGMENTS

This work has received funding from the Deutsche Forschungsgemeinschaft (DFG, German Research Foundation) under CRC 1238-277146847 (subprojects A04 and B01) and also from the DFG under Germany's Excellence Strategy–Cluster of Excellence Matter and Light for Quantum Computing (ML4Q) EXC 2004/1-390534769.

DATA AVAILABILITY

The data that support the findings of this article are openly available [44].

APPENDIX: DETAILS OF MULTITERMINAL TRANSPORT ANALYSIS

1. Transmission and proportionality coefficients

For an upward, out-of-plane magnetization ($M > 0$), the relevant transmission coefficients for the setup shown in Fig. 1(b) are as follows:

$$T_{3,4}^{\mathrm{ee}} = T_{8,9}^{\mathrm{ee}} = T_L^{\mathrm{ee}} \quad \text{and} \quad T_{3,4}^{\mathrm{eh}} = T_{8,9}^{\mathrm{eh}} = T_L^{\mathrm{eh}},$$

$$T_{3,9}^{\mathrm{ee}} = T_{8,4}^{\mathrm{ee}} = T_T^{\mathrm{ee}} \quad \text{and} \quad T_{3,9}^{\mathrm{eh}} = T_{8,4}^{\mathrm{eh}} = T_T^{\mathrm{eh}},$$

$$T_{3,11}^{\mathrm{ee}} = T_{8,11}^{\mathrm{ee}} = T_{11,4}^{\mathrm{ee}} = T_{11,9}^{\mathrm{ee}} = T^D.$$

Using Eq. (2), the nonzero proportionality coefficients for $M > 0$ then become

$$
\begin{aligned}
a_{1,1} &= -a_{1,2} = a_{2,2} = -a_{2,3} = a_{3,3} = a_{4,4} = -a_{4,5}\\
&= a_{5,5} = -a_{5,6} = a_{6,6} = -a_{6,7} = a_{7,7} = -a_{7,8}\\
&= a_{8,8} = a_{9,9} = -a_{9,10} = a_{10,10} = -a_{10,1} = \frac{e^2}{h},\\
a_{3,4} &= a_{8,9} = \frac{e^2}{h}\left(T_L^{\mathrm{eh}} - T_L^{\mathrm{ee}}\right),\\
a_{3,9} &= a_{8,4} = \frac{e^2}{h}\left(T_T^{\mathrm{eh}} - T_T^{\mathrm{ee}}\right),\\
a_{11,11} &= \frac{2e^2}{h}T^D,\\
a_{3,11} &= a_{8,11} = a_{11,4} = a_{11,9} = -\frac{e^2}{h}T^D.
\end{aligned}
$$

Note that contact 11 acts as both a metallic drain (through T^D) and as a SC "scattering" object allowing electrons coming from contacts 4 and 9 to be transported via the CAR or CT processes to contacts 3 and 8 (through T_L^{eh}, T_L^{ee}, T_T^{eh}, and T_T^{ee}).

2. Longitudinal and transverse resistance

Next, Eq. (1) is solved (with the summation running over all 11 contacts) with $V_{\mathrm{SC}} = V_{11}$ and

$$I_2 = I_3 = I_4 = I_5 = I_7 = I_8 = I_9 = I_{10} = 0, \tag{A1}$$

$$I_1 + I_6 + I_{11} + I_{11}^{\mathrm{SC}} = 0, \tag{A2}$$

where I_{11} is the single-particle current and I_{11}^{SC} is the supercurrent flowing into the device from contact 11. This yields the expressions for the longitudinal and transverse resistance:

$$R_{xx} = \frac{V_2 - V_3}{I_1} = \frac{V_4 - V_5}{-I_6} = \frac{V_8 - V_9}{-I_6} = \frac{V_{10} - V_9}{I_1} = 0, \tag{A3}$$

$$R_{yx} = \frac{V_{10} - V_2}{I_1} = \frac{V_9 - V_3}{I_1} = \frac{V_8 - V_4}{-I_6} = \frac{V_7 - V_5}{-I_6} = \frac{h}{e^2}, \tag{A4}$$

as expected, regardless of whether the SC contact 11 is grounded or floating. The resistances measured across the SC strip ($R_{3\text{-}4}$ and $R_{9\text{-}8}$), on the other hand, do depend on whether (super)current is allowed to flow into the device through contact 11. These resistances are discussed for two different exprimental setups in the main text.

3. Non-ideal grounded contacts

For the measurements shown in Figs. 2(e) and 2(f), the SC contact 11 and the normal metal contact 6 are both grounded (i.e., $V_{11} = V_6 = 0$). In the actual experiment, both contact 11 and 6 have a finite contact resistance $R_{\mathrm{c},i}$ to the QAHI thin film, which means that the potentials $V_{11} = -I_{11}R_{\mathrm{c},11}$ and $V_6 = -I_6 R_{\mathrm{c},6}$ at the sample side of the contact will not be equal and slightly higher than zero. This will cause a small current to flow from contacts 11 to contact 6, which was not taken into account in Eqs. (10)–(12).

In the absence of CAR/CT and the presence of 100% damping at the superconductor-QAHI interface, i.e., $T_L^{\mathrm{ee}} = T_T^{\mathrm{ee}} = T_T^{\mathrm{eh}} = 0$ and $T^D = 1$, we find:

$$I_6 = \frac{R_{\mathrm{c},11}}{R_{\mathrm{c},6} + h/e^2} I_{11}, \tag{A5}$$

which is a simple current divider.

The resistances for the grounded configuration then become

$$R_{3\text{-}4} = R_{8\text{-}4} = \frac{R_{\mathrm{c},11}}{1 + (R_{\mathrm{c},6} + R_{\mathrm{c},11})e^2/h} \approx R_{\mathrm{c},11}, \tag{A6}$$

$$R_{9\text{-}8} = \frac{h}{e^2}. \tag{A7}$$

Notice that $R_{3\text{-}4}$ and $R_{8\text{-}4}$ are positive and will possibly mask the negative resistances stemming from Andreev processes at the superconductor-QAHI interface.

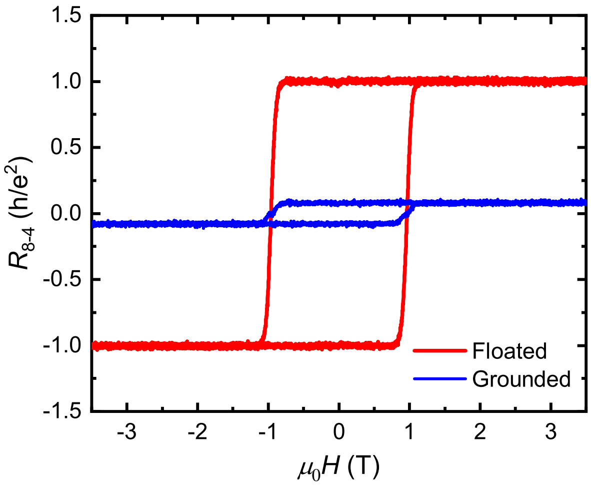

FIG. 5. The apparent transverse resistance $R_{8\text{-}4} = (V_8 - V_4)/I_1$ with $I_1 = 1$ nA, for the floating and grounded configuration. The nonzero $R_{8\text{-}4}$ in the grounded configuration corresponds to $I_6 \approx -80$ pA which stems from the finite contact resistances of contacts 6 and 11 [see Eq. (A6)].

Figure 5 shows $R_{8\text{-}4} = (V_8 - V_4)/I_1$ for the floating and grounded configuration. When the SC electrode is floating then $I_1 = -I_6$ and $R_{8\text{-}4} = h/e^2$ to-within the accuracy of our measurement. On the other hand, when the SC electrode is grounded, $R_{8\text{-}4}$ in Fig. 5 is nonzero. This corresponds to a current $I_6 \approx -80$ pA flowing on the right side of the Nb strip. Rather than claiming that $T_L^{\mathrm{ee}} > T_L^{\mathrm{eh}}$ [Eq. (12)], we attribute the nonzero $R_{8\text{-}4}$ to the presence of a finite contact resistance at the SC electrode 11, $R_{\mathrm{c},11}$ [see Eq. (A6)]. This is backed up by the fact that $R_{8\text{-}4}$ remains unchanged as the magnetic field is increased above the upper critical field of Nb, $H_{c2} = 2.7$ T [see inset of Figs. 2(c)].

Note that the effect of nonideal contacts for the grounded configuration in our experiment is large, as contacts 6 and 11 were grounded outside the dilution refrigerator (rather than on-chip). This means that in this case the "contact" resistance $R_{\mathrm{c},i}$ also includes the line and filter resistances. Equation (A6) gives a lower bound for $R_{\mathrm{c},11} > R_{8\text{-}4} \approx 2$ kΩ.

4. Does a thin insulating barrier between the superconductor and QAHI help?

In a recent publication [22], Huang *et al.* claimed that an AlO_x oxide barrier suppresses the single-particle current into the SC electrode ($T^D \approx 0$), whereas the SC proximity effect survives up to slightly higher barrier thicknesses. The observations of kinks at $\sigma_{2T} \approx 0.57{-}0.59\frac{e^2}{h}$ in the magnetic-field behavior of the two-terminal conductance measured across a Nb strip were interpreted as signatures of the $\mathcal{N}=1$ topological SC state [Eq. (6)]. In the supposed $\mathcal{N}=2$ topological SC state, on the other hand, the samples showed $\sigma_{2T} \approx 0.74\frac{e^2}{h}$ [Eq. (7)].

While Huang *et al.* suggested [22] that their observation of a kink in σ_{2T} supports the appearance of the chiral Majorana edge mode predicted by theory [5,21], the σ_{2T} values at the kink are only within 10–30% of the expected quantization. This was attributed to additional conduction channels and a remaining electric short through the Nb. Here, we examine whether these values can be reconciled with a high resistive short across the width of the Hall bar. We assume $T^D = 0$ to follow the claim of Ref. [22], and instead allow a fraction T^S of the current to flow between the opposing edges of the Hall bar through the Nb to consider the electric short assumed in Ref. [22]. The transmission coefficients for an electron to transmit as an electron between contacts 3, 4, 8, and 9 are then modified to:

$$T^{ee}_{3,9} = T^{ee}_{8,4} = T^{ee}_T + T^S,$$

and the new proportionality coefficients become

$$a_{3,9} = a_{8,4} = \frac{e^2}{h}\left(T^{eh}_T - T^{ee}_T - T^S\right), \tag{A8}$$

$$a_{11,11} = a_{3,11} = a_{8,11} = a_{11,4} = a_{11,9} = 0. \tag{A9}$$

Using the condition $T^{ee}_T = T^{eh}_T = T^{ee}_L = T^{eh}_L$ for the $\mathcal{N}=1$ topological SC state, and $T^{ee}_T = T^{eh}_T = T^{eh}_L = 0$ for the $N=2$ topological SC state, the expressions for the two-terminal conductance then become

$$\sigma_{2T} = (1 - T^S)\frac{e^2}{2h} \quad \text{for} \quad \mathcal{N}=1, \tag{A10}$$

$$= (1 - T^S)\frac{e^2}{h} \quad \text{for} \quad \mathcal{N}=2. \tag{A11}$$

Hence, if the $\mathcal{N}=2$ topological SC state (which is indistinguishable from the QAHI state) yields $\sim 0.74\frac{e^2}{h}$ [22], then we should search for a feature at $\sim 0.37\frac{e^2}{h}$ for the $\mathcal{N}=1$ topological SC state, as one would also intuitively expect. As a result, the kinks observed by Huang *et al.* at $0.57{-}0.59\frac{e^2}{h}$ are most likely not related to the $\mathcal{N}=1$ topological SC state, and furthermore, their study in Ref. [22] gives no evidence for induced superconductivity in a QAHI. Moreover, the magnetic-field dependencies of the two-terminal conductance reported in Ref. [22] show several kinks at different values of σ_{2T}, which suggests that the kinks at $0.57{-}0.59\frac{e^2}{h}$ are not special points. Such features are possibly caused by temperature effects [45] or inhomogeneous switching of the magnetization [46,47], affecting the longitudinal conductance of the QAHI film.

[1] R. Yu, W. Zhang, H.-J. Zhang, S.-C. Zhang, X. Dai, and Z. Fang, Quantized anomalous Hall effect in magnetic topological insulators, Science **329**, 61 (2010).

[2] C.-Z. Chang, J. Zhang, X. Feng, J. Shen, Z. Zhang, M. Guo, K. Li, Y. Ou, P. Wei, L.-L. Wang, Z.-Q. Ji, Y. Feng, S. Ji, X. Chen, J. Jia, X. Dai, Z. Fang, S.-C. Zhang, K. He, Y. Wang *et al.*, Experimental observation of the quantum anomalous Hall effect in a magnetic topological insulator, Science **340**, 167 (2013).

[3] C.-Z. Chang, W. Zhao, D. Y. Kim, H. Zhang, B. A. Assaf, D. Heiman, S.-C. Zhang, C. Liu, M. H. W. Chan, and J. S. Moodera, High-precision realization of robust quantum anomalous Hall state in a hard ferromagnetic topological insulator, Nat. Mater. **14**, 473 (2015).

[4] X.-L. Qi, T. L. Hughes, and S.-C. Zhang, Chiral topological superconductor from the quantum Hall state, Phys. Rev. B **82**, 184516 (2010).

[5] J. Wang, Q. Zhou, B. Lian, and S.-C. Zhang, Chiral topological superconductor and half-integer conductance plateau from quantum anomalous Hall plateau transition, Phys. Rev. B **92**, 064520 (2015).

[6] C. W. J. Beenakker, P. Baireuther, Y. Herasymenko, I. Adagideli, L. Wang, and A. R. Akhmerov, Deterministic creation and braiding of chiral edge vortices, Phys. Rev. Lett. **122**, 146803 (2019).

[7] C. J. Beenakker, A. Grabsch, and Y. Herasymenko, Electrical detection of the Majorana fusion rule for chiral edge vortices in a topological superconductor, SciPost Phys. **6**, 022 (2019).

[8] I. Adagideli, F. Hassler, A. Grabsch, M. Pacholski, and C. W. J. Beenakker, Time-resolved electrical detection of chiral edge vortex braiding, SciPost Phys. **8**, 013 (2020).

[9] C.-Z. Chen, Y.-M. Xie, J. Liu, P. A. Lee, and K. T. Law, Quasi-one-dimensional quantum anomalous Hall systems as new platforms for scalable topological quantum computation, Phys. Rev. B **97**, 104504 (2018).

[10] J. Legendre, E. Zsurka, D. Di Miceli, L. Serra, K. Moors, and T. L. Schmidt, Topological properties of finite-size heterostructures of magnetic topological insulators and superconductors, Phys. Rev. B **110**, 075426 (2024).

[11] D. J. Clarke, J. Alicea, and K. Shtengel, Exotic circuit elements from zero-modes in hybrid superconductor–quantum-Hall systems, Nat. Phys. **10**, 877 (2014).

[12] G.-H. Lee, K.-F. Huang, D. K. Efetov, D. S. Wei, S. Hart, T. Taniguchi, K. Watanabe, A. Yacoby, and P. Kim, Inducing superconducting correlation in quantum Hall edge states, Nat. Phys. **13**, 693 (2017).

[13] M. Kayyalha, D. Xiao, R. Zhang, J. Shin, J. Jiang, F. Wang, Y.-F. Zhao, R. Xiao, L. Zhang, K. M. Fijalkowski, P. Mandal, M. Winnerlein, C. Gould, Q. Li, L. W. Molenkamp, M. H. W. Chan, N. Samarth, and C.-Z. Chang, Absence of evidence for chiral Majorana modes in quantum anomalous Hall-superconductor devices, Science **367**, 64 (2020).

[14] J. Shen, J. Lyu, J. Z. Gao, Y.-M. Xie, C.-Z. Chen, C.-w. Cho, O. Atanov, Z. Chen, K. Liu, Y. J. Hu, K. Y. Yip, S. K. Goh, Q. L. He, L. Pan, K. L. Wang, K. T. Law, and R. Lortz, Spectroscopic fingerprint of chiral Majorana modes at the edge of a quantum anomalous Hall insulator/superconductor heterostructure, Proc. Natl. Acad. Sci. USA **117**, 238 (2020).

[15] O. Atanov, W. T. Tai, Y.-M. Xie, Y. H. Ng, M. A. Hammond, T. S. Manfred Ho, T. H. Koo, H. Li, S. L. Ho, J. Lyu, S. Chong, P. Zhang, L. Tai, J. Wang, K. T. Law, K. L. Wang, and R. Lortz, Proximity-induced quasi-one-dimensional superconducting quantum anomalous Hall state, Cell Rep. Phys. Sci. **5**, 101762 (2024).

[16] A. Uday, G. Lippertz, K. Moors, H. F. Legg, R. Joris, A. Bliesener, L. M. C. Pereira, A. A. Taskin, and Y. Ando, Induced superconducting correlations in a quantum anomalous Hall insulator, Nat. Phys. **20**, 1589 (2024).

[17] L. Fu and C. L. Kane, Probing neutral Majorana fermion edge modes with charge transport, Phys. Rev. Lett. **102**, 216403 (2009).

[18] A. R. Akhmerov, J. Nilsson, and C. W. J. Beenakker, Electrically detected interferometry of Majorana fermions in a topological insulator, Phys. Rev. Lett. **102**, 216404 (2009).

[19] L. Zhao, E. G. Arnault, A. Bondarev, A. Seredinski, T. F. Q. Larson, H. Draelos, A. W. Li, K. Watanabe, T. Taniguchi, F. Amet, H. U. Baranger, and G. Finkelstein, Interference of chiral Andreev edge states, Nat. Phys. **16**, 862 (2020).

[20] M. Hatefipour, J. J. Cuozzo, J. Kanter, W. M. Strickland, C. R. Allemang, T.-M. Lu, E. Rossi, and J. Shabani, Induced superconducting pairing in integer quantum Hall edge states, Nano Lett. **22**, 6173 (2022).

[21] S. B. Chung, X.-L. Qi, J. Maciejko, and S.-C. Zhang, Conductance and noise signatures of Majorana backscattering, Phys. Rev. B **83**, 100512(R) (2011).

[22] Y. Huang, Y. Fu, P. Zhang, K. L. Wang, and Q. L. He, Inducing superconductivity in quantum anomalous Hall regime, J. Phys.: Condens. Matter **36**, 37LT01 (2024).

[23] C.-Z. Chen, J. J. He, D.-H. Xu, and K. T. Law, Effects of domain walls in quantum anomalous Hall insulator/superconductor heterostructures, Phys. Rev. B **96**, 041118(R) (2017).

[24] W. Ji and X.-G. Wen, $\frac{1}{2}(e^2/h)$ conductance plateau without 1D chiral Majorana fermions, Phys. Rev. Lett. **120**, 107002 (2018).

[25] Y. Huang, F. Setiawan, and J. D. Sau, Disorder-induced half-integer quantized conductance plateau in quantum anomalous Hall insulator-superconductor structures, Phys. Rev. B **97**, 100501(R) (2018).

[26] B. Lian, J. Wang, X.-Q. Sun, A. Vaezi, and S.-C. Zhang, Quantum phase transition of chiral Majorana fermions in the presence of disorder, Phys. Rev. B **97**, 125408 (2018).

[27] S. Datta, in *Electronic Transport in Mesoscopic Systems*, Cambridge Studies in Semiconductor Physics and Microelectronic Engineering (Cambridge University Press, Cambridge, England, 1995).

[28] C. J. Lambert and R. Raimondi, Phase-coherent transport in hybrid superconducting nanostructures, J. Phys.: Condens. Matter **10**, 901 (1998).

[29] G. Lippertz, A. Bliesener, A. Uday, L. M. C. Pereira, A. A. Taskin, and Y. Ando, Current-induced breakdown of the quantum anomalous Hall effect, Phys. Rev. B **106**, 045419 (2022).

[30] I. Protopopov, Y. Gefen, and A. Mirlin, Transport in a disordered $\nu = 2/3$ fractional quantum Hall junction, Ann. Phys. **385**, 287 (2017).

[31] C. Nosiglia, J. Park, B. Rosenow, and Y. Gefen, Incoherent transport on the $\nu = 2/3$ quantum Hall edge, Phys. Rev. B **98**, 115408 (2018).

[32] S. Manna, A. Das, Y. Gefen, and M. Goldstein, Shot noise as a diagnostic in the $\nu = 2/3$ fractional quantum Hall edge zoo, Low Temp. Phys. **50**, 1113 (2024).

[33] S. Manna, A. Das, Y. Gefen, and M. Goldstein, Diagnostics of anomalous conductance plateaus in abelian quantum Hall regime, arXiv:2307.05173.

[34] P. Pandey, S. Manna, K. N. Frei, J. Saji, A. Denis, A. Savin, K. Watanabe, T. Taniguchi, P. J. Hakonen, A. Das, and M. Kumar, Half-quantized Hall plateaus in the confined geometry of graphene, arXiv:2410.03896.

[35] J. Nakamura, S. Liang, G. C. Gardner, and M. J. Manfra, Half-integer conductance plateau at the $\nu = 2/3$ fractional quantum Hall state in a quantum point contact, Phys. Rev. Lett. **130**, 076205 (2023).

[36] M. H. Fauzi, K. Nakagawara, K. Hashimoto, N. Shibata, and Y. Hirayama, Synthesizing $2h/e^2$ resistance plateau at the first Landau level confined in a quantum point contact, Commun. Phys. **6**, 365 (2023).

[37] O. Gül, Y. Ronen, S. Y. Lee, H. Shapourian, J. Zauberman, Y. H. Lee, K. Watanabe, T. Taniguchi, A. Vishwanath, A. Yacoby, and P. Kim, Andreev reflection in the fractional quantum Hall state, Phys. Rev. X **12**, 021057 (2022).

[38] E. J. Fox, I. T. Rosen, Y. Yang, G. R. Jones, R. E. Elmquist, X. Kou, L. Pan, K. L. Wang, and D. Goldhaber-Gordon, Part-per-million quantization and current-induced breakdown of the quantum anomalous Hall effect, Phys. Rev. B **98**, 075145 (2018).

[39] M. Kawamura, R. Yoshimi, A. Tsukazaki, K. S. Takahashi, M. Kawasaki, and Y. Tokura, Current-driven instability of the quantum anomalous Hall effect in ferromagnetic topological insulators, Phys. Rev. Lett. **119**, 016803 (2017).

[40] G. Qiu, P. Zhang, P. Deng, S. K. Chong, L. Tai, C. Eckberg, and K. L. Wang, Mesoscopic transport of quantum anomalous Hall effect in the submicron size regime, Phys. Rev. Lett. **128**, 217704 (2022).

[41] L.-J. Zhou, R. Mei, Y.-F. Zhao, R. Zhang, D. Zhuo, Z.-J. Yan, W. Yuan, M. Kayyalha, M. H. W. Chan, C.-X. Liu, and C.-Z. Chang, Confinement-induced chiral edge channel interaction in quantum anomalous Hall insulators, Phys. Rev. Lett. **130**, 086201 (2023).

[42] K. M. Fijalkowski, N. Liu, M. Klement, S. Schreyeck, K. Brunner, C. Gould, and L. W. Molenkamp, A balanced quantum Hall resistor, Nat. Electron. **7**, 438 (2024).

[43] T. Röper, H. Thomas, D. Rosenbach, A. Uday, G. Lippertz, A. Denis, P. Morfin, A. A. Taskin, Y. Ando, and E. Bocquillon, Propagation, dissipation, and breakdown in quantum anomalous Hall edge states probed by microwave edge plasmons, Phys. Rev. B **110**, L161403 (2024).

[44] A. Uday, G. Lippertz, B. Bhujel, A. A. Taskin, and Y. Ando, Non-Majorana-origin of the half-integer conductance quantization elucidated by multi-terminal superconductor-quantum anomalous Hall insulator heterostructure (2024), doi: https://zenodo.org/records/14176676.

[45] A. J. Bestwick, E. J. Fox, X. Kou, L. Pan, K. L. Wang, and D. Goldhaber-Gordon, Precise quantization of the anomalous Hall effect near zero magnetic field, Phys. Rev. Lett. **114**, 187201 (2015).

[46] E. O. Lachman, A. F. Young, A. Richardella, J. Cuppens, H. R. Naren, Y. Anahory, A. Y. Meltzer, A. Kandala, S. Kempinger, Y. Myasoedov, M. E. Huber, N. Samarth, and E. Zeldov, Visualization of superparamagnetic dynamics in magnetic topological insulators, Sci. Adv. **1**, e1500740 (2015).

[47] E. O. Lachman, M. Mogi, J. Sarkar, A. Uri, K. Bagani, Y. Anahory, Y. Myasoedov, M. E. Huber, A. Tsukazaki, M. Kawasaki, T. Yoshinori, and E. Zeldov, Observation of superparamagnetism in coexistence with quantum anomalous Hall $C = \pm 1$ and $C = 0$ Chern states, npj Quantum Mater. **2**, 70 (2017).

Chapter 4

Conclusion

In this thesis, the superconducting proximity effect was investigated in V-doped $(Bi_xSb_{1-x})_2Te_3$ thin films displaying the quantum anomalous Hall effect. When an s-wave SC is placed on top of such a QAHI thin film, the metallization effect causes the chemical potential in the QAHI to move out of the magnetic gap opened at the Dirac point of the 2D surface states. This results in the region of the QAHI thin film in contact with the SC to become metallic, whereas the rest of the QAHI film remains insulating in the 3D bulk as well as the 2D surface. In this thesis, it was shown using KWANT simulations that this doping by the superconducting electrode is beneficial for the superconducting proximity effect, causing the metallic regions of the QAHI underneath the SC to become proximitized. In such a heterostructure the inversion symmetry is broken between the top and bottom surface of the QAHI, as the top surface is in direct contact with the SC. In this case, the induced superconducting phase is predicted to be a topological superconductor with Chern number $\mathcal{N} = 1$, associated with a single chiral Majorana mode at the edge of the proximitized QAHI region. These chiral Majorana edge modes are of great interest as the creation of a π-phase domain boundary in these edge-modes is predicted to lead to mobile non-Abelian zero modes, which could transfer quantum information between stationary topological qubits (see chapter 5). As a result, the experimental realization of induced superconducting correlations in a QAHI will greatly contribute to a better understanding of topological superconductivity and Majorana physics, as well as provide a additional platform to develop topological quantum computation. Two experiments were presented in this thesis to study the magneto-transport features of the superconducting proximity effect in QAHI devices.

The main highlight of this thesis is the first experiment which demonstrated the successful observation of crossed Andreev reflection (CAR) across a superconducting Nb electrode contacting one edge channel of the QAHI. This is the first compelling evidence for induced superconducting pair correlation in the chiral edge state of the QAHI. In the CAR process, an electron in the chiral edge state, arriving at a grounded superconducting electrode with an energy eV smaller than the superconducting gap Δ, is converted into a hole in the chiral edge state leaving from the SC, carrying a potential of $-V$. During this conversion, a Cooper pair is formed in the grounded SC. The negative potential of the downstream edge channel leaving from the SC, is recorded as a negative nonlocal resistance with respect to the SC. For this experiment, narrow superconducting electrodes of Nb with widths ranging from 160 to 520 nm were fabricated on top of multi-terminal Hall-bar devices consisting of V-doped $(Bi_xSb_{1-x})_2Te_3$ thin films. A negative downstream resistance contribution of $\Delta R_\mathrm{D} = -400\ \Omega$ was observed for the narrowest superconducting electrode (Fig. 2.1). This is about 3% of the maximum negative downstream resistance $-h/2e^2$ derived from a Landauer-Büttiker analysis of the experimental set-up. With increasing width of the Nb electrode, the value of ΔR_D decreases exponentially with a characteristic length of $\sim$100 nm (Fig. 2.3). This length scale is much larger than the superconducting coherence length of Nb in the dirty limit $\xi_\mathrm{Nb} \approx 30$ nm. This means that the Nb superconducting electrode itself cannot mediate the CAR process. Instead, we interpret the long characteristic length scale observed for the CAR process as evidence for a proximitized QAHI surface state underneath the Nb electrode which can mediate the CAR process over a much longer length scale due to its smaller induced superconducting gap ($\Delta_\mathrm{ind} \approx 0.04$ meV). This ability to proximitize the surface states of a QAHI constitutes an important advancement for the community as it finally opens up the SC-QAHI platform for Majorana research. In the outlook (chapter 5), two proposal for future experiments will be discussed based on these concepts.

The second experiment in this thesis addressed the half-integer two-terminal conductance of $e^2/(2h)$ observed in SC-QAHI heterostructures. Until now, the Landauer-Büttiker analysis of such a heterostructure in literature neglected to consider equilibration mechanisms between the chiral 1D edge states and the SC, like through the formation of chiral Andreev edge states (CAESs) or a single-particle current into the SC via subgap states. By formulating a Landauer-Büttiker model which *does* take into account edge state equilibration, it was shown in chapter 3 that the $e^2/(2h)$ conductance is *not* a feature unique to Majorana edge transport (Eqs. 3.6-3.7) and its experimental pursuit is ill-conceived. In addition, experiments were performed on multi-terminal devices made of V-doped $(Bi_xSb_{1-x})_2Te_3$ thin films proximitized by a Nb superconducting electrode to determine the potentials of all the chiral edge states in the system. The current flowed from left to right through the QAHI thin film and the SC lying across the middle of the QAHI film was electrically floating. The four-terminal resistance measured across the superconducting electrode was always h/e^2, which is equivalent to a two-terminal conductance of $e^2/(2h)$ for this set-up. Since the four-terminal resistance remained h/e^2 even when the external magnetic field was increased above the upper critical field of Nb or when the QAHI film underneath the SC was interrupted by a gap, it is clear that chiral Majorana edge states do *not* lie at the origin of the $e^2/(2h)$ conductance. Instead, the chiral edge states arriving at the SC, one at the potential of the source V_S and the other at the potential of the drain V_D, fully equilibrate with the floating SC such that $V_\mathrm{SC} = (V_\mathrm{S} + V_\mathrm{D})/2$. Since for μm-size superconducting electrodes on top of a QAHI the edge states fully equilibrate, the downstream resistance measured with respect to the SC will always be zero ($R_\mathrm{D} = 0$). Combining the insights from the two studies presented in this thesis on narrow and wide superconducting electrodes, it was demonstrated that signatures of the superconducting proximity effect in proximitized QAHI films are observable only within the length scale of the superconducting coherence length.

Chapter 5

Outlook

It has been demonstrated in this thesis that superconducting correlations can be induced in SC-QAHI heterostructures. Below, a few experiments are discussed that aim to confirm the presence of topological superconductivity, explore the associated Majorana physics, and investigate non-abelian zero modes in such systems.

CAR without Extrinsic Contact Resistance

In chapter 2, it was shown that when the width of the SC is comparable to the superconducting coherence length ξ_{S} then CAR can give rise to a negative downstream resistance, while chapter 3 has shown that a large (μm-size) SC electrode essentially acts as a good metal contact. Combining these two findings of this thesis, a better device design is proposed to study the CAR (and CT) in a QAHI, shown in Fig. 5.1a for an upward out-of-plane magnetization. In this device structure a SC strip lies across the QAHI Hall-bar, but its width is not constant. On the top edge of the QAHI, the superconducting electrode is wide ($W \gg \xi_{\mathrm{S}}$) and the SC acts as a good metal contact:

$$T^{\mathrm{ee}}_{2,7} = T^{\mathrm{ee}}_{7,3} = T^{\mathrm{D}}, \quad T^{\mathrm{ee}}_{2,3} = T^{\mathrm{eh}}_{2,3}, \quad T^{\mathrm{ee}}_{2,6} = T^{\mathrm{eh}}_{2,6}, \quad T^{\mathrm{ee}}_{5,3} = T^{\mathrm{eh}}_{5,3}.$$

Here, T^{D} and $T^{\mathrm{ee}}_{ij} = T^{\mathrm{eh}}_{ij}$ describe single electrons entering the SC electrode with an energy smaller than the SC gap though subgap states and fully equilibrated CAESs, respectively.

The superconducting electrode narrows down to a width comparable to the superconducting coherence length ($W \approx \xi_{\mathrm{S}}$) at the bottom edge of the QAHI. As a result, the only relevant processes for the narrow section of the superconducting electrode are CAR ($T^{\mathrm{eh}}_{5,6} = T^{\mathrm{CAR}}$), CT ($T^{\mathrm{ee}}_{5,6} = T^{\mathrm{CT}}$), and the single-particle current into the SC ($T^{\mathrm{ee}}_{5,7} = T^{\mathrm{ee}}_{7,6} = T^{\mathrm{D}}$). For a floating superconducting electrode ($I_1 = -I_4$) with $V_4 = 0$, the Landauer-Büttiker (LB) formalism [86, 87] at zero temperature then yields the expression for the potential of the SC:

$$V_{\mathrm{SC}} = V_7 = \frac{1 - T^{\mathrm{CT}} + T^{\mathrm{CAR}}}{2 - T^{\mathrm{CT}} + T^{\mathrm{CAR}}} V_1. \tag{5.1}$$

Notice that when $T^{\mathrm{CT}} \approx T^{\mathrm{CAR}}$, $V_{\mathrm{SC}} \approx V_1/2$ as was the case for the fully equilibrated edge states in chapter 3.

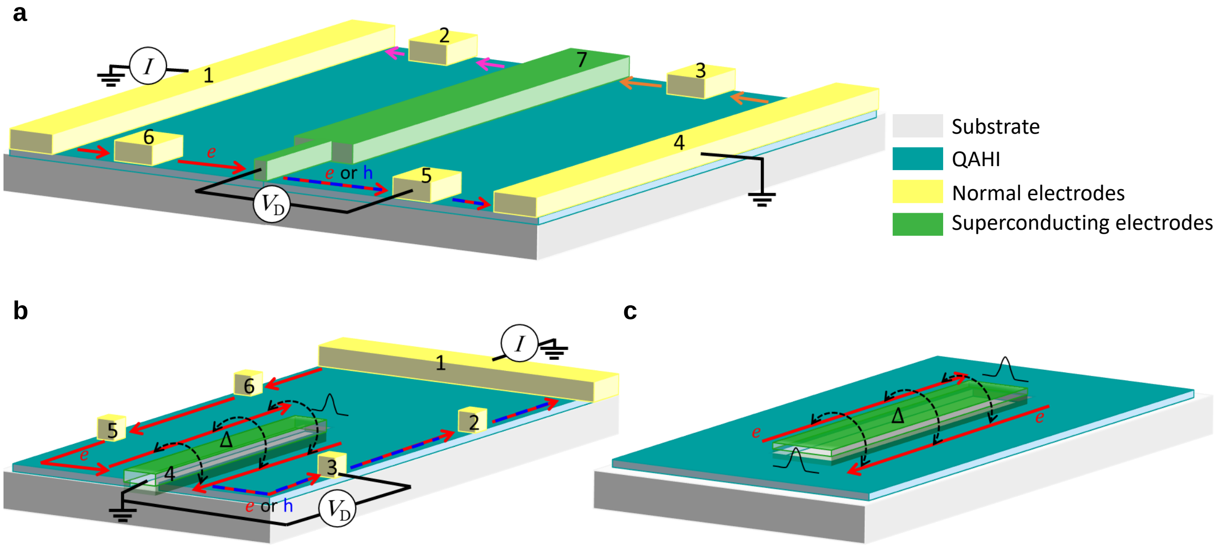

Fig. 5.1 | Proposals for future CAR experiments on a QAHI. In all the panels the 1D chiral edge channel runs in the anti-clockwise direction for an upward out-of-plane magnetization. **a**, Schematic of a multi-terminal Hall-bar device on a QAHI thin film with a superconducting electrode lying across the middle of the device. In the four-terminal set-up, the normal electrodes 1 and 4 are the source and drain, respectively, and the downstream voltage (V_{D}) is measured between the normal electrode 5 and the superconducting electrode 7. An incoming electron e continues in the downstream channel as an e or h depending on whether CT or CAR takes place across the narrow section of the superconducting electrode. **b**, Schematic of a Hall-bar, where a trench is etched in the QAHI thin film before depositing the superconducting electrode 4. The downstream voltage V_{D} is measured between electrode 3 and the grounded electrode 4. Depending on whether CT or CAR takes place, an electron arriving at the SC is converted into an electron or hole in the downstream channel, respectively. Note that due to the presence of a trench below the SC both the CT and CAR processes are now mediated by the parent superconductor. In this device structure, two Majorana zero modes are created: one in resonance with the chiral edge state and the other at the end of the trench. **c**, Schematic of an 'inverted nanowire' structure, in which the trench is moved to the middle of the QAHI thin film and filled with a SC. The two counter-propagating 1D chiral edge channels are coupled through the SC via the CAR process, creating two non-abelian Majorana zero modes at the ends of the trench. Note that the superconducting gap (Δ) is associated with the parent SC in both panel b and c.

For this asymmetric device design, the intrinsic downstream resistance is given by:

$$R_{\mathrm{D}}^{\mathrm{i}} = \frac{V_5 - V_7}{I_1} = \frac{h}{e^2}(T^{\mathrm{CT}} - T^{\mathrm{CAR}}), \tag{5.2}$$

which is negative if $T^{\mathrm{CAR}} > T^{\mathrm{CT}}$. Moreover, when $T^{\mathrm{CAR}} = 1$ (and hence $T^{\mathrm{CT}} = 0$), then one obtains the maximum negative value for $R_{\mathrm{D}}^{\mathrm{i}}$ of $-h/e^2$. This is twice the maximum negative downstream resistance value of $-h/(2e^2)$ derived for the set-ups in chapter 2 and 3! Note that the transverse resistance $R_{\mathrm{yx}} = (V_6 - V_2)/I_1 = (V_6 - V_2)/I_1$ is quantized to h/e^2, independent of the size of T^{CT}, T^{CAR}, and T^{D}.

This experimental set-up has two additional advantages: Firstly, the SC is not grounded as in chapter 2 and Refs. [20, 70, 72, 74]. In the four-terminal measurement scheme shown in Fig. 5.1a, $R_{\mathrm{D}} = R_{\mathrm{D}}^{\mathrm{i}}$ in the superconducting state, which means that there is no extrinsic contact resistance contribution that could possibly mask the negative nonlocal resistance contribution from CAR across the narrow SC section. Secondly, the positive longitudinal resistance contribution due to the breakdown of the QAHE is minimized in this set-up. The breakdown effect in a QAHI is large when two chiral edge states with different potentials are separated by a small distance [53], e.g. in narrow QAHI ribbons. However, since the superconducting electrode only needs to have a width of $\sim$100 nm at the bottom edge of the QAHI, the Hall-bar can be very wide (>100 μm) without running into fabrication issues.[1] This ensures that for small excitation currents the breakdown effect will most-likely be absent in this device design.

Majorana Zero Modes in SC-QAHI Heterostructures

In Fig. 5.1b, the device design resembles the devices investigated in chapter 2, with a key distinction: a trench is etched in the QAHI film and subsequently filled with the SC. In this set-up, the 2D surface of the QAHI is not proximitized as there is no film underneath the superconducting electrode, making it a fundamentally different system. When the width of the trench is comparable to the coherence length of the SC, the two counter-propagating edge channels along the trench boundaries can couple via CAR mediated by the SC. This hybrid structure is predicted to give rise to 1D topological superconductivity, hosting a pair of Majorana zero modes in the absence of an external magnetic field: one localized at the end of the trench and the other in resonance with the 1D chiral edge state [19]. Experimentally, the presence of CAR can be verified by measuring a negative downstream resistance $R_{\mathrm{D}} \equiv V_{\mathrm{D}}/I$ with respect to the grounded SC. These experiments might potentially benefit from choosing a SC with a longer coherence length than Nb, for instance Al. However, it is important to keep in mind that the low critical magnetic field of Al ($\sim$10 mT), combined with the magneto-caloric effect observed around 0 T in magnetically-doped QAHIs [6], may pose challenges for the analysis of the magnetic-field dependence of R_{D}. On the other hand, if one manages to make the trench narrow enough, then Nb can still be employed as the superconductor, having the benefit of a larger superconducting gap and higher upper critical field.

[1] It would be extremely challenging to fabricate a continues $\sim$100-nm-wide SC electrode across the full width of a 100-μm-wide Hall-bar.

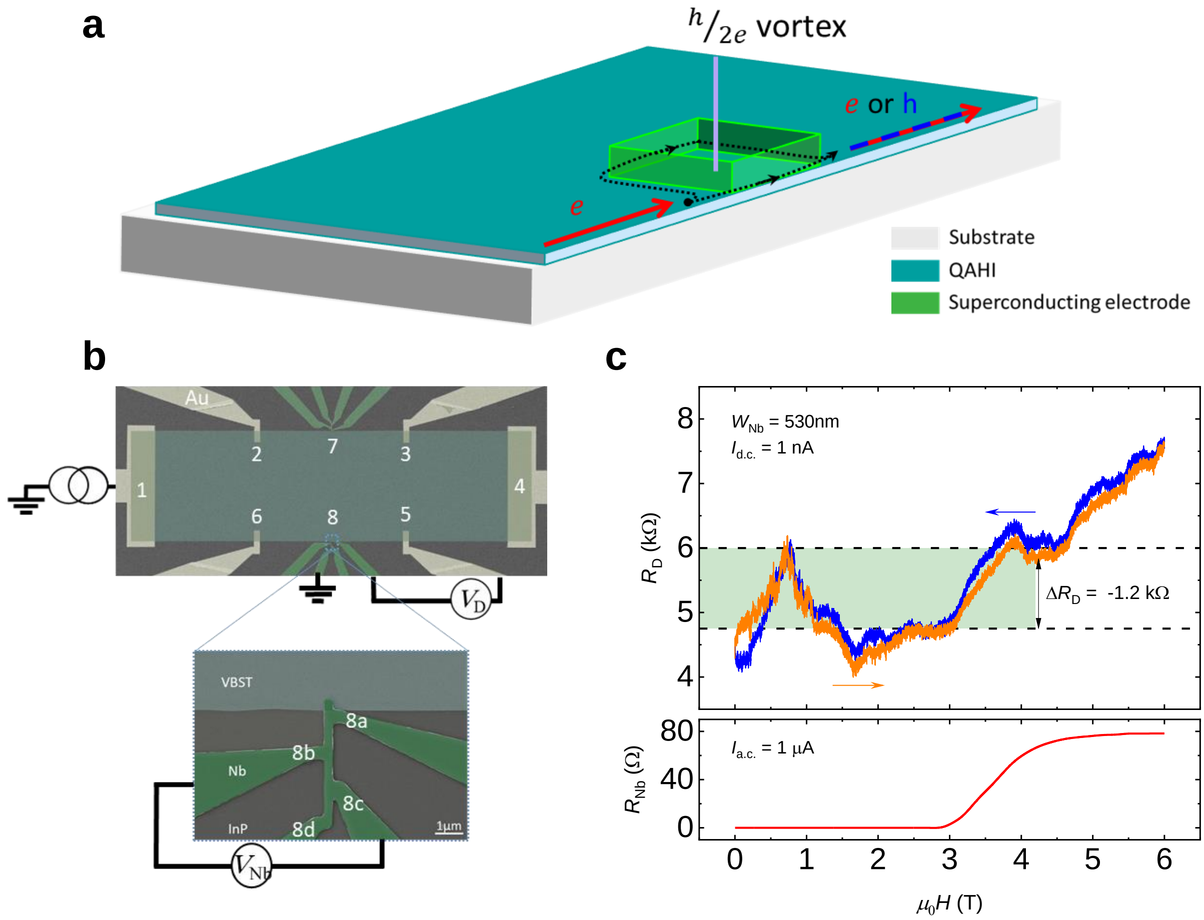

Fig. 5.2 | Majorana interference device on a QAHI. **a**, Schematic of a short superconducting electrode contacting one edge of the QAHI. An incoming electron splits into two chiral Majorana edge modes (CMEMs) moving around the grounded superconducting island, as represented by the black dotted lines. The two CMEMs will recombine on the other side of the SC as an electron or hole depending on the number of vortices (even or odd) enclosed by the two paths. A single vortex is shown in purple, contributing the superconducting flux quantum of $h/2e$. **b**, False-colour scanning electron microscopy image of a real device based on panel a, including the measurement set-up. The V-doped $(Bi_xSb_{1\text{-}x})_2Te_3$ (VBST) thin film (cyan) is contacted by normal (yellow) and superconducting (green) electrodes made of Pt/Au and Nb, respectively. The magnified image of the short superconducting Nb electrode is shown in the bottom of panel b. The downstream voltage (V_D) is measured between contacts 5 and 8a for an upward and out-of-plane magnetization where the 1D chiral edge state propagates anticlockwise along the sample edge. Notice that the superconducting Nb is measured between contacts 8b and 8c, independent from the sample. **c**, Magnetic-field dependence of $R_D \equiv V_D/I_{d.c.}$ and R_{Nb} shown for a Nb electrode of width $W_{Nb} = 530$ nm. The forward (orange) and backward (blue) magnetic-field-sweep are measured at 25 mK with $I_{d.c.} = 1$nA. The change in R_D when the SC in normal and superconducting state is highlighted by the green shaded region.

When CAR is observed in the device structure shown in Fig. 5.1b, it is reasonable to conclude that the 1D topological superconductivity state is realized. The associated Majorana zero mode at the end of the trench can then be detected by locally fabricating a tunnel probe (not shown in Fig. 5.1b). This platform can be further modified to create an 'inverted nanowire' with two localized Majorana zero modes, when the trench side-contacted by the SC is fabricated in the middle of the QAHI, see Fig. 5.1c. Note that this inverted nanowire might suffer less from disorder as compared to other Majorana nanowire platforms, which would help in distinguishing the Majorana zero modes from Andreev bound states.

Majorana Interference for Short Superconducting Electrodes

Another natural extension of the results presented in chapter 2, is to verify whether the proximitized QAHI region underneath the superconducting electrode is topological or not. The schematic shown in Fig. 5.2a is based on a proposal from Beenakker [26], which involves a short superconducting electrode that covers only one edge of the QAHI. If the $\mathcal{N} = 1$ topological superconductor phase is realized in the proximitized region of the QAHI, then an electron arriving at the grounded superconducting electrode will split into two chiral Majorana edge modes (CMEMs) that take two different paths around the SC. These CMEMs recombine on the other side of the SC as an electron or hole depending on whether the two paths enclose an even or odd number of superconducting vortices, respectively. In particular, the CMEMs accumulate a relative phase difference of π every time they cross the branch cut of a vortex in the SC. The charge neutral Majorana fermions can then be electrically detected through their interference upon recombination in the downstream edge state of the QAHI.

Figure 5.2b shows an image of a real device fabricated in the course of this thesis, where a 530-nm-wide superconducting Nb electrode is contacting a V-doped $((\mathrm{Bi_xSb_{1\text{-}x}})_2\mathrm{Te_3}$ thin film. The same fabrication recipe was used as for the devices investigated in chapter 2. The preliminary data for the downstream resistance $R_\mathrm{D} \equiv V_\mathrm{D}/I_\mathrm{d.c.}$ for an upward out-of-plane magnetization with $I_\mathrm{d.c.} = 1$ nA is shown in Fig. 5.2c. The magnetic field response of R_D shows several features as the Nb turns superconducting (below $\sim$3 T). The forward and backward sweeps follow the same path suggesting that the peaks and dips are real and not random fluctuations. Note that in chapter 2 CAR was not observed for device E with the widest Nb electrode ($W_\mathrm{Nb} = 520$ nm), see Figs. 2.3 and S7. As a result no CAR is expected for the device shown in Fig. 5.2b-c as well, yet the change in R_D from the normal to superconducting state is $\Delta R_\mathrm{D} \equiv -[R_\mathrm{D}(H > H_\mathrm{c2}) - R_\mathrm{D}(H < H_\mathrm{c2}) - R_\mathrm{Nb,InP}] \simeq -1.2$ kΩ, where $R_\mathrm{Nb,InP}$ is negligible for the 530-nm-wide Nb electrode. The observation of CAR in this device can possibly be explained by the superconducting electrode no longer acting as a good metallic drain, resulting in a larger fraction of the incoming electrons undergoing CAR (or CT) processes across the superconducting electrode.

Moreover, when Nb is superconducting the magnetic field response of R_D in Fig. 5.2c shows a peak and dip at $\sim$0.7 T and $\sim$1.7 T, respectively. A period of $\sim$2 T is too large to be related to Majorana interference in this device due to the formation of vortices, as for an overlap area of 530×800 nm^2 a vortex is injected about every $\sim$5 mT. Note that the size of L_Nb is difficult to determine and might be much smaller than $\sim$800 nm. Since

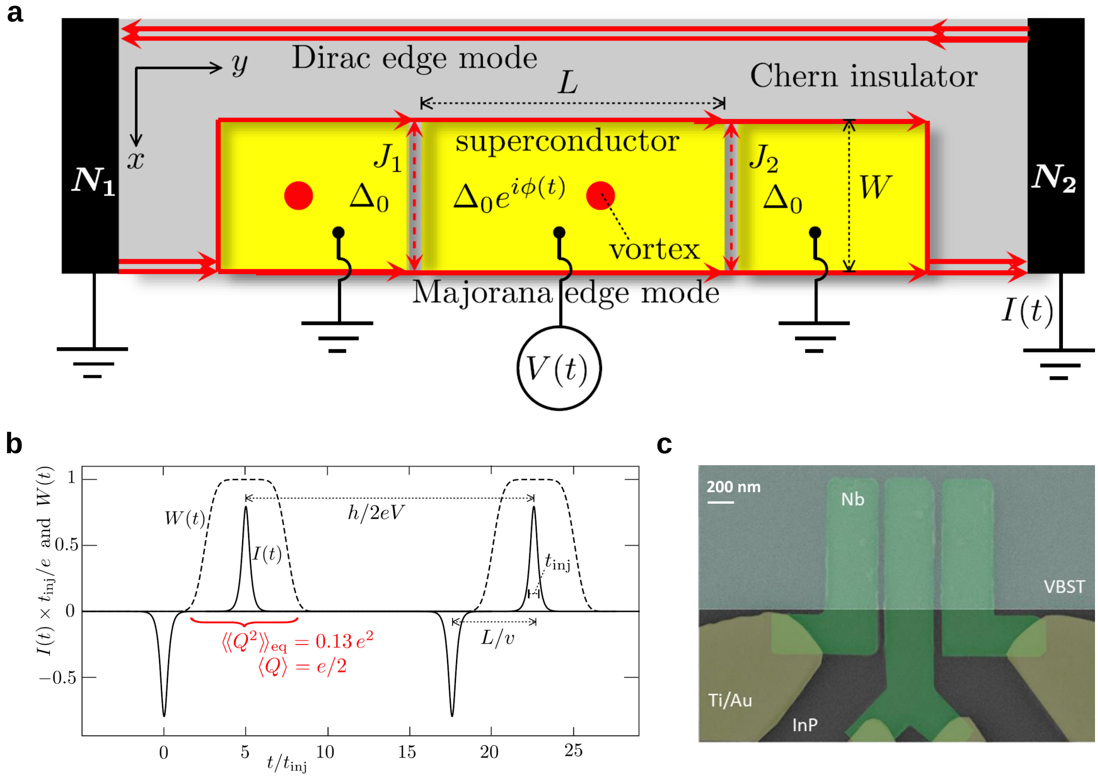

Fig. 5.3 | Injection of edge vortices in Josephson junctions on top of a QAHI. **a**, Proposed device design with two Josephson junctions (J_1 and J_2) and normal electrodes (N_1 and N_2). In response to a voltage pulse $V(t)$ applied to the middle superconducting electrode, a pair of edge vortices are injected at J_1 into the chiral Majorana edge channels at opposite boundaries of the SC. The edge vortices propagate along the respective chiral edge channels and fuse at J_2, resulting in a current pulse $I(t)$ flowing through N_2. The red dots represent bulk vortices. **b**, Charge fractionalization due to the formation of edge vortices for the same device design as in panel a, but in response to a constant voltage: $V(t) = V$ and in the absence of bulk vortices. In this set-up, the constant voltage bias V causes edge vortices to be continuously injected with a period of $h/(2eV)$. In the absence of bulk vortices, the fusion of the edge vortices results in two current pulses which integrate to an average charge of $\langle Q\rangle = -e/2$ and $+e/2$, separated by L/v with v the edge mode velocity. $W(t)$ represents the detection window for the second pulse. If bulk vortices are present, the peak shapes of $I(t)$ will change depending on the outcome of the braiding operations [15, 17]. **c**, False-colour scanning electron microscopy image of a device fabricated on V-doped $(Bi_xSb_{1-x})_2Te_3$ (VBST) with Nb electrodes in the course of this thesis based on panel a. The Josephson junction gaps are ~50 nm. Panels a and b are reprinted figures with permission from Refs. [16] and [18], respectively. © Copyright (2019-2020) by the American Physical Society.

a chemical wet-etching process is employed to etch the Hall-bar shape into the QAHI thin film, the first few hundred nms at the edge of film may be damaged by the acid creeping underneath the photoresist. This means that it is unclear where the 1D edge channel exactly flows with respect to the physical edge of the sample. The peak and dip in Fig. 5.2c could possibly be related to the formation of CAESs along the SC-QAHI interface, although one would also expect fluctuations over mT field ranges in this case [74,88]. Other effects that have yet to be considered are the Fabry-Pérot resonances when the Fermi wavelength k_F matches the Nb electrode dimensions [89,90], and the effect of the Meissner screening current in the SC in response to an external magnetic field [90]. Both effects were shown to greatly improve the tunnel-coupling between the chiral 1D edge states and the SC. However, so far the theoretical work on the SC-QAHI hybrid structure is scarce. Nevertheless, the observation of additional features in the magnetic field response of R_D, when Nb is in the superconducting state, warrants further investigation.

For the study of possible Majorana interference, one obvious modification is to include a hole in the superconducting electrode in the next device such that one can deterministically trap multiples of the superconducting flux quantum $h/(2e)$. Additionally, switching to a type-I SC (like Al), rather than Nb, would remove the additional flux stemming from vortices in the superconducting electrode. Lastly, by determining the length dependence of R_D, one may obtain a better understanding of the position of the 1D edge state with respect to the edge of the QAHI thin film, as well as the length-scale over which the edge state penetrates into the 2D bulk.

Josephson Junctions on a QAHI

Chiral Majorana edge modes in a topological superconductor still exhibit conventional fermionic exchange properties, while non-Abelian anyons are essential to enable "braiding" operations necessary for quantum computing applications. Theoretically, a biased Josephson junction fabricated on top of a QAHI has been proposed to be able to deterministically inject a pair of isolated vortices into the 1D chiral Majorana edge modes [15–18]. These "edge vortices" are π-phase domain boundaries which propagate along the chiral Majorana edge modes and carry with them a non-Abelian zero mode. Figure 5.3a shows the theoretically proposed device layout for the electrical detection of these edge vortices. The red arrows represent the 1D chiral Majorana edge modes and the red dots indicate localized bulk vortices in the SC. Upon the application of a voltage pulse $V(t)$ to the middle superconducting island which integrates to $\int V(t)dt = h/(2e)$, the superconducting phase difference across the Josephson junction J_1 is incremented with 2π and a pair of edge vortices are injected in the top an bottom chiral Majorana edge mode at J_1 in a state of even fermion parity. The two edge vortices, subsequently, fuse at the Josephson junction J_2 and depending on whether the fermion parity has changed from even to odd or not, may or may not leave behind an unpaired electron. Such a parity change occurs when one of the edge vortices crosses the branch cut of the phase winding around a bulk vortex (the red dot on the middle superconducting island in Fig. 5.3a). This constitutes a braiding operation between a pair of non-Abelian anyons: one immobile in a bulk vortex, the other mobile in an edge vortex [16]. The transferred charge $Q = \int I(t)dt$, measured at metal contact N_2, is quantized to $Q = e$ or zero, depending on whether the region between the Josephson junctions J_1 and J_1 contain an odd or even number of bulk vortices, respectively.

The shape of the current pulse $I(t)$ measured at N_2 can be quite complicated, as it depends on the relative magnitude of the path length difference between the upper and lower Majorana edge modes δL, the edge mode velocity v, and the duration of the vortex injection process t_{inj} [15, 17]. However, even in the absence of bulk vortices (and braiding), the dynamics of edge vortices can be investigated in the device layout shown in Fig. 5.3a. If a constant d.c. voltage is applied to the middle superconducting island $V(t) = V$, instead of a voltage pulse, then a periodic train of edge vortices are injected, separated by $\Delta t = h/(2eV)$, which upon fusion create two current pulses $I(t)$ separated by L/v, which integrate to an average charge of $\langle Q\rangle = -e/2$ and $+e/2$ [18], see Fig. 5.3b. Notice that these two pulses still sum to zero, as no change of the fermion parity takes place in the absence of immobile bulk vortices. The observation of this charge fractionalization phenomenon in the absence of bulk vortices would constitute the first milestone in the development of so-called "flying qubits" in this platform which combines two Josephson junctions fabricated on top of a QAHI.

Figure 5.3c shows a false-colour scanning electron microscopy image of two Nb Josephson junctions contacting a V-doped $(Bi_xSb_{1\text{-}x})_2Te_3$ thin film fabricated in the course of this thesis. Currently, the smallest junction gaps were $\sim$50 nm, but the Josephson junction did not enter the zero-resistance state yet. Efforts are being taken to further improve the interface quality and reduce the gap size. For a practical estimate of the time scales of these experiments, one can take $L \approx 430$ nm and $W \approx 1.2$ μm (from Fig. 5.3c), the induced supercondcuting coherence length $\xi_S \approx 100$ nm (from chapter 2), and the edge mode velocity $v \approx 4.5 \times 10^5$ m/s (from our publication [57]). This yields a period between edge vortex injection of $\Delta t = h/(2eV) \approx 2.1$ ps for 1 mV of d.c. bias, a pulse separation of $L/v \approx 0.9$ ps, and an edge vortex injection time of $t_{\text{inj}} = (\xi_S \Delta t)/(2\pi W) \approx 30$ fs [16, 18]. Hence, the magneto-transport experiments on edge vortices will be extremely challenging requiring THz data acquisition.

Bibliography

[1] KITAEV, A. Y. Fault-tolerant quantum computation by anyons. *Ann. Phys. 303*, 1 (2003), 2–30.

[2] VON KLITZING, K., DORDA, G., AND PEPPER, M. New method for high-accuracy determination of the fine-structure constant based on quantized Hall resistance. *Phys. Rev. Lett. 45* (1980), 494–497.

[3] HALDANE, F. D. M. Model for a quantum Hall effect without Landau levels: Condensed-matter realization of the "parity anomaly". *Phys. Rev. Lett. 61* (1988), 2015–2018.

[4] LIU, C.-X., QI, X.-L., DAI, X., FANG, Z., AND ZHANG, S.-C. Quantum anomalous Hall effect in $Hg_{1-y}Mn_yTe$ quantum wells. *Phys. Rev. Lett. 101* (2008), 146802.

[5] YU, R., ZHANG, W., ZHANG, H.-J., ZHANG, S.-C., DAI, X., AND FANG, Z. Quantized anomalous Hall effect in magnetic topological insulators. *Science 329*, 5987 (2010), 61–64.

[6] BESTWICK, A. J., FOX, E. J., KOU, X., PAN, L., WANG, K. L., AND GOLDHABER-GORDON, D. Precise quantization of the anomalous Hall effect near zero magnetic field. *Phys. Rev. Lett. 114* (2015), 187201.

[7] CHANG, C.-Z., ZHANG, J., FENG, X., SHEN, J., ZHANG, Z., GUO, M., LI, K., OU, Y., WEI, P., WANG, L.-L., JI, Z.-Q., FENG, Y., JI, S., CHEN, X., JIA, J., DAI, X., FANG, Z., ZHANG, S.-C., HE, K., WANG, Y., LU, L., MA, X.-C., AND XUE, Q.-K. Experimental observation of the quantum anomalous Hall effect in a magnetic topological insulator. *Science 340*, 6129 (2013), 167–170.

[8] CHANG, C.-Z., ZHAO, W., KIM, D. Y., ZHANG, H., ASSAF, B. A., HEIMAN, D., ZHANG, S.-C., LIU, C., CHAN, M. H. W., AND MOODERA, J. S. High-precision realization of robust quantum anomalous Hall state in a hard ferromagnetic topological insulator. *Nat. Mater. 14* (2015), 473–477.

[9] CHANG, C.-Z., ZHAO, W., KIM, D. Y., WEI, P., JAIN, J. K., LIU, C., CHAN, M. H. W., AND MOODERA, J. S. Zero-field dissipationless chiral edge transport and the nature of dissipation in the quantum anomalous Hall state. *Phys. Rev. Lett. 115* (2015), 057206.

[10] CHECKELSKY, J. G., YOSHIMI, R., TSUKAZAKI, A., TAKAHASHI, K. S., KOZUKA, Y., FALSON, J., KAWASAKI, M., AND TOKURA, Y. Trajectory of the anomalous

Hall effect towards the quantized state in a ferromagnetic topological insulator. *Nat. Phys. 10* (2014), 731–736.

[11] Kou, X., Guo, S.-T., Fan, Y., Pan, L., Lang, M., Jiang, Y., Shao, Q., Nie, T., Murata, K., Tang, J., Wang, Y., He, L., Lee, T.-K., Lee, W.-L., and Wang, K. L. Scale-invariant quantum anomalous Hall effect in magnetic topological insulators beyond the two-dimensional limit. *Phys. Rev. Lett. 113* (2014), 137201.

[12] Qi, X.-L., Hughes, T. L., and Zhang, S.-C. Chiral topological superconductor from the quantum Hall state. *Phys. Rev. B 82* (2010), 184516.

[13] Wang, J., Zhou, Q., Lian, B., and Zhang, S.-C. Chiral topological superconductor and half-integer conductance plateau from quantum anomalous Hall plateau transition. *Phys. Rev. B 92* (2015), 064520.

[14] Legendre, J., Zsurka, E., Di Miceli, D., Serra, L. m. c., Moors, K., and Schmidt, T. L. Topological properties of finite-size heterostructures of magnetic topological insulators and superconductors. *Phys. Rev. B 110* (2024), 075426.

[15] Adagideli, I., Hassler, F., Grabsch, A., Pacholski, M., and Beenakker, C. W. J. Time-resolved electrical detection of chiral edge vortex braiding. *SciPost Phys. 8*, 1 (2020).

[16] Beenakker, C. W. J., Baireuther, P., Herasymenko, Y., Adagideli, I., Wang, L., and Akhmerov, A. R. Deterministic creation and braiding of chiral edge vortices. *Phys. Rev. Lett. 122*, 14 (2019), 146803.

[17] Beenakker, C. J., Grabsch, A., and Herasymenko, Y. Electrical detection of the Majorana fusion rule for chiral edge vortices in a topological superconductor. *SciPost Phys. 6*, 2 (2019).

[18] Hassler, F., Grabsch, A., Pacholski, M. J., Oriekhov, D. O., Ovdat, O., Adagideli, I., and Beenakker, C. W. J. Half-integer charge injection by a Josephson junction without excess noise. *Phys. Rev. B 102* (2020), 045431.

[19] Clarke, D. J., Alicea, J., and Shtengel, K. Exotic circuit elements from zero-modes in hybrid superconductor–quantum-Hall systems. *Nat. Phys. 10*, 11 (2014), 877–882.

[20] Lee, G.-H., Huang, K.-F., Efetov, D. K., Wei, D. S., Hart, S., Taniguchi, T., Watanabe, K., Yacoby, A., and Kim, P. Inducing superconducting correlation in quantum Hall edge states. *Nat. Phys. 13* (2017), 693–698.

[21] Chen, C.-Z., Xie, Y.-M., Liu, J., Lee, P. A., and Law, K. T. Quasi-one-dimensional quantum anomalous Hall systems as new platforms for scalable topological quantum computation. *Phys. Rev. B 97* (2018), 104504.

[22] Nayak, C., Simon, S. H., Stern, A., Freedman, M., and Das Sarma, S. Non-Abelian anyons and topological quantum computation. *Rev. Mod. Phys. 80* (2008), 1083–1159.

[23] Chung, S. B., Qi, X.-L., Maciejko, J., and Zhang, S.-C. Conductance and noise signatures of Majorana backscattering. *Phys. Rev. B 83* (2011), 100512.

[24] Chen, C.-Z., He, J. J., Xu, D.-H., and Law, K. T. Effects of domain walls in quantum anomalous Hall insulator/superconductor heterostructures. *Phys. Rev. B 96* (2017), 041118.

[25] Lian, B., Wang, J., Sun, X.-Q., Vaezi, A., and Zhang, S.-C. Quantum phase transition of chiral Majorana fermions in the presence of disorder. *Phys. Rev. B 97* (2018), 125408.

[26] Beenakker, C. Angels and demons: Majorana and Dirac fermions in a quantum Hall edge channel. *Journal Club for Condensed Matter Physics* (2017).

[27] Ji, W., and Wen, X.-G. $\frac{1}{2}(e^2/h)$ Conductance plateau without 1D chiral Majorana fermions. *Phys. Rev. Lett. 120* (2018), 107002.

[28] Huang, Y., Setiawan, F., and Sau, J. D. Disorder-induced half-integer quantized conductance plateau in quantum anomalous Hall insulator-superconductor structures. *Phys. Rev. B 97* (2018), 100501.

[29] Kayyalha, M., Xiao, D., Zhang, R., Shin, J., Jiang, J., Wang, F., Zhao, Y.-F., Xiao, R., Zhang, L., Fijalkowski, K. M., Mandal, P., Winnerlein, M., Gould, C., Li, Q., Molenkamp, L. W., Chan, M. H. W., Samarth, N., and Chang, C.-Z. Absence of evidence for chiral Majorana modes in quantum anomalous Hall-superconductor devices. *Science 367*, 6473 (2020), 64–67.

[30] Ando, Y. Topological insulator materials. *J. Phys. Soc. Japan 82*, 10 (2013), 102001.

[31] König, M., Wiedmann, S., Brüne, C., Roth, A., Buhmann, H., Molenkamp, L. W., Qi, X.-L., and Zhang, S.-C. Quantum spin Hall insulator state in HgTe quantum wells. *Science 318*, 5851 (2007), 766–770.

[32] Bernevig, B. A., Hughes, T. L., and Zhang, S.-C. Quantum spin Hall effect and topological phase transition in HgTe quantum wells. *Science 314*, 5806 (2006), 1757–1761.

[33] Bendias, K., Shamim, S., Herrmann, O., Budewitz, A., Shekhar, P., Leubner, P., Kleinlein, J., Bocquillon, E., Buhmann, H., and Molenkamp, L. W. High Mobility HgTe Microstructures for Quantum Spin Hall Studies. *Nano Lett. 18*, 8 (2018), 4831–4836.

[34] Lunczer, L., Leubner, P., Endres, M., Müller, V. L., Brüne, C., Buhmann, H., and Molenkamp, L. W. Approaching quantization in macroscopic quantum spin Hall devices through gate training. *Phys. Rev. Lett. 123* (2019), 047701.

[35] Roth, A., Bruene, C., Buhmann, H., Molenkamp, L. W., Maciejko, J., Qi, X.-L., and Zhang, S.-C. Nonlocal transport in the quantum spin Hall state. *Science 325*, 5938 (2009), 294–297.

[36] Chen, Y. L., Analytis, J. G., Chu, J.-H., Liu, Z. K., Mo, S.-K., Qi, X. L., Zhang, H. J., Lu, D. H., Dai, X., Fang, Z., Zhang, S. C., Fisher, I. R., Hussain, Z., and Shen, Z.-X. Experimental realization of a three-dimensional topological insulator, Bi_2Te_3. *Science 325*, 5937 (2009), 178–181.

[37] Hasan, M. Z., and Kane, C. L. Colloquium: topological insulators. *Rev. Mod. Phys. 82* (2010), 3045–3067.

[38] Kong, D., Chen, Y., Cha, J. J., Zhang, Q., Analytis, J. G., Lai, K., Liu, Z., Hong, S. S., Koski, K. J., Mo, S.-K., Hussain, Z., Fisher, I. R., Shen, Z.-X., and Cui, Y. Ambipolar field effect in the ternary topological insulator $(Bi_xSb_{1\text{-}x})_2Te_3$ by composition tuning. *Nat. Nanotechnol. 6* (2011), 705–709.

[39] Zhang, H., Liu, C.-X., Qi, X.-L., Dai, X., Fang, Z., and Zhang, S.-C. Topological insulators in Bi_2Se_3, Bi_2Te_3 and Sb_2Te_3 with a single Dirac cone on the surface. *Nat. Phys. 5* (2009), 438–442.

[40] Zhang, J., Chang, C.-Z., Zhang, Z., Wen, J., Feng, X., Li, K., Liu, M., He, K., Wang, L., Chen, X., Xue, Q.-K., Ma, X., and Wang, Y. Band structure engineering in $(Bi_{1\text{-}x}Sb_x)_2Te_3$ ternary topological insulators. *Nat. Commun. 2* (2011), 574.

[41] Liu, C.-X., Zhang, H., Yan, B., Qi, X.-L., Frauenheim, T., Dai, X., Fang, Z., and Zhang, S.-C. Oscillatory from two-dimensional to three-dimensional topological insulators. *Phys. Rev. B 81* (2010), 041307.

[42] Chong, S. K., Liu, L., Watanabe, K., Taniguchi, T., Sparks, T. D., Liu, F., and Deshpande, V. V. Emergent helical edge states in a hybridized three-dimensional topological insulator. *Nat. Communun. 13* (2022).

[43] Huang, Y., and Shklovskii, B. I. Disorder effects in topological insulator thin films. *Phys. Rev. B 103* (2021), 165409.

[44] Nandi, D., Skinner, B., Lee, G. H., Huang, K.-F., Shain, K., Chang, C.-Z., Ou, Y., Lee, S.-P., Ward, J., Moodera, J. S., Kim, P., Halperin, B. I., and Yacoby, A. Signatures of long-range-correlated disorder in the magnetotransport of ultrathin topological insulators. *Phys. Rev. B 98* (2018), 214203.

[45] Mycielski, A., Rigaux, C., Menant, M., Dietl, T., and Otto, M. Spin glass phase transition in $Hg_{1\text{-}k}Mn_kTe$ semimagnetic semiconductors. *Solid State Commun. 50*, 3 (1984), 257–260.

[46] Shamim, S., Beugeling, W., Böttcher, J., Shekhar, P., Budewitz, A., Leubner, P., Lunczer, L., Hankiewicz, E. M., Buhmann, H., and Molenkamp, L. W. Emergent quantum Hall effects below 50 mT in a two-dimensional topological insulator. *Sci. Adv. 6*, 26 (2020), eaba4625.

[47] Cuono, G., Autieri, C., and Dietl, T. CdTe and HgTe doped with V, Cr, and Mn: Prospects for the quantum anomalous Hall effect. *Phys. Rev. B 110* (2024), 165112.

[48] Serlin, M., Tschirhart, C. L., Polshyn, H., Zhang, Y., Zhu, J., Watanabe, K., Taniguchi, T., Balents, L., and Young, A. F. Intrinsic quantized anomalous Hall effect in a moiré heterostructure. *Science 367*, 6480 (2020), 900–903.

[49] Deng, Y., Yu, Y., Shi, M. Z., Guo, Z., Xu, Z., Wang, J., Chen, X. H., and Zhang, Y. Quantum anomalous Hall effect in intrinsic magnetic topological insulator $MnBi_2Te_4$. *Science 367*, 6480 (2020), 895–900.

[50] Deng, H., Chen, Z., Wołoś, A., Konczykowski, M., Sobczak, K., Sitnicka, J., Fedorchenko, I. V., Borysiuk, J., Heider, T., Pluciński, L., Park, K., Georgescu, A. B., Cano, J., and Krusin-Elbaum, L. High-temperature quantum anomalous Hall regime in a $MnBi_2Te_4/Bi_2Te_3$ superlattice. *Nat. Phys. 17* (2021), 36–42.

[51] Li, T., Jiang, S., Shen, B., Zhang, Y., Li, L., Tao, Z., Devakul, T., Watanabe, K., Taniguchi, T., Fu, L., Shan, J., and Mak, K. F. Quantum anomalous Hall effect from intertwined moiré bands. *Nature 600* (2021), 641–646.

[52] Fox, E. J., Rosen, I. T., Yang, Y., Jones, G. R., Elmquist, R. E., Kou, X., Pan, L., Wang, K. L., and Goldhaber-Gordon, D. Part-per-million quantization and current-induced breakdown of the quantum anomalous Hall effect. *Phys. Rev. B 98* (2018), 075145.

[53] Lippertz, G., Bliesener, A., Uday, A., Pereira, L. M. C., Taskin, A. A., and Ando, Y. Current-induced breakdown of the quantum anomalous Hall effect. *Phys. Rev. B 106* (2022), 045419.

[54] Okazaki, Y., Oe, T., Kawamura, M., Yoshimi, R., Nakamura, S., Takada, S., Mogi, M., Takahashi, K. S., Tsukazaki, A., Kawasaki, M., Tokura, Y., and Kaneko, N.-H. Quantum anomalous Hall effect with a permanent magnet defines a quantum resistance standard. *Nat. Phys. 18* (2021), 25–29.

[55] Tokura, Y., Yasuda, K., and Tsukazaki, A. Magnetic topological insulators. *Nature Reviews Physics 1* (2019).

[56] Kawamura, M., Yoshimi, R., Tsukazaki, A., Takahashi, K. S., Kawasaki, M., and Tokura, Y. Current-driven instability of the quantum anomalous Hall effect in ferromagnetic topological insulators. *Phys. Rev. Lett. 119* (2017), 016803.

[57] Röper, T., Thomas, H., Rosenbach, D., Uday, A., Lippertz, G., Denis, A., Morfin, P., Taskin, A. A., Ando, Y., and Bocquillon, E. Propagation, dissipation, and breakdown in quantum anomalous Hall edge states probed by microwave edge plasmons. *Phys. Rev. B 110* (2024), L161403.

[58] Wang, J., Lian, B., and Zhang, S.-C. Universal scaling of the quantum anomalous Hall plateau transition. *Phys. Rev. B 89* (2014), 085106.

[59] Zhang, R.-X., Hsu, H.-C., and Liu, C.-X. Electrically tunable spin polarization of chiral edge modes in a quantum anomalous Hall insulator. *Phys. Rev. B 93* (2016), 235315.

[60] Zhang, Y., He, K., Chang, C.-Z., Song, C.-L., Wang, L.-L., Chen, X., Jia, J.-F., Fang, Z., Dai, X., Shan, W.-Y., Shen, S.-Q., Niu, Q., Qi, X.-L., Zhang, S.-C., Ma, X.-C., and Xue, Q.-K. Crossover of the three-dimensional topological insulator Bi_2Se_3 to the two-dimensional limit. *Nat. Phys. 6* (2010), 584–588.

[61] Chong, Y. X., Liu, X., Sharma, R., Kostin, A., Gu, G., Fujita, K., Davis, J. C. S., and Sprau, P. O. Severe Dirac mass gap suppression in Sb_2Te_3-based quantum anomalous Hall materials. *Nano Lett. 20*, 11 (2020), 8001–8007.

[62] Bonnet, D., Erlenkämper, S., Germer, H., and Rabenhorst, H. A new measurement of the energy gap in superconducting niobium. *Phys. Lett. A 25*, 6 (1967), 452–453.

[63] Legg, H. F., Loss, D., and Klinovaja, J. Metallization and proximity superconductivity in topological insulator nanowires. *Phys. Rev. B 105* (2022), 155413.

[64] Akhmerov, A. R., Nilsson, J., and Beenakker, C. W. J. Electrically detected interferometry of Majorana fermions in a topological insulator. *Phys. Rev. Lett. 102* (2009), 216404.

[65] Shen, J., Lyu, J., Gao, J. Z., Xie, Y.-M., Chen, C.-Z., Cho, C.-w., Atanov, O., Chen, Z., Liu, K., Hu, Y. J., Yip, K. Y., Goh, S. K., He, Q. L., Pan, L., Wang, K. L., Law, K. T., and Lortz, R. Spectroscopic fingerprint of chiral Majorana modes at the edge of a quantum anomalous Hall insulator/superconductor heterostructure. *Proc. Natl. Acad. Sci. U.S.A. 117*, 1 (2020), 238–242.

[66] Fu, L., and Kane, C. L. Probing Neutral Majorana Fermion Edge Modes with Charge Transport. *Phys. Rev. Lett. 102* (2009), 216403.

[67] Atanov, O., Tai, W. T., Xie, Y.-M., Ng, Y. H., Hammond, M. A., Manfred Ho, T. S., Koo, T. H., Li, H., Ho, S. L., Lyu, J., Chong, S., Zhang, P., Tai, L., Wang, J., Law, K. T., Wang, K. L., and Lortz, R. Proximity-induced quasi-one-dimensional superconducting quantum anomalous Hall state. *Cell Rep. Phys. Sci. 5*, 1 (2024), 101762.

[68] Mourik, V., Zuo, K., Frolov, S. M., Plissard, S. R., Bakkers, E. P. A. M., and Kouwenhoven, L. P. Signatures of Majorana fermions in hybrid superconductor-semiconductor nanowire devices. *Science 336*, 6084 (2012), 1003–1007.

[69] Pikulin, D. I., Dahlhaus, J. P., Wimmer, M., Schomerus, H., and Beenakker, C. W. J. A zero-voltage conductance peak from weak antilocalization in a Majorana nanowire. *New J. Phys. 14*, 12 (2012), 125011.

[70] Gül, O., Ronen, Y., Lee, S. Y., Shapourian, H., Zauberman, J., Lee, Y. H., Watanabe, K., Taniguchi, T., Vishwanath, A., Yacoby, A., and Kim, P. Andreev reflection in the fractional quantum Hall state. *Phys. Rev. X 12* (2022), 021057.

[71] Wan, Z., Kazakov, A., Manfra, M. J., Pfeiffer, L. N., West, K. W., and Rokhinson, L. P. Induced superconductivity in high-mobility two-dimensional electron gas in gallium arsenide heterostructures. *Nat. Comm. 6* (2015), 7426.

[72] Hatefipour, M., Cuozzo, J. J., Kanter, J., Strickland, W. M., Allemang, C. R., Lu, T.-M., Rossi, E., and Shabani, J. Induced superconducting pairing in integer quantum Hall edge states. *Nano Lett. 22*, 15 (2022), 6173–6178.

[73] Calado, V. E., Goswami, S., Nanda, G., Diez, M., Akhmerov, A. R., Watanabe, K., Taniguchi, T., Klapwijk, T. M., and Vandersypen, L. M. K. Ballistic Josephson junctions in edge-contacted graphene. *Nat. Nano. 10* (2015), 761–764.

[74] Zhao, L., Arnault, E. G., Bondarev, A., Seredinski, A., Larson, T. F. Q., Draelos, Anne W. Li, H., Watanabe, K., Taniguchi, T., Amet, F., Baranger, H. U., and Finkelstein, G. Interference of chiral Andreev edge states. *Nat. Phys. 13* (2020), 862–867.

[75] Blonder, G. E., Tinkham, M., and Klapwijk, T. M. Transition from metallic to tunneling regimes in superconducting microconstrictions: excess current, charge imbalance, and supercurrent conversion. *Phys. Rev. B 25* (1982), 4515–4532.

[76] Pannetier, B., and Courtois, H. Andreev reflection and proximity effect. *J. Low Temp. Phys. 118* (2004), 1573–7357.

[77] Eroms, J., Weiss, D., Boeck, J. D., Borghs, G., and Zülicke, U. Andreev reflection at high magnetic fields: evidence for electron and hole transport in edge states. *Phys. Rev. Lett. 95* (2005), 107001.

[78] Hoppe, H., Zülicke, U., and Schön, G. Andreev reflection in strong magnetic fields. *Phys. Rev. Lett. 84* (2000), 1804–1807.

[79] van Ostaay, J. A. M., Akhmerov, A. R., and Beenakker, C. W. J. Spin-triplet supercurrent carried by quantum Hall edge states through a Josephson junction. *Phys. Rev. B 83* (2011), 195441.

[80] Clarke, D. J., Alicea, J., and Shtengel, K. Exotic non-Abelian anyons from conventional fractional quantum Hall states. *Nat. Commun. 4*, 1 (2013), 1348.

[81] Huang, Y., Fu, Y., Zhang, P., Wang, L. K., and He, Q. L. Inducing superconductivity in quantum anomalous Hall regime. *J. Phys.: Condens. Matter. 36*, 37 (2024), 37LT01.

[82] He, Q. L., Pan, L., Stern, A. L., Burks, E. C., Che, X., Yin, G., Wang, J., Lian, B., Zhou, Q., Choi, E. S., Murata, K., Kou, X., Chen, Z., Nie, T., Shao, Q., Fan, Y., Zhang, S.-C., Liu, K., Xia, J., and Wang, K. L. RETRACTED: Chiral Majorana fermion modes in a quantum anomalous Hall insulator-superconductor structure. *Science 357*, 6348 (2017), 294–299.

[83] Thorp, H. H. Editorial retraction. *Science 378*, 6621 (2022), 718–718.

[84] Lachman, E. O., Young, A. F., Richardella, A., Cuppens, J., Naren, H. R., Anahory, Y., Meltzer, A. Y., Kandala, A., Kempinger, S., Myasoedov, Y., Huber, M. E., Samarth, N., and Zeldov, E. Visualization of superparamagnetic dynamics in magnetic topological insulators. *Sci. Adv. 1*, 10 (2015), e1500740.

[85] Lachman, E. O., Mogi, M., Sarkar, J., Uri, A., Bagani, K., Anahory, Y., Myasoedov, Y., Huber, M. E., Tsukazaki, A., Kawasaki, M., Yoshinori, T., and Zeldov, E. Observation of superparamagnetism in coexistence with quantum anomalous Hall $C = \pm 1$ and $C = 0$ Chern states. *npj Quantum Mater. 2* (2017), 70.

[86] Datta, S. *Electronic transport in mesoscopic systems.* Cambridge Studies in Semiconductor Physics and Microelectronic Engineering. Cambridge University Press, 1995.

[87] Lambert, C. J., and Raimondi, R. Phase-coherent transport in hybrid superconducting nanostructures. *J. Phys.: Condens. Matter. 10* (1998), 901–941.

[88] Kurilovich, V. D., Raines, Z. M., and Glazman, L. I. Disorder-enabled Andreev reflection of a quantum Hall edge. *Nat. Commun. 14* (2023), 2237.

[89] Galambos, T. H., Ronetti, F., Hetényi, B., Loss, D., and Klinovaja, J. Crossed Andreev reflection in spin-polarized chiral edge states due to the Meissner effect. *Phys. Rev. B 106* (2022), 075410.

[90] Michelsen, A. B., Recher, P., Braunecker, B., and Schmidt, T. L. Supercurrent-enabled Andreev reflection in a chiral quantum Hall edge state. *Phys. Rev. Res. 5* (2023), 013066.

List of Publications

1. Lippertz, G., Uday, A., Bliesener, A., Pereira, L. M. C., Taskin, A. A., and Ando, Y. Nonreciprocal charge transport on the edges of a quantum anomalous Hall insulator. *In preparation.*

2. Brede, J., Bagchi, M., Greichgauer, A., Taskin, A. A., Uday, A., Bliesener, A., Lippertz, G., Yazdanpanah, R., Rüssmann, P., Blügel, S., and Ando, Y. Superconducting proximity effect in $(Bi_{1\text{-}x}Sb_x)_2Te_3$ thin films probed by STM. *In preparation.*

3. Uday, A., Lippertz, G., Bhujel, B., Taskin, A. A., and Ando, Y.,Non-Majorana-origin of the half-integer conductance quantization elucidated by multi-terminal superconductor–quantum anomalous Hall insulator heterostructure. *Phys. Rev. B 111* (2025), 035440.

4. Uday, A., Lippertz, G., Moors, K., Legg, H. F., Joris, R., Bliesener, A., Pereira, L.M.C., Taskin, A. A., and Ando, Y.Induced superconducting correlations in a quantum anomalous Hall insulator. *Nat. Phys. 20* (2024), 1589–1595.

5. Brede, J., Bagchi, M., Greichgauer, A., Uday, A., Bliesener, A., Lippertz, G., Yazdanpanah, R., Taskin, A. A., and Ando, Y. Characterizing the chemical potential disorder in the topological insulator $(Bi_{1\text{-}x}Sb_x)_2Te_3$ thin films. *Phys. Rev. Mater. 8* (2024), 104202.

6. Röper, T., Thomas, H., Rosenbach, D., Uday, A., Lippertz, G., Denis, A., Morfin, P., Taskin, A. A., Ando, Y., and Bocquillon, E. Propagation, dissipation, and breakdown in quantum anomalous Hall edge states probed by microwave edge plasmons. *Phys. Rev. B 110* (2024), L161403.

7. Lippertz, G., Breunig, O., Fister, R., Uday, A., Bliesener, A., Brede, J., Taskin, A. A. and Ando, Y. Selective-Area Epitaxy of Bulk-Insulating $(Bi_xSb_{1\text{-}x})_2Te_3$ Films and Nanowires by Molecular Beam Epitaxy. *ACS Appl. Mater. Interfaces 16* (2024), 41293–41299.

8. Rössler, M., Fan, D., Münning, F., Legg, H. F., Bliesener, A., Lippertz, G., Uday, A., Yazdanpanah, R., Feng, J., Taskin, A., and Ando, Y. Top-down fabrication of bulk-insulating topological insulator nanowires for quantum devices. *Nano Lett. 23* 7 (2023), 2846–2853.

9. Lippertz, G., Bliesener, A., Uday, A., Pereira, L. M. C., Taskin, A. A., and Ando, Y. Current-induced breakdown of the quantum anomalous Hall effect. *Phys. Rev. B 106* (2022), 045419.

10. Legg, H. F., Rössler, M., Münning, F., Fan, D., Breunig, O., Bliesener, A., Lippertz, G., Uday, A., Taskin, A. A., Loss, D., Klinovaja, J., and Ando, Y. Giant magnetochiral anisotropy from quantum-confined surface states of topological insulator nanowires. *Nat. Nanotechnol. 17* (2022), 696–700.

11. Bai, M., Wei, X.-K., Feng, J., Luysberg, M., Bliesener, A., Lippertz, G., Uday, A., Taskin, A. A., Mayer, J., and Ando, Y. Proximity-induced superconductivity in $(Bi_{1\text{-}x}Sb_x)_2Te_3$ topological-insulator nanowires. *Commun. Mater. 3* (2022), 20.

12. Jolly, A., Uday, A., Gurumurthy, S. C., Shilpa, M. P., Surabhi, S. Mundinamani, S., Ramam, K., Gedda, M., Murari M. S., and Jeong, J. R. Effect of silane/amine-based dopants on polymer-metal interaction of sub-surface silver nanoparticulate films *J. Mater. Sci.: Mater. Electron. 32* (2021), 2719–2730.

13. Reinhoffer, C., Mukai, Y., Germanskiy, S., Bliesener, A., Lippertz, G., Uday, A., Taskin, A. A., Ando, Y., Wang, Z., and van Loosdrecht, P. H. M. Relaxation dynamics of the optically driven nonequilibrium states in the electron- and hole-doped topological-insulator materials $(Bi_{1\text{-}x}Sb_x)_2Te_3$. *Phys. Rev. Mater. 4* (2020), 124201.

FACULTY OF MATHEMATICS AND NATURAL SCIENCE
DEPARTMENT OF PHYSICS, INSTITUTE OF PHYSICS II
TOPOLOGICAL MATTER LABORATORY COLOGNE
Zülpicher Straße 77
50937 Cologne
Germany